To the Graduate Council:

I am submitting herewith a dissertation written by Wei Li entitled “An Investigation of the Deposition and Characterization of Materials Formed by Electron Beam Induced Deposition.” I have examined the final electronic copy of this dissertation for form and content and recommend that it be accepted in partial fulfillment of the requirements for the degree of Doctor of Philosophy, with a major in Materials Science and Engineering.

David C. Joy
Major Professor

We have read this dissertation
and recommend its acceptance:

Philip D. Rack

Joseph E. Spruiell

Anthony J. Pedraza

Accepted for the Council:

Linda Painter
Interim Dean of Graduate Studies

(Original signatures are on file with official student records.)

An Investigation of the Deposition and Characterization of Materials Formed by Electron Beam Induced Deposition

A Dissertation

Presented for the

Doctor of Philosophy

Degree

The University of Tennessee, Knoxville

Wei Li

December, 2006

Dedication

This dissertation is dedicated to my parents, Shu-Ping Li and An-Xiang Pan, for giving birth to me and ceaseless love and support throughout my life. I also want to dedicate this work to my brother, Fan Li, for inspiring me in many ways and for great love and support constantly. Another important person to whom I would like to dedicate my work is my mentor professor, Dr. David Joy, for teaching me to analyze and solve problems in the way of a scientist.

Acknowledgements

I would like to thank Dr. Young Choi, Yinghong Lin, Dr. Steven Randolph, Dr. Philip Rack, Sachin Deo and Jihoon Kim for lots of helpful discussions. I also want to give thanks to the other current and former members in our group along with all the members of Dr. Philip Rack's research group for their supports. Great appreciation is due Dr. Bernhard Frost at Oak Ridge National Laboratory, Dr. Maggie Connatser in Chemistry Department, Dr. Nicholas Ritchie at National Institute of Standards and Technology, Tim Grundman in Electrical Engineering Department and Toshihide Agemura and Takeshi Ogashiwa at Hitachi High Technologies. Without their advices and efforts, this work cannot be done. Finally, I would like to thank my committee members: Dr. David Joy, Dr. Anthony Pedraza, Dr. Philip Rack and Dr. Joseph Spruiell. Their guidance and expertise was indispensable.

Abstract

This dissertation deals with EBID – Electron Beam Induced Deposition – a novel bottom up nanofabrication technique. Since EBID was first employed for nano-patterning, a number of empirical factors were investigated to control deposition process. Meanwhile a few theoretical models were proposed based on some fundamental assumptions. So far little work has been done to verify the validity of these assumptions. The main objective of my PhD study, therefore, was to answer whether these assumptions are valid so that unifying the empirical factors and theoretical models would be possible. Electrical resistivity of deposited materials was another interesting topic included in this work.

Verification of the assumptions was the core of this work. It started with the first assumption that the reaction happens on the surface. The substrate temperature was changed under controlled beam conditions to study how the growth rate was affected and the result provided evidence for the first assumption. The same data confirmed the second assumption that the mean lifetime of adsorbed molecules follows an Arrhenius relation. To verify the third assumption that secondary electrons drive the dissociation reaction, a variety of experiments were designed. It was attempted to suppress secondary emission by biasing the substrate or change secondary emission yield by controlling the experimental conditions. No correlation with deposition rate was found. But the experiments led to a better understanding of the role of interaction volume in deposition. Time-resolved sample current monitoring was then adopted to study electron scattering during deposition and a characteristic trend was found in the measurements. NISTMonte, was employed to simulate electron scattering for comparison. The estimation from the simulation agreed with the experiment. The role of backscattered electrons was also investigated by depositing lines across the boundary between a bulk material and thin film. The substrate thickness was found no influence on the linewidth of the deposits, which was explained by the transition of interaction volume. At last, a theoretical estimation suggested that backscattered electrons predominate the deposition for keV range primary electrons.

The second part of this work is to measure resistivity of the deposited materials. Four-point measurement circuits were fabricated on a wafer through thin film process. A probe station was used to measure the resistance and SEM and AFM were adopted to provide dimensional information. The resistivity of the deposited materials showed that the deposited materials have resistivity in semiconducting material range and the deposited material formed at slow scan speed had a lower resistivity than that formed at fast scan speed.

Table of Contents

List of Figures

List of Abbreviations

AES	Auger Electron Spectrometer
AFM	Atomic Force Microscope
AlF_3	Aluminum Fluoride
BEB	Binary-Encounter-Bethe
BSE	Backscattered Electron
CD	Critical Dimension
CVD	Chemical Vapor Deposition
CNT	Carbon Nanotube
DUV	Deep Ultraviolet
EBID	Electron Beam Induced Deposition
EBL	Electron Beam Lithography
EDS	Energy Dispersive X-Ray Spectrometry
ESD	Electron Stimulated Desorption
ESED	Environmental Secondary Electron Detector
E-T	Everhart-Thornley
FE	Field Emission
FWHM	Full Width at Half Maximum
IBID	Ion Beam Induced Deposition
IP	Ion Pump
IPA	Isopropanol
MIBK	Methyl Isobutyl Ketone
NA	Numerical Aperture
NIH	National Institutes of Health
NIST	National Institute of Standards and Technology
PC	Photonic Crystal
PE	Primary Electron
PMMA	PolyMethyl MethAcrylate
PVD	Physical Vapor Deposition
RGA	Residual Gas Analyzer

RP	Rough Pump
QCM	Quartz Crystal Microbalance
SE	Secondary Electron
SEM	Scanning Electron Microscope
SET	Single Electron Transport
SiF_4	Silicon Tetrafluoride
Si_3N_4	Silicon Nitride
STEM	Scanning Transmission Electron Microscope
STM	Scanning Tunneling Microscope
TEM	Transmission Electron Microscope
TMP	Turbomolecular Pump
TOF-MS	Time-Of-Flight Mass Spectrometer
TPD	Temperature Programmed Desorption
UHV	Ultra-high Vacuum
HV	High Vacuum
VPSEM	Variable Pressure Scanning Electron Microscope
$W(CO)_6$	Tungsten Hexacarbonyl
WF_6	Tungsten Hexafluoride
YAG	Yttrium Aluminum Garnet
ZrO_2	Zirconium Dioxide

Chapter 1 Introduction

1.1 Definition

Electron beam induced deposition (EBID), also called "direct writing", is an inexpensive, maskless technique which can fabricate structures of various sizes, shapes and materials on the submicron and nanometer scale. EBID is essentially a chemical vapor deposition (CVD) process. It employs an electron beam to dissociate the precursor molecules sticking to a substrate when a precursor gas is introduced into a vacuum chamber, leaving a non-volatile deposit on the substrate and a volatile by-product pumped out of the chamber. A schematic set-up is illustrated in Figure 1.1.

1.2 History and development

The discovery that electrons can deposit materials on the sample is not new. Ever since the first electron microscope was invented, the observation that materials grow on the area where electron beam scans has been reported. The earliest traceable documentation was from Stewart[2] in 1934. She pointed out: "In an evacuated tube in which the slightest traces of organic vapors may occur, . . . insulating layers are formed on surfaces subject to electron . . . bombardment. These layers may be attributed to carbon compounds, and their formation is related to the polymerization of organic vapors . . . ." Afterwards intensive researches were performed to study the carbon films formed on sample surfaces that were irradiated by electron beam in the presence of organic molecules[3-7]. In those days this insulating film was undesirable and viewed as an obstacle to advances in true micro-chemical and high-resolution micro-structural analyses. Therefore it was given the name *contamination* by analytical electron microscopists and most of the studies then focused on how to reduce the contamination.

Not until about twenty years later did people realize this contamination could be applied as a new technique of lithography in many fields. The first attempts were carried out in 1956 to measure astigmatism in a probe forming system[8, 9] and then in 1969 to

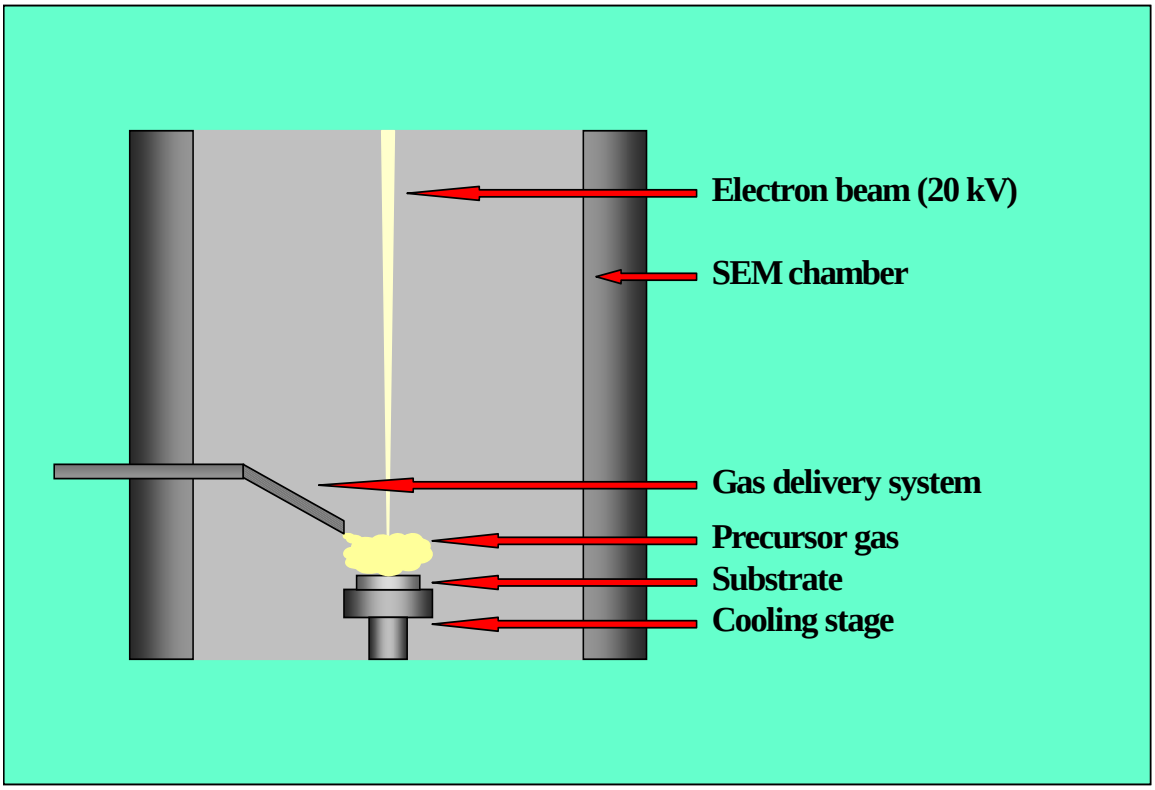

Figure 1.1 EBID System Schematic

A schematic diagram of EBID system representing a standard SEM chamber equipped with a gas delivery system for EBID.

determine the highest possible information density obtainable by lithographic methods[10, 11]. Broers et al. were the first to use contamination grown patterns as an etching mask to define 8-nm-wide metal lines[12]. Though its merit was revealed this electron beam direct writing technique was not paid enough attention until three driving forces appeared in the late 70's.

First the semiconductor industry advanced into sub-micron era, as predicted by Moore's Law. Moore's Law says that the number of transistors per chip would roughly double every 18 months, which means in approximately every 18 months the linear minimum feature size will shrink by half[13]. The feature size W of photolithography is determined by

$$W_{\min} \approx k \frac{\lambda}{NA} \qquad 1.1$$

where k is a constant of order 0.75, λ is the wavelength and NA is the numerical aperture of the system[14]. The numerical aperture NA is limited because of mechanical reasons. Thus the only way to decrease the feature size is adopting shorter wavelengths. However, even shorter wavelengths, like deep ultraviolet (DUV) light, can only push the feature size down to 65nm. Photolithography is reaching its limit and new technologies are called upon to produce even finer feature size to follow Moore's Law. Electron beam direct writing technique is found to be a promising substitute to photolithography because of the very fine size of the beam.

In the meantime a revolution that will deeply influence the twenty-first century was conceived in the academic society. In a talk entitled *There's Plenty of Room at the Bottom*, given by Richard Feynman in 1959, he suggested that it should be possible to manipulate atoms and molecules directly and in principle it should be possible to carry out chemical synthesis by mechanical manipulation and build a tiny, swallowable surgical nanobot (nano-robot). Norio Taniguchi in 1974 coined the term *Nanotechnology* to describe the precision manufacture of materials at nanometer tolerance. This term was

later popularized by K. Eric Drexler in his 1986 book *Engines of Creation: The Coming Era of Nanotechnology*. Two types of approaches have been developed to achieve the goal. One is termed as 'bottom up' approach, in which structures are built by combining numbers of smaller components, and the other 'top down' approach in which small features are constructed out of larger ones. Self-assembly is one type of 'bottom up' approach. Electron Beam Induced Deposition (EBID), Ion Beam Induced Deposition (IBID) and Electron Beam Lithography (EBL) are the most common 'top down' approaches. EBID is winning more and more attention because of its cleanness and better resolution compared with IBID and simpleness compared with EBL.

The new development of characterization techniques with atomic scale resolution is another important driving force. Transmission electron microscopes (TEM) and scanning transmission electron microscopes (STEM) have been improved to reach even sub-angstrom resolution. Atomic force microscope (AFM) and scanning tunneling microscope (STM) give researchers the capability to look at surfaces and to move atoms around.

Because of all the driving forces mentioned above, since 1980s the research on EBID has increased significantly. All empirical factors, such as beam current[4, 15-52], beam energy[16, 20, 26, 29, 38, 39, 42, 51, 53-57], base pressure[23, 24, 29, 30, 38, 41, 43, 58-65], precursor material, substrate material, substrate temperature[22, 26, 32, 50, 60, 66, 67] and scan rate[23, 46, 47, 57, 68], have been investigated to find out how these factors influence growth rate of deposition. Scanning electron microscope (SEM), transmission electron microscope (TEM), scanning transmission electron microscope (STEM), Auger electron spectroscope (AES), scanning tunneling microscope (STM) and dual-beam (ion beam and electron beam) system have been exploited to carry out in-situ morphology, structure and characterization studies. Beam deflecting controller and electron beam lithography system (EBL) have also been applied to make pattern transferring and 3-D fabrication. A number of models have been proposed to explain how the empirical factors impact growth rate, structure and properties and to simulate the deposition process. In recent years the focus of the research has changed to application of

EBID. EBID has been adopted in application like mask repair[69], nanostructure circuit[55, 70], microelectronic GHz switch[71], photonic crystal[72], miniature tunnel junction[43], attachment of carbon nano-tube[73-76], wiring biomolecules[77-79], tip fabrication for AFM[17, 21, 80-83], quantum devices[50, 84-87], field emission tips[45, 46, 88-98], solid-state Fresnel lenses[99] and mask fabrication for ion milling[100]. A number of commercial EBID systems have been launched to the market. These EBID systems are equipped with pattern generation software, high-speed beam blank as well as high-precision gas delivery unit. Some representative models of these systems include MeRiT MG mask repair system from NaWoTec, DualBeam system and Nova NanoSEM system from FEI, CrossBeam system from Carl Zeiss and FIB-SEM Hybrid System and Triple Beam System from SII Nanotechnology.

1.3 Applications

1.3.1 Mask repair

Liang and Stivers[69] employed a focused electron beam instead of a focused ion beam to deposit materials for clear defect repair on a phase-shift mask. Their results demonstrated that the repair was damage-free and that electron beams can offer superior spatial resolution for high edge placement precision and image quality for small defects on ever shrinking mask features.

1.3.2 Nanostructure circuit fabrication

Gopal et al. presented a prototype for rapid circuit fabrication at the nanometer scale, which starts with the fabrication of Ohmic contacts by electron beam induced deposition and then formation of interconnects by ion beam induced deposition. This method was applied to three-terminal transport measurement of Y-junction carbon nanotubes and fabrication of nanocircuit for determination of electromechanical degradation of silver nanowires[70].

1.3.3 Vacuum microelectronic GHz switch fabrication

Three-dimensional components such as ultra fast vacuum microelectronic switches and focusing lenses were made via EBID under computer control with nanometer precision. These components make miniaturized electron optical probe forming systems and imaging systems feasible.[71]

1.3.4 Photonic crystal fabrication

Because of its high resolution and accuracy additive nanolithography with EBID was employed to fabricate photonic crystals (PC) and PC devices to investigate their activity and characteristics. The initial promising results show optical filter action, which indicates these photonic crystals can act as filters in the infrared region[72].

1.3.5 Miniature tunnel junction

Komuro et al. applied EBID using WF_6 gas to make very thin metallic wires and metal/insulator/metal tunnel junctions for single-electron transport (SET) devices. Electrical properties of the tunnel junctions connected to the wires showed non-linear behavior that indicated a Fowler-Nordheim plot[43].

1.3.6 Bonding carbon nanotubes

EBID of low melting point metals was employed to bond carbon nanotubes (CNT) to electrodes for new microelectronic devices using CNTs. The results showed a bonding between CNTs and electrodes with improved electric conductivity and mechanical strength[73]. By the same method CNT-base transistors and CNT-attached AFM tips were fabricated by Kim et al. and a multi-walled CNT bridge was placed and soldered to a gold electrode structure to construct a nanoscale mass sensor by Mateiu et al.[75]. Kim and Lieber[76] reported that by using EBID to attach carbon nanotubes to the independent electrodes fabricated on pulled glass micropipettes and applying voltages to open and close the open ends of the nanotubes nanotube nanotweezers were realized.

1.3.7 Wiring biomolecules

EBID has been reported to make electric contact to single biomolecules to investigate electron transport phenomenon through the biomolecules. The initial measurements confirmed the feasibility of the EBID approach for connecting a nanoscale molecule to a measurement device[77-79].

1.3.8 Tip fabrication for AFM

EBID was used to fabricate high aspect ratio tips suitable for imaging in AFM. The growth rate and shape (length, cone angle and cone length) of the tips were systematically investigated. Both lateral and vertical resolutions of AFM were significantly improved[17, 21, 80, 81].

1.3.9 Quantum devices

Crozier et al. presented a nanolithography technique to fabrication periodic arrays of uniformly sized quantum dots. The technique is based on EBID and single-source molecular hydride chemistry. Uniform dots of height 5nm and full width at half maximum (FWHM) 4nm were achieved in this way[84]. Similar work was carried out by Guise et al.[87].

1.3.10 Field emission tips

Very high brightness field emission tips were fabricated via EBID. Brightness values exceeding that of conventional field emitters by a factor of 10 were demonstrated. Massive parallel electron beams can be generated in a computer-controlled fashion and can be applied to high through-put lithography[92]. Experiments to improve field emitters by EBID have also been carried out[45, 46, 88-91, 93-98].

1.3.11 Solid-state Fresnel lenses for electron optics

EBID was reported to fabricate the solid-state Fresnel lenses for electron optics by overwriting an AlF_3 film with the lens pattern. These lenses, which can be convergent or divergent, are not expected to compete with conventional magnetic lenses in most applications (such as microscopy), but may find a niche in electron-beam lithography[99].

1.3.12 Mask fabrication for ion milling

A process combining EBID and low energy ion milling makes it possible to fabricate nanometer-sized structures with various materials with high crystallinity, which is a critical factor for device fabrication. In addition, because of the minimum damage caused by this process during thinning a desired region in a sample it is useful for sample preparation for TEM[100].

Chapter 2 EBID system setup

2.1 Introduction

The work to be presented in this dissertation was carried out on an EBID system, as shown in Figure 2.1, modified from a Hitachi S-4300SE/N variable pressure scanning electron microscope (VPSEM) equipped with a Schottky emission electron gun. The sectional view of the Hitachi S-4300SE/N VPSEM is illustrated in Figure 2.2. The secondary electron (SE) detector, backscattered electron (BSE) detector, environmental secondary electron detector (ESED), energy dispersive X-ray spectrometry (EDS) detector and real-time high resolution electric current measurement on the Hitachi 4300SE/N SEM allow in-situ morphological analysis in both high and low vacuum and in-situ chemical composition analysis. The EBID system includes a vacuum system, an electron optics system, a temperature-control system, a gas delivery system and an imaging and analysis system. Each part will be introduced individually in the following sections.

2.2 The vacuum system

The vacuum system consists of three rough pumps (RP), two turbomolecular pumps (TMP) and three ion pumps (IP). The Schottky emitter gun tip is protected at ultrahigh vacuum (UHV) range $\sim 1\times10^{-7}$ Pa as being separated from the specimen chamber by a number of intermediate chambers. As illustrated in Figure 2.2, these intermediate chambers are pumped down by IP1, IP2 and IP3, all of which are backed with TMP2. The lowest intermediate chamber is directly supported by TMP2 and is connected to the specimen chamber through a differential aperture that allows electrons to pass through while keeping the gun tip from contamination. The specimen chamber is backed with TMP1 at a high vacuum (VH) range $\sim 1\times10^{-4}$ Pa in normal working mode. Both TMP1 and TMP2 are backed with the three rough pumps.

A computer-controlled leak valve allows the chamber pressure to vary from high

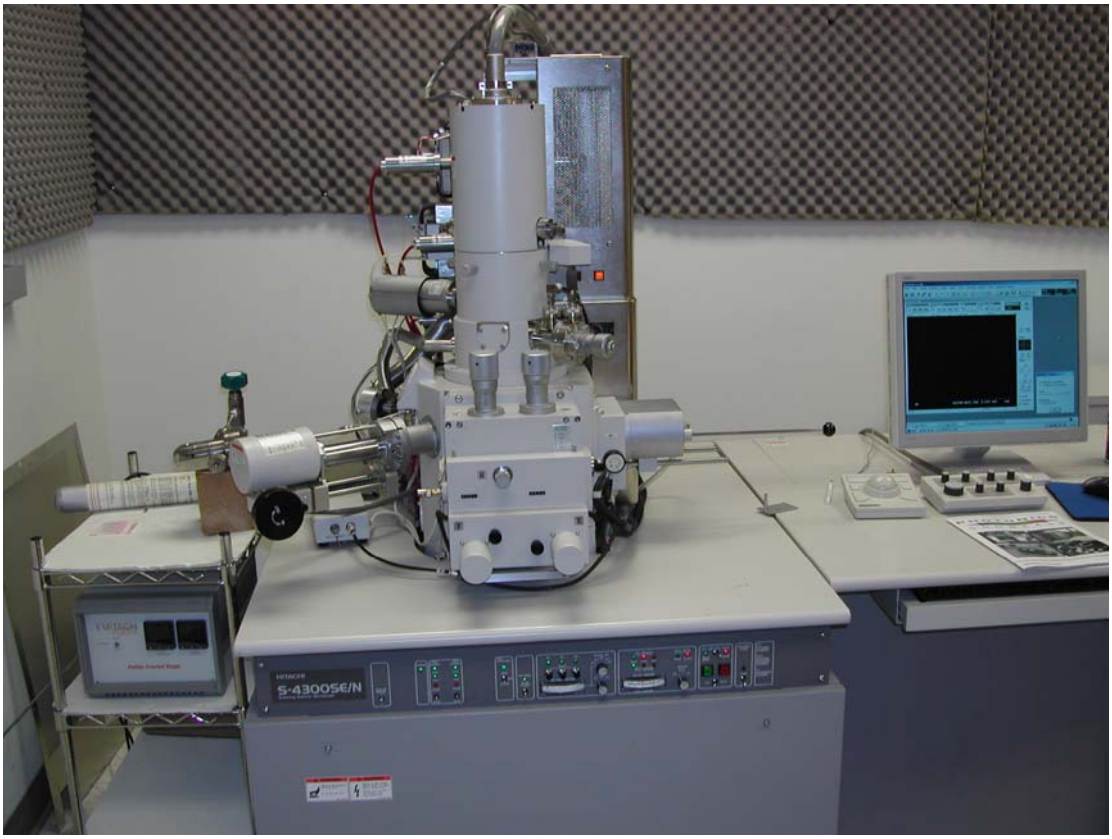

Figure 2.1 Experimental EBID System

A digital photograph of the experimental EBID system modified from a Hitachi S-4300SE/N variable pressure scanning electron microscope (VPSEM) equipped with a Schottky field emission electron gun.

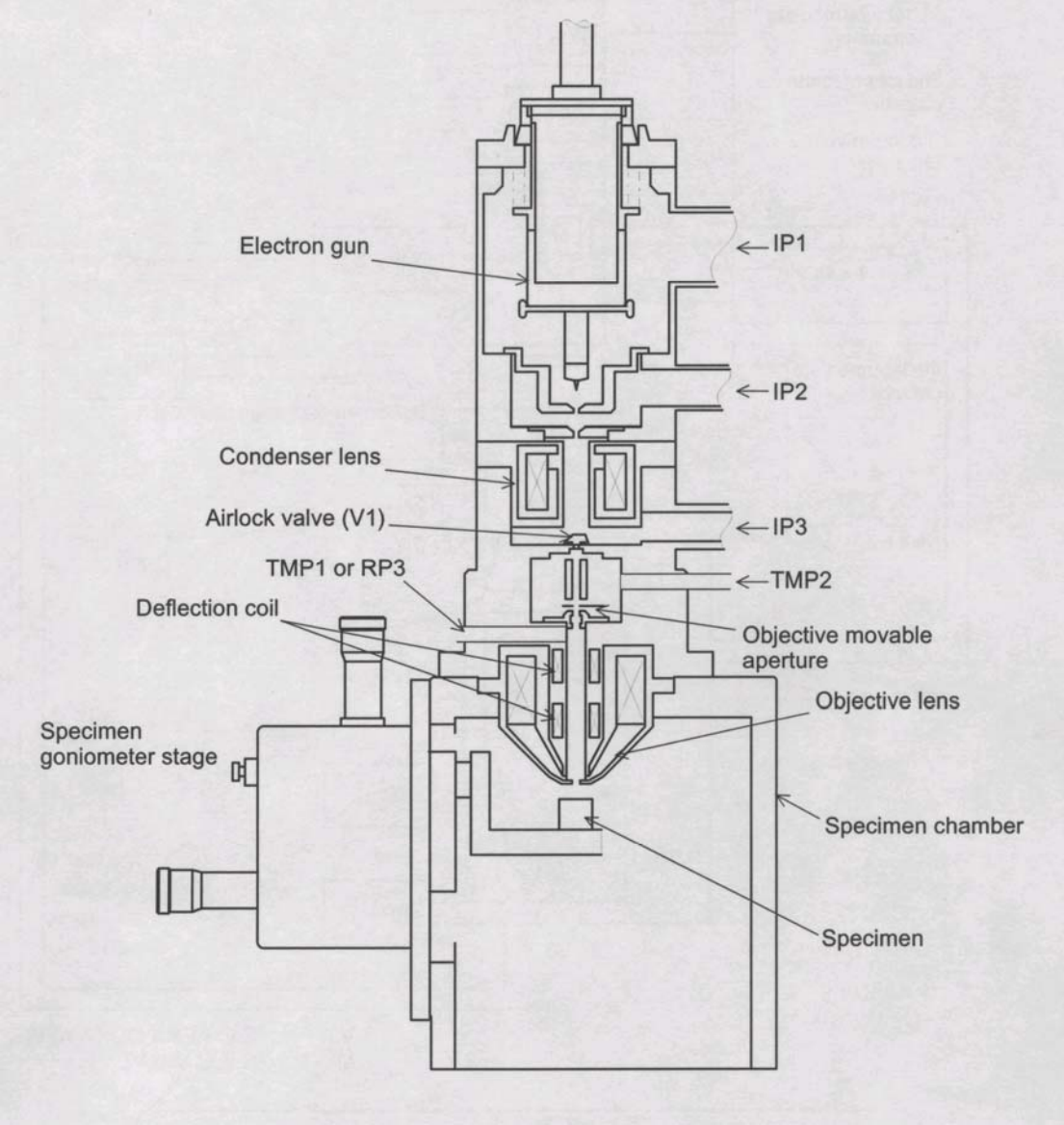

Figure 2.2 Schematic of Column Unit

A cross-sectional schematic of column unit on the Hitachi S-4300SE/N VPSEM illustrating the lens and vacuum configuration.

vacuum (1×10^{-4}~1×10^{-2} Pa) to low vacuum (10~1000 Pa) while the pressure of the electron column is always maintained at below 1×10^{-7} Pa. The pressures in the electron column and the specimen chamber are monitored by Penning gauges which detect low pressure range 10^{-8}~10^{-1} Pa and Pirani gauges which measure high pressure range 10^{-1} ~1000 Pa.

2.3 The electron optics system

The Hitachi S4300SE/N VPSEM is equipped with a Schottky emission electron gun because it provides a remarkably stable emission current. The Schottky emission electron gun consists of a cathode, suppressor electrode, first anode and second anode. The cathode (tip) is a ZrO_2/W Schottky emission tip with a sharp needle point from which electrons are extracted. Achieving the desired stability of the emission current requires an ultrahigh vacuum (below 1×10^{-7} Pa) and maintaining tip at a constant temperature of about 1700 K. The suppressor electrode suppresses the unwanted thermal electrons from the filament which supports the tip. An extracting voltage is applied between the cathode and first anode to control the emission current from the tip. An accelerating voltage in a range of 0.5 to 30 kV is provided between the cathode and the second anode.

The electron optics in the microscope, as shown in Figure 2.2, can be described as follows. The electron gun produces a stream of monochromatic electrons. The stream is condensed by a first condenser lens and condenser aperture which form the beam and eliminate the high-angle electrons from the beam. Then the beam is further confined by a second condenser lens and an objective movable aperture into a thin, tight and coherent beam. A set of deflection coils scans the beam in a raster fashion and the objective lens focuses the scanning beam onto the sample surface.

The electron beam scans across the surface in a raster fashion which moves the beam from side to side in lines from top to bottom. The beam dwells at each point for a period of time determined by the scan speed (usually in the microsecond range) and

interaction occurs inside the sample and the resulting signals are counted by the detectors and displayed on the CRT. This process is repeated until this frame is finished and then the next frame repeats. The SEM provides three scan modes: spot, line and box mode, which enable simple pattern transfers in EBID. More complex pattern transfers can be accomplished by installing a vector-scan controller to the system. The SEM also allows electron beam to scan at various speeds.

2.4 The temperature-controlling system

An Emitech K25X Peltier cooling stage, as shown in Figure 2.3, is installed on the original sample stage of the SEM. The cooling stage is connected to an external control unit and a water chiller via a feed-through port on the specimen chamber wall. The temperature of the cooling stage, which can vary from –30 to 75 °C, can be set and monitored through an electrical lead-through by the control unit. Two tubes connecting the cooling stage and the chiller form a liquid cooling circuit, taking away the heat generated at the hot end of the Peltier cooling stage.

2.5 The gas delivery system

The gas delivery system, shown in Figure 2.4, includes a reservoir storing the precursor gas, a leak valve unit controlling the gas flow and a wobble stick with a hypodermic needle at the end providing the capability to localize the gas to the surface from a desired distance and angle.

2.5.1 The precursor gases

Tungsten hexafluoride (WF_6) was chosen as the precursor gas in this work because one of the most important applications of EBID is photomask repair and tungsten is one ideal candidate for this purpose. WF_6 is a corrosive chemical commonly used in chemical vapor deposition (CVD). It is odorless and colorless and has a melting point of 2.3 °C and a boiling point of 17.0 °C. The molecule of WF_6 has an octahedral structure and a dipole moment of zero.

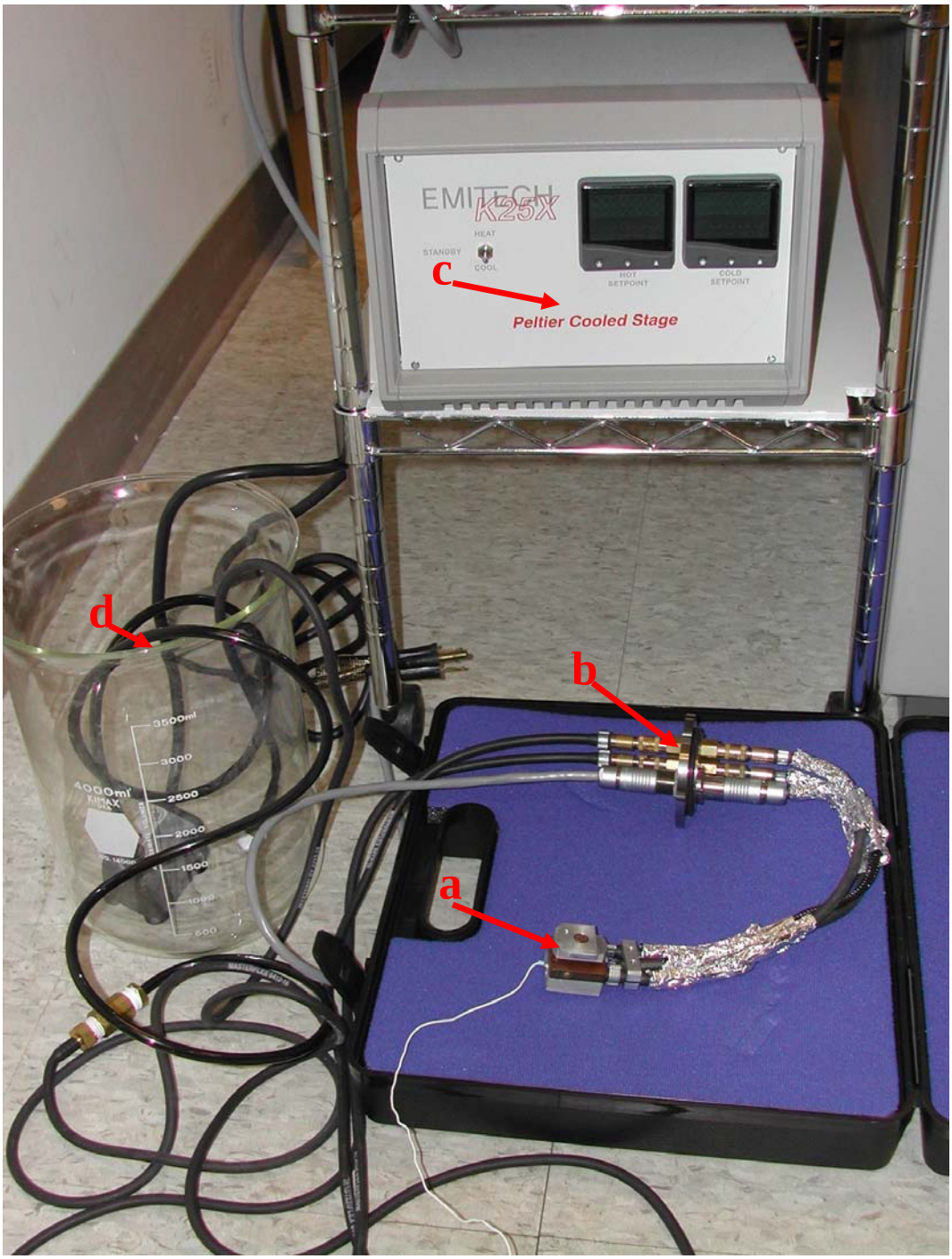

Figure 2.3 Peltier Cooling Stage

A digital photograph of the Emitech K25X Peltier cooling stage installed on the EBID system, which includes (a) a cooling stage, (b) a vacuum feed-through port, (c) an external control unit and (d) a water chiller.

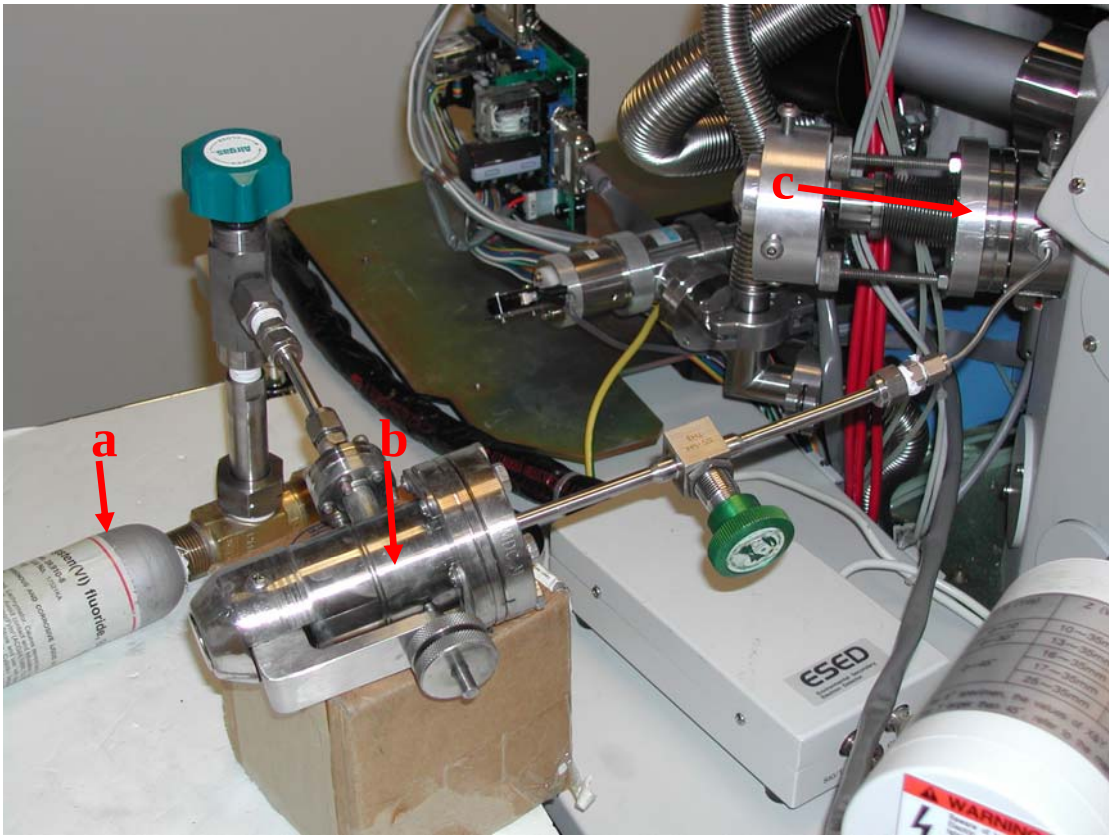

Figure 2.4 Gas Delivery System

A digital photograph of the gas delivery system consists of (a) a reservoir, (b) a leak valve and (c) a wobble stick with a hypodermic needle on the end.

Tungsten hexacarbonyl ($W(CO)_6$) was initially adopted as the precursor but was later given up because it induces a lot of carbon contamination in the deposit and also because it needs heating during the experiment and has a tendency to condense and cause clogging problem to the tubes and valves during and after the experiment.

2.5.2 The gas flow control unit

It is of great significance to have a fine control of the gas flow because this allows an investigation of EBID as a function of chamber pressure. In addition, the SEM can only allow a tiny amount of gas flow into the specimen chamber when operated in high vacuum mode. The gas flow control unit consists of a set of shut-off valves and a Varian variable leak valve, which provides a very fine control and a rapid adjustment of the gas flow.

2.5.3 The wobble stick

The wobble stick, shown in Figure 2.5, is mounted on the wall of the specimen chamber through a vacuum flange, providing the capability to localize the gas flow to the desired area on substrate surface. It is a metal rod extending into the chamber and supporting a hypodermic needle of a 0.5 mm inner diameter which is mounted on the end of the rod. The other end of the rod passes through a ball, extending outside of the chamber and restrained by a spring unit mounted on the vacuum flange. The ball is coupled in a metal ring by four adjusting screws. Loosening or tightening the screws enables the metal rod to move in the plane perpendicular to the rod axis. The ring is supported and held by three long bolts to counter the dragging force from the spring unit. These bolts can be adjusted to allow the metal rod to move in the longitudinal direction. Thus the wobble stick provides the capability to maneuver the needle from outside of the chamber and to position the needle close to the substrate and beam axis.

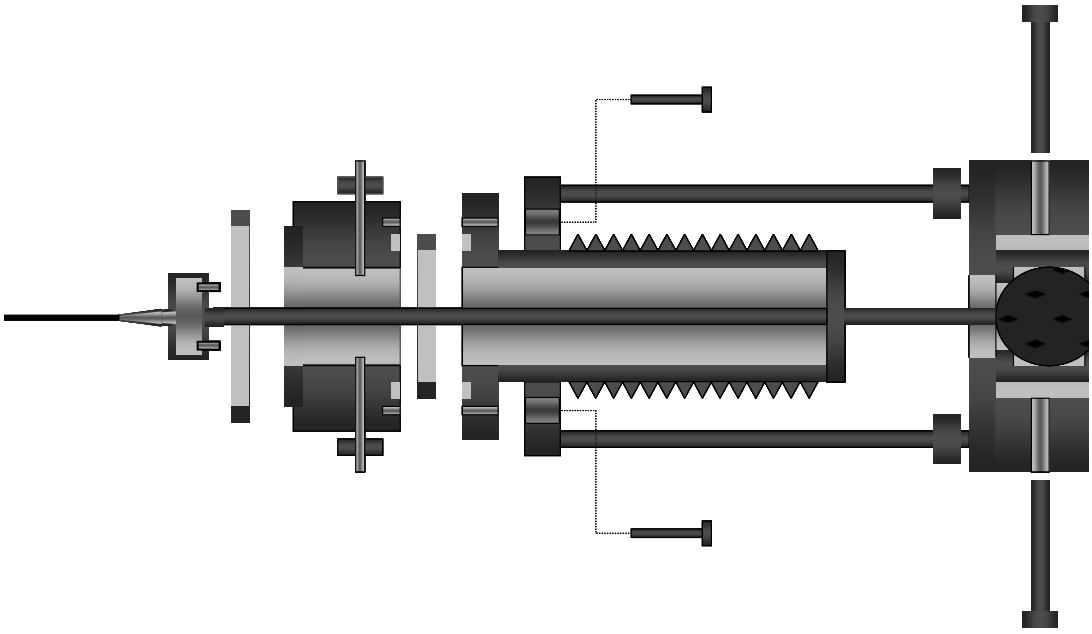

(a)

(b)

Figure 2.5 Wobble Stick

A figure showing (a) a schematic and (b) a digital photograph of the wobble stick used in the EBID system.

2.6 The imaging and analysis system

The imaging and analysis system consists of SE, BSE, ESED and EDS detectors, which enables in-situ analysis of morphology, chemical composition.

2.6.1 The SE detector

The SE detector is an Everhart-Thornley (E-T) detector, as shown in Figure 2.6, consisting of a scintillator, light guide and photomultiplier. An energetic electron (keV energy) interacting with the scinitillator can produce photons. These photons are conducted to the photomultiplier by total internal reflection by the light guide. Electrons are generated by the bombardment of photons on the photomultiplier and then amplified by cascade effect. Thus SE signals are collected to form a SE image on the monitor. To collect SE signals, a large positive bias is applied to the scintillator so that low-energy secondary electrons can gain enough energy to produce photons. A Faraday cage is placed around the scintillator to shield the field so the electron beam will not be deflected. A SE image can provide information such as compositional contrast and topographic contrast. The drawback of E-T SE detector is that it cannot be used in low vacuum environment because the high voltage applied to the scintillator would result in a destructive flashover.

2.6.2 The BSE detectors

The Hitachi S4300SE/N has two BSE detectors. The first one shares the same E-T detector with the SE detector. To get rid of the SE signals, a negative bias of –50 V is applied to the Faraday cage to completely repel the secondary electrons. The efficiency of this type of BSE detector is not satisfying because only backscattered electrons flying toward the BSE detector can be collected. To improve the efficiency a second BSE detector, using a YAG (Yttrium Aluminum Garnet) single crystal disc scintillator, is mounted right beneath the polepiece of the objective lens. The BSE signal efficiency is significantly boosted due to the increase of the solid angle of collection. A BSE image can provide information of composition and topography as well. In addition, the high

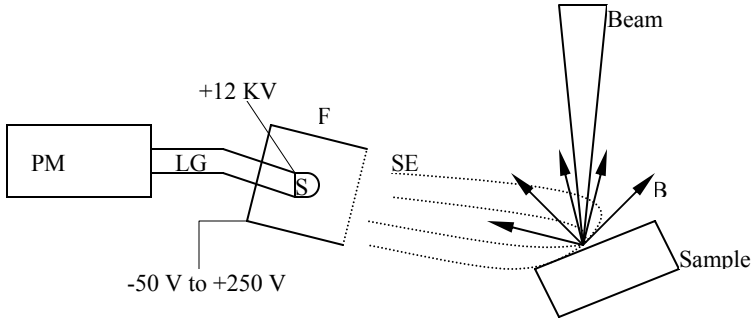

Figure 2.6 Everhard-Thornley Detector

A schematic diagram of the Everhart-Thornley detector: B, backscattered electron trajectories; SE, secondary electron trajectories; F, Faraday cage (bias range from –50 V to +250 V); S, Scintillator, with thin metallic coating: high bias (+12 kV) supply to the scintillator coating; LG, light guide; PM, photomultiplier.

kinetic energy of backscattered electrons enables the BSE detector to work in both high vacuum and low vacuum.

2.6.3 The ESED detector

Although the BSE detector is generally useful there are many occasions when a true SE image is required. The environmental secondary electron detector (ESED), which converts the secondary electrons into ions and then counts the ion signal, provides this capability. A positively biased electrode is set between the grounded specimen and the objective lens. The anions generated by secondary electron interaction with the gas drift towards the electrode, producing a secondary ion cascade as they accelerate in the field. The ion flow in the gas induces a current in the external circuit which is used for imaging. Since ions drift much more slowly than electrons, the response time of ESED detectors is slower than conventional SE detector. But it gives an option for situations where a true SE image is requested.

2.6.4 The EDS detector

The EDS detector is made of p-1-n silicon diode, biased with a high voltage. X-ray photons generated by electron bombardment on the specimen strike the detector, creating electron-hole pairs that drift in opposite directions due to the high voltage. The electron-hole pairs are then transformed to a charge pulse which is then converted to a voltage pulse. The voltage pulse is further amplified and analyzed by a computer x-ray analyzer. Since the voltage pulse is a function of the energy of x-ray photon, an energy spectrum can thus be made for chemical composition analysis. The advantage of the EDS detector is that it allows analysis of local area and provides functions such as x-ray mapping.

2.6.5 The time-resolved sample current measurement unit

The electric current measurement is connected to the sample stage through the grounding port of the SEM. During the deposition process, the sample current, which is

the beam current subtracted by the emitted backscattered electrons and secondary electrons, is conducted through the grounding path and collected by the measurement. To measure the beam current, a Faraday cup, which is a graphite cylinder with a very small hole drilled on the top, is placed on the sample stage to collect all the incoming electrons. There are two options for the measurement unit. The first option is Keithley 485 Autoranging Digital Picoammeter with resolution of up to 100 fA. For the purpose of monitoring the real-time sample current, a Keithley 6485 Digital Picoammeter with resolution of up to 10 fA and reading rate of up to 1000 per second can be employed together with a PC-based data acquisition/control system. The ExceLINX software installed on the system makes it easy to acquire data directly into an Excel spreadsheet and allows a variety of test programming.

Chapter 3 Growth mechanism of EBID

3.1 Literature review

Since the first day when electron beam was found to be able to deposit materials on the irradiated area, achieving an understanding of this deposition process has been the focus of scientists and engineers in the related areas. Through the long journey of pursuing this goal, people have realized that the growth is a multi-stage complex physical and chemical process. A number of widely accepted proposals for the mechanism of EBID will be depicted later on. People also found that the deposition process is controlled by a number of factors. These factors include beam energy, current density, gas pressure, substrate temperature, scan rate and deposition time. Changing any one of these factors can significantly change the growth rate and shape of deposits. The influence of these factors on the growth rate and deposit geometry will be detailed in this section. These factors also play important roles in determining the structure, composition and electrical properties of deposits. It will be discussed in the next chapter.

The scenario which is popular among most of the people in this field can be depicted as follows. The substrate surface is impinged by the precursor molecules flowing into the system. The molecules are adsorbed on the surface and will stay for a while, which is called resident time or mean life time. In the meantime, the incident electrons hit the substrate and get scattered within the substrate. The scattering events of the incident electrons generate backscattered electrons and secondary electrons. Secondary electrons have larger dissociation cross-section with the precursor gas because of low energy and are more likely to decompose the adsorbed precursor molecules when they are emitted from the surface. The electron-irradiated area is soon depleted of the precursor gas and a concentration gradient is formed between the depletion area and its neighboring area. This concentration gradient drives the molecules from the neighboring area to the depletion area, which ensures the growth process can continue.

People have explored various experimental factors from the stance of reducing carbon contamination in electron microscopes in the early days and gaining control of the growth, structures and properties of deposit in recent years. These factors will be summarized below.

3.1.1 Beam energy

The growth rate was found to increase with a decreasing beam energy[20, 26, 53, 54]. Hoyle et al.[16] observed this trend and further investigated the deposition process at ultra-low beam energy by providing a retarding potential. He discovered that the growth rate increases as the beam energy falls and reaches the peak at about 0.1keV and then falls down after that.

Beam energy influences lateral growth, vertical growth and tip geometry of deposited materials. The diameter of the deposits grown in spot mode was generally observed to increase with a decreasing beam energy[17, 20, 38, 101]. However, there were different observations on the influences of beam energy on the lateral growth (or diameter). Lau et al.[42] found out that the deposit was thinner at lower beam energies because the penetration of electrons is shallower and less material is deposited along the outer sheath of the deposit. Shimojo et al.[56] reported that the accelerating voltage did not significantly change the size of the deposits in the range 2 ~ 30keV. Unlike the general observation that lateral growth decreases with beam energy, high beam energy stimulates vertical growth of deposit[29, 38, 101]. Further, it was reported that the vertical growth of the deposits dropped remarkably as the beam energy fell down below 10keV[17]. Schiffmann[17] investigated the influences of beam energy on the cone shape of the deposited tips. The result indicated that the cone half-angle decreased and the cone length increased as the electron energy went up.

3.1.2 Current density

Two types of growth behaviors have been reported as people studied the influence of current density on growth rate of deposition. The first type was that growth rate

decreased as current density increased[4, 15-21]. The second type was that growth rate was proportional to current density[4, 22-35]. As current density kept going up, the growth rate finally saturated. This is commonly interpreted as whether the flux can always form a monolayer on the surface or not by the model proposed by Scheuer et al.[33]. This concept was later developed into terms such as electron limited region and gas flux limited region, and was widely used. The experimental result presented by Schiffmann[17] showed the deposited volume increased, reached its maximum and fell off as the beam current increased from 0 to 200pA, which demonstrated a transition from electron limited region to gas flux limited region.

The diameter of the deposited fibers was reported to increase with current density[17, 20, 21, 38]. Schiffmann[17] studied the effect of beam current on tip shape of the deposits. The study showed that at low beam current the tip shape was roughly cylindrical with a conical top and at high beam current the tip was totally cone-shaped with a cylindrical shaft. Increasing the beam current led to a drop of tip length and cone length. However, an increase of the beam current resulted in a hike of tip diameter and cone half-angle.

3.1.3 Gas pressure

It is widely reported that the growth rate increases with gas pressure[23, 24, 29, 30, 38, 60-65]. It was reported that a lower gas pressure could lead to deposits with smaller diameter in the stage of nucleation[59, 102].

In addition, it was found that there exists a threshold pressure for film deposition to occur. Wang et al.[103] discovered that that to deposit a Cr film from CrO_xCl_y the precursor pressure had to pass a threshold value and the reaction could be reversed and thus the Cr film could be etched by adding Cl2 gas into the chamber.

3.1.4 Substrate temperature

It was reported that tungsten deposition happened when the substrate temperature was below 50°C and the deposited thickness increased to a great extent with decreasing substrate temperature[22]. Takahashi et al.[32] observed a similar result as well. That low substrate temperature was favorable for the deposition was explained by an increase of adsorption coefficient as the substrate temperature dropped.[26, 51]

3.1.5 Scan rate

Kohlmann-von Platen et al.[23] investigated the influences of dwell time (the time in which electron beam induces deposition) and loop time (the time for one cycle in which electron beam induces deposition and then be moved away from the spot) on the growth rate. The results showed that for a constant dwell time longer loop time led to higher growth rate and for a constant loop time longer dwell time led to lower growth rate, which indicates the growth rate was affected by the time in which the irradiated area could be replenished of precursor molecules.

3.1.6 Deposition time

The growth rate was found not to be constant throughout the whole deposition process. The results have shown that after a fast start the growth rate drops to a lower value[17, 18, 24, 27, 35, 42, 51, 63, 85, 104]. Silvis-Cividjian et al.[58] pointed out the deposition followed a growth process of nucleation, fast growth and saturation.

Some studies also showed the vertical growth keeps increasing with deposition time while the lateral growth stops after a while[17, 18, 104, 105].

3.2 Theoretical background

3.2.1 Electron-solid interaction

After the beam electrons reach the specimen surface, they will pass through the surface and experience a series of scattering events including both elastic and inelastic scattering with atoms of the specimen. These scattering events cause successive energy deposition of the incident electrons to the specimen, forming an interaction volume of the beam electrons in the specimen. Both scattering events generate a large variety of signals. Here only backscattered electrons (BSE) and secondary electrons (SE) will be discussed because they are of interest in EBID.

3.2.1.1 Interaction volume

The interaction of electrons in specimen can be visualized by irradiating electron-sensitive polymers like methylmethacrylate (PMMA) which makes the polymer solvable in a suitable solvent[1]. The results by such etching show that the interaction volume has a pear-like shape as shown in Figure 3.1. Ford low atomic number materials like PMMA, the electrons tend to undergo relatively more inelastic scattering as they initially penetrate into the solid, which cause the “neck” region of the volume. As the electrons lose energy to the specimen, elastic scattering becomes more dominant and the electrons deviate from their original direction of travel and this lateral spread contributes to the “bulbous” region of the pear-shaped interaction volume.

The linear dimensions of the interaction volume decreases with atomic number at a given beam energy. In materials of high atomic number, the electrons undergo more elastic scattering per unit distance and the mean scattering angle is greater. The electron trajectories are thus more deviating from the initial direction of travel and reduce the penetration in the materials. In the same logic, the electron trajectories in materials of low atomic number have a deeper penetration and less deviation.

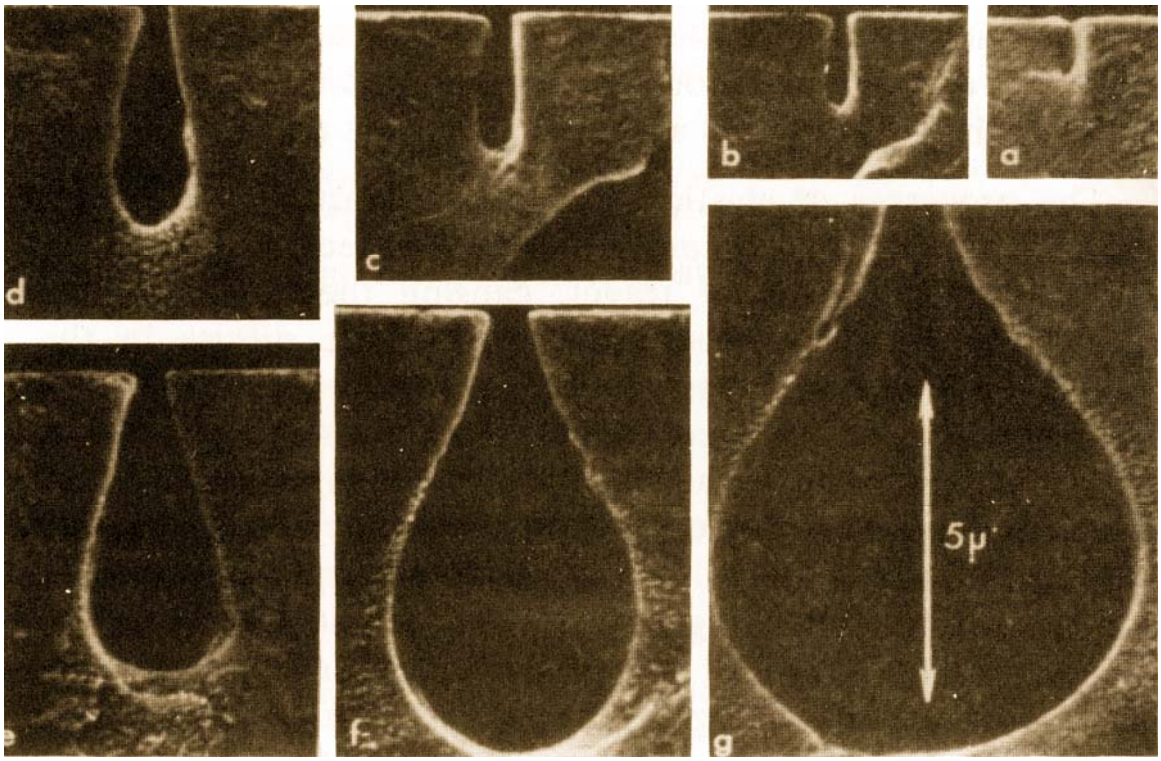

Figure 3.1 Direct Visualization of Interaction Volume

A series of electron photographs present direct visualization of the interaction volume in PMMA. In (a) through (g), the electron dose is the same, but the etching time is increased progressively to reveal successively lower energy deposition (radiation damage) levels[1]

The size of the interaction volume is strongly dependent on the energy with which the electrons interact with the specimen. At higher energy, the electrons can travel to greater depths. However, the shape of the interaction volume does not change significantly with beam energy since the lateral and depth dimensions scale in a similar way with beam energy.

As the tilt angle of a specimen increases, the interaction volume becomes smaller. This is because the forward scattering causes the electrons travel near the surface, which reduces the travel distance in depth.

3.2.1.2 Backscattered electrons

Backscattered electrons are not a special type of electrons but all electrons reemerging from the specimen surface which is positively biased by +50V. For example, if the beam current is measured in a Faraday cage and the beam electrons are bombarding a copper specimen biased by +50V, a large percentage of the incident electrons are absorbed by the specimen and the rest are scattered out of the specimen. These re-emergent electrons are then collectively known as backscattered electrons. There are two types of backscattered electrons: BSEI which are beam electrons suffering high elastic-scattering angles and promptly leaving the specimen in the immediate vicinity of the beam impact area and BSEII which are beam electrons suffering multiple elastic scattering whose cumulative effect brings a significant fraction back to the surface. BSEII are the dominant part of the total BSE and are emitted relatively uniformly over a much larger area whose diameter is similar to the Kanaya-Okayama range of the beam below the surface.

The backscatter coefficient η, the ratio of the backscattered electrons to the incident electrons, is found to increase with atomic number. This is straightforward from the nature of backscattering.

The backscatter coefficient is relatively insensitive to beam energy compared to the strong dependence of the interaction volume on beam energy.

The backscatter coefficient increases with the tilt angle of the specimen because as the tilt angle increases the tendency of the electrons to undergo forward scattering causes them to travel closer to the surface.

3.2.1.3 Secondary electrons

Secondary electrons are defined as those electrons emitted from the specimen with energy less than 50eV, which is an arbitrary cutoff. The energy spectrum of all emitted electrons plotted over the range 0 to E_0 (the energy of the incident electrons) should be similar to that shown in Figure 3.2 and in region III a sharp increase of emitted electrons is found at about 3-5eV. The increase in emitted electrons forming region III is due to secondary electron emission. Secondary electrons emission has been interpreted with the following theories. In metals secondary electrons are generated from excitation of valence electrons by incident electrons[106-109]. In non-conducting materials secondary electrons are generated from ionization of bound electrons by primary electrons[108, 110, 111]. For secondary electron emission in both metals and non-conducting materials plasmon decay plays an important role. Chung and Everhart[112] pointed out that an important source of secondary electrons may arise from the decay of long-wavelength surface and volume plasmons via near vertical interband transition. Kanaya et al.[110] and Grais and Bastawros[111] added that in insulators secondary electron emission is due to combination of ionization loss in the first collision and plasmon loss for the escaping secondary emission.

Secondary electrons are generated throughout the interaction volume of the beam electrons in the specimen but only those generated within the mean escape distance from the surface can come out. The mean escape distance is about 5λ, where λ is the mean free path of the secondary electrons[113] and is about 1 nm for metals and up to 10 nm for insulators. There are two types of secondary electrons: SEI which are generated by the incident electrons as they enter the specimen and SEII which are generated by the backscattered electrons as they exit. The schematic diagram is shown in Figure 3.3. In general, the ratio of SEII to SEI is of the order 3 or 4[113]. The ratio of SEII and SEI has

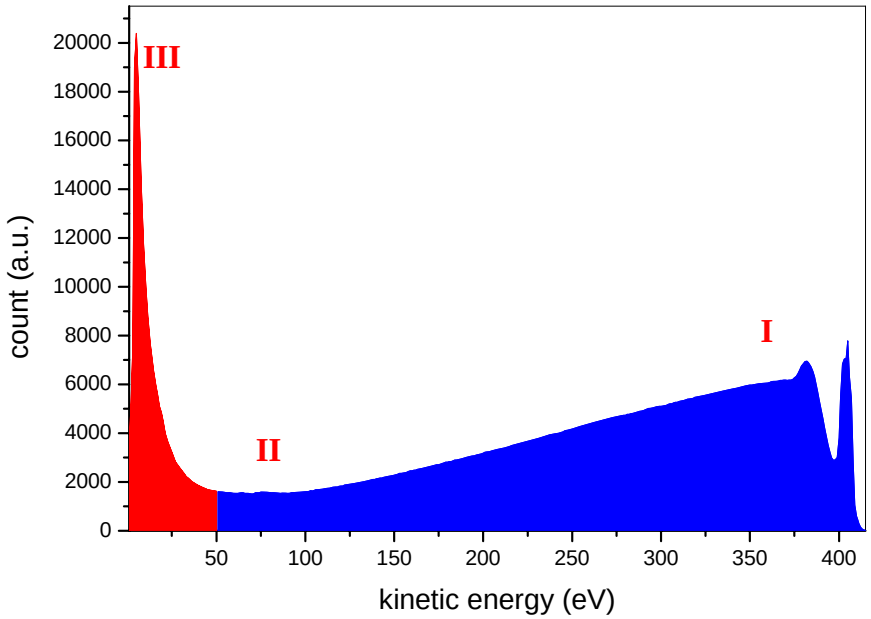

Figure 3.2. Energy Spectrum of Emitted Electrons

A diagram presents electron emission spectrum generated by beam electrons from a substrate which includes backscattered electrons (regions I and II) and secondary electrons (region III) (Courtesy of Yinghong Lin)

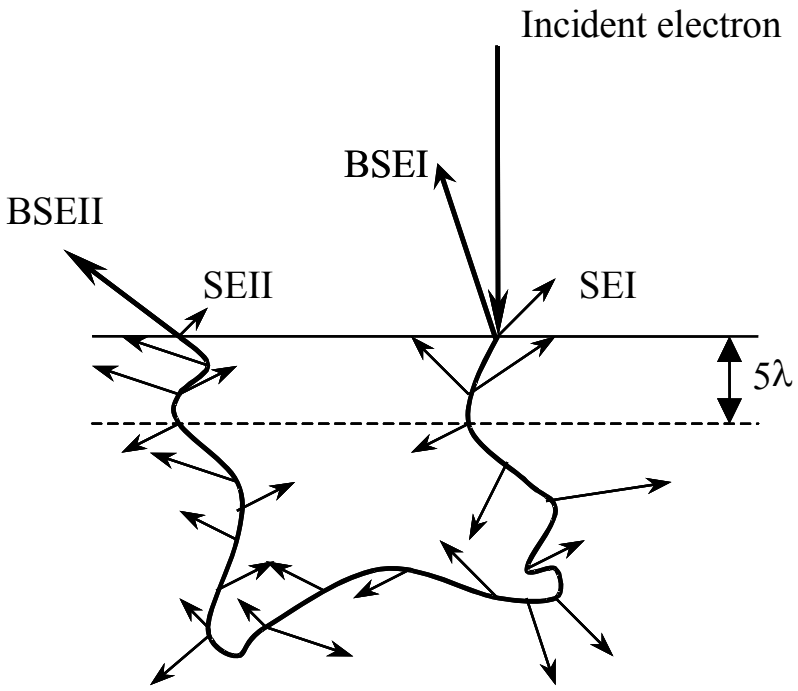

Figure 3.3 Origin of SE and BSE

A schematic diagram of the origin of the two sources of secondary electrons and backscattered electrons in the substrate.

a strong dependence on atomic number. In high atomic number materials SEII dominate while in low atomic number materials SEI do.

Unlike backscattered electrons whose coefficient strongly depends on the atomic number of the specimen, the experiments performed on conventional instruments show secondary electrons coefficient is relatively insensitive to composition and fails to show any strong dependence on atomic number. However, measurements from our group and other individual[114], made in ultrahigh-vacuum conditions with in situ surface cleaning of the specimen, suggest a much stronger compositional dependence. At low beam energies, this compositional dependence is more manifest since secondary electron coefficient usually reaches its peak at low beam energy range.

The secondary electron coefficient has a strong dependence on beam energy. Starting from zero beam energy, the secondary electron coefficient rises with beam energy, reaching unity at about 1 keV. A peak, slightly above unity above metals and up to 5 for nonmetals, occurs in the range 1-2 keV. As the beam energy further increases, the coefficient decreases and gets back to unity in the range 2-3 keV. It continues to drop and eventually approaches zero as the beam energy approaches infinity.

Secondary electron coefficients are found experimentally to increase with the tilt angle of the specimen, following a secant relationship[115] as expressed in Eq. 3.1.

$$\delta(\theta) = \delta_0 \sec\theta \qquad 3.1$$

3.2.2 Gas-surface interactions

3.2.2.1 Adsorption and desorption

When a gas molecule approaches a surface, it will feel an attractive force. As the distance between the molecule and surface continues to decrease, the magnitude of this attractive force initially increases and then passes through a maximum and falls off. Eventually this attractive force becomes a repulsive force, as the molecule is too close to

the surface. A typical plot of potential energy vs. distance for such a system, as shown in Figure 3.4, indicates that a potential minimum exists near the surface. When a gas molecule approaches the surface, it will reach and be trapped in a position of minimum potential energy. The mean life time for adsorption is given by Eq. 3.2

$$\tau = \tau_0 \exp\left(\frac{E_{des}}{kT}\right) \qquad 3.2$$

in which τ_0 has a magnitude of 10^{-16} to 10^{-9} sec, E_{des} is the magnitude of the potential well shown in Figure 3.4, k is Boltzmann's constant, and T is the ambient temperature. This implies that the deeper the potential well, that is, the greater magnitude of E_{des}, the longer the mean life time for adsorption.

Adsorption, according to the type of attractive forces, can be grouped into two categories. Adsorption processes involving forces of the van der Waals, or dispersion, usually of magnitude ranging from 0.001 to 0.1 eV, are called physisorption processes. Adsorption processes involving forces of hydrogen bonding, covalent chemical bonding, or metallic bonding, of magnitude ranging from 0.1 to as high as 10 eV, are referred to as chemisorption processes.

Three models have been developed in order to use the fundamental equation above to describe the adsorption behavior in any real system. The first model, the Henry's law model, assumes that all molecules adsorb independently of one another, that is, all positions on the surface are equivalent, independent of where an incoming molecule strikes. The second model, the Langmuir model, is basically the same as the Henry's law model. The only difference is that the Langmuir model says that τ has a finite value for atoms striking unoccupied sites and zero value for atoms striking occupied sites. This implies that the total adlayer coverage can never exceed the total number of sites, and the coverage is limited to a single monatomic layer. Brunauer, Emmett and Teller[116] proposed the B.E.T. model of the adsorption process to treat multiplayer adsorption. The detailed assumptions of this model will not be given here.

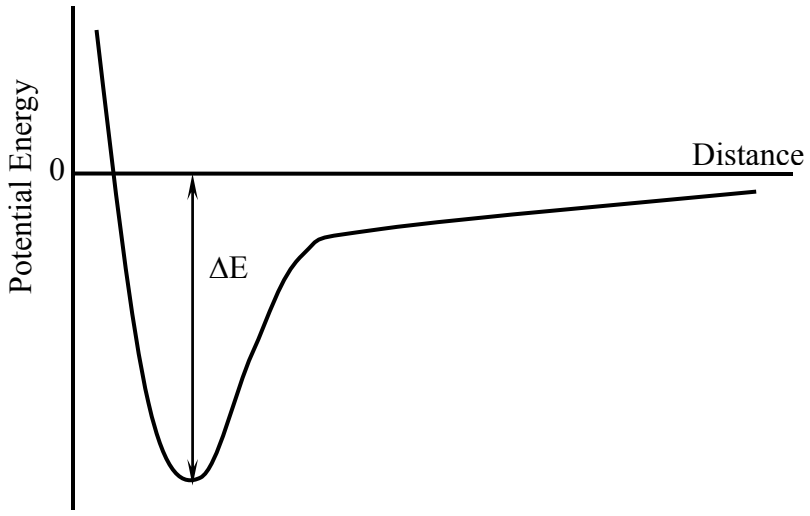

Figure 3.4 Distance Dependence of Potential Energy

A schematic diagram shows system potential energy as a function of the distance between an approaching gas molecule and the surface.

The interested readers can check the related readings[116, 117].

Physisorption processes are usually associated with nonspecific forces. In systems of this sort, the interactions among the adsorbed species, which is called lateral interactions, are comparable in strength to the interactions with the substrate atoms. In addition, on any real surface the adsorption potential well depth will not be the same for all adsorption sites. There will be a variation in the well depth, reflecting the nature of the surface. This variation arises from the disturbances associated with surface heterogeneity. There are three types of behaviors for adsorbed species depending on the amplitude of the variation of the surface potential relative to kT: mobile adsorption, in which the potential variation is small compared to kT, and localized adsorption, in which the variation is larger than kT but not large enough to stop surface diffusion, and immobile adsorption, in which the surface diffusion is prohibited by the very large potential variation. In many cases, this potential variation is small, resulting a highly mobile adsorbed phase.

Compared to physisorption, the binding forces in chemisorption are more specific, both in terms of which adspecies-surface species combination lead to chemisorption, and in terms of the preferred positions of the adspecies relative to the surface atoms and to each other. Chemisorption could be nondissociative and dissociative. In the case of dissociative chemisorption one must consider the possibility of desorption as individual atoms and the possibility of recombination to reform the molecule and subsequent desorption of this species.

Desorption is a phenomenon and process opposite to adsorption. Desorption process accompanies adsorption process in a system no matter whether it is equilibrium or unequilibrium. Statistically adsorbates leave the surface after a mean life time for adsorption. The equilibrium state is a dynamic process in which the same amount of species adsorb onto the surface as that leaving the surface. Desorption can be enhanced by many factors, such as substrate temperature and almost all of the energetic particles. Electron stimulated desorption (ESD) is a good example in which adsorbed species are pumped up to an excited state by electron impacts and the system will relax by the

excited species leaving the surface, thus lowering the system potential energy and transferring equivalent kinetic energy to the excited ones.

3.2.2.2 Surface diffusion

In the case of chemisorption, adsorbed species are situated at the bottom of a potential well in thermal equilibrium with the underlying solid. Thermal fluctuations tend to drive these adsorbates back into the gas phase. However, the activation energy for desorption is in the range 1-5 eV and the rate is quite small. Another possibility is the adsorbates hop from one well to another and the energy barrier for this motion is less than that of desorption. Since diffusion is an activated process, it is expected to follow an Arrhenius form:

$$D = D_0 \exp\left(-\frac{E_{dif}}{RT}\right) \qquad 3.3$$

in which D is the diffusion coefficient, D_0 the diffusion prefactor, E_{dif} is the activation energy for diffusion, R is the gas constant and T is the temperature.

3.2.3 Surface chemical reactions

3.2.3.1 Reaction steps

Surface reactions can be classified into three categories: etching, deposition and catalytic reactions. In etching reactions, the induced gas reacts with the surface to produce new species containing atoms from the surface. This new species then returns to the gas phase and the surface is progressively consumed. In deposition reactions, material is deposited on the surface, with or without a decomposition reaction, to extend the surface or to form a solid phase of a new chemical species. In catalytic reactions, the surface is not participating in the reaction, but serving as a site at which the reaction rate is enhanced compared to the rate in the gas phase.

All classes of surface reactions can be treated in terms of a sequence of steps. Generally the steps include physical adsorption from the gas phase, chemisorption, surface diffusion to the reaction site, the actual reaction step, surface diffusion away from the reaction site, return to a physisorption state, and finally desorption into the gas phase. Figure 3.5 is a schematic diagram illustrating all the possible steps. Not all of these steps will be involved in any given reaction, and in many cases only one of these steps will control the overall reaction rate. All steps except the actual reaction step have introduced previously. The actual reaction step is a complex process that involves multiple intermediate steps coexisting at the same time.

3.2.3.2 Cross-section for dissociation

Electrons with energy of several tens of electron volts have a de Broglie wavelength of about 0.1 nm. This wavelength is comparable to molecular and atomic dimensions. When electrons pass through gas molecules, electrons from the gas molecules may be promoted to a higher level and even ejected from the molecules. Direct attachment of the incident electrons to the molecules cause a transfer of momentum and energy from the incident electrons to the molecules, usually leading to fragmentation (i.e. dissociative ionization). The cross-section for ionization is a function of electron energy. Figure 3.6[118] is a plot of the electron-impact ionization cross-section for silicon tetrafluoride (SiF_4) from 5 to 5000 eV, based on the Binary-Encounter-Bethe (BEB) model. The plot shows as the incident electron energy starts to increase from a threshold value, the cross-section for ionization increases with the incident electron energy and reaches its peak at about 100 eV and then starts to fall off. This is a universal trend for electron ionization cross-section and all the atoms and molecules follow that.

3.2.4 Theoretical models for EBID

Scheuer et al.[33] proposed a simple phenomenological model of the deposition process based on mass balance equation. The model assumes that only the molecules

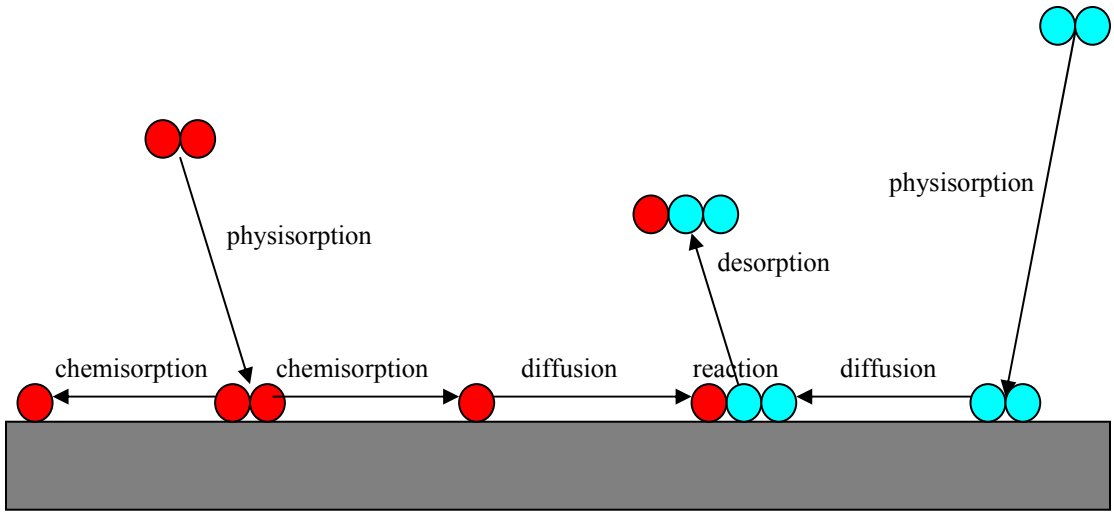

Figure 3.5 Possible Steps of Surface Chemical Reaction

A schematic view of the possible steps, which include physisorption, chemisorption, diffusion, reaction and desorption, involved in a surface chemical reaction between two molecules.

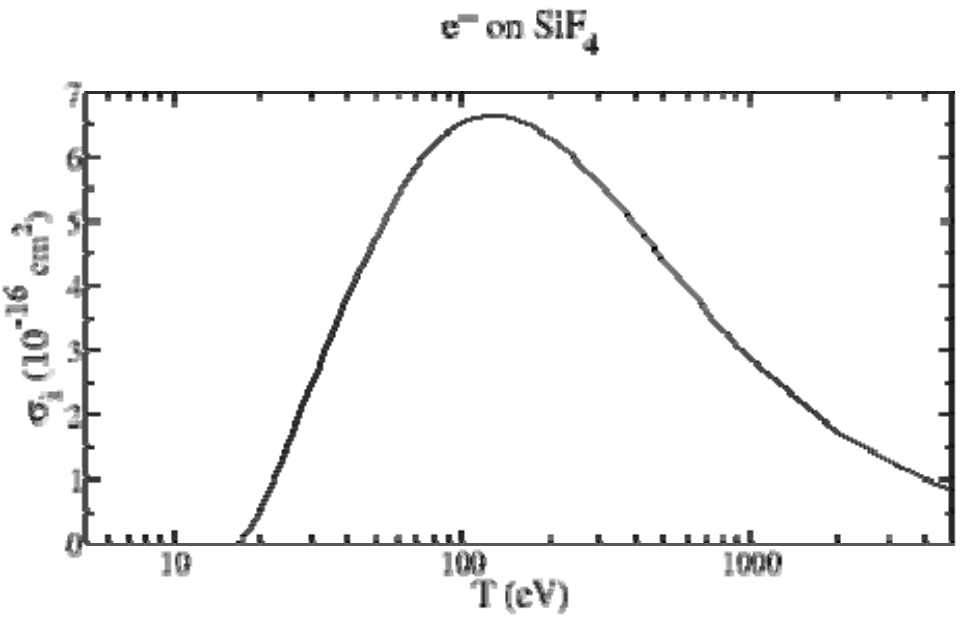

Figure 3.6 Ionization Cross-section for SiF_4

A diagram of the electron-impact ionization cross-section for silicon tetrafluoride (SiF_4) from 5 to 5000 eV, calculated by using the Binary-Encounter-Bethe (BEB) model.

adsorbed on the surface undergo dissociation by electron irradiation. Thus only a monolayer of adsorbates contributes to the growth. The adsorption rate is given by

$$\frac{dN}{dt} = g \cdot F \cdot \left(1 - \frac{N}{N_0}\right) - \frac{N}{\tau} - \sigma \cdot N \cdot f \qquad 3.4$$

in which N is the density of adsorbed molecules on the substrate surface, g the sticking coefficient, F the molecular flux density arriving at the surface, N_0 the molecule density of a monolayer, τ the mean lifetime of an adsorbed molecule, σ the cross section for dissociation of the adsorbed molecules under electron irradiation, and f the electron flux density. The layer growth rate R follows as

$$R = \left(v \cdot N \cdot \tau\right) \cdot \sigma \cdot f \qquad 3.5$$

in which v is the volume occupied by a dissociated molecule or its fractions.

3.3 Motivation

EBID has become a promising technique for fabricating nanostructures due to its high resolution and its simple and contamination-free procedure. However, its fundamental mechanism and kinetics are not quite understood, which makes its way to realistic applications in industry challenging. Most of the effort that has been done was focused on how the experimental factors, such as beam energy and current density, influence the growth behavior of EBID. People try to interpret the results from the perspective of their specialty, and as a result various mechanisms have been proposed. Among them two questions stand out as the most controversial but most significant ones.

The first question is where does the dissociation reaction happen, in the gas phase or on the substrate surface. This determines whether we can adopt Scheuer's mass balance model, as introduced previously, to describe the deposition process or not. Scheuer's model assumes that the dissociation takes place on the substrate surface, which is generally accepted. There are a few experiments supporting this assumption. Kunz et al.[119] ruled out the possibility that the nucleation occurs by gas phase dissociation

based on the observations that there were no apparent spreading of the deposition profile due to the isotropic flux of dissociated species from the irradiated gas volume and that no nucleation was found when a broad beam passed through the gas without striking the sample surface. Takahashi et al.[32] made the same suggestion based on a similar reasoning that the size of the structure should be much larger than that observed in the experiment because the decomposed atoms would travel in the gas phase with long diffusion path. Hirose and Sakamoto[120] designed a parallel-electron-incident-growth experiment and could not detect any signals of the desired material from the surface near the beam after irradiation, which indicated that gas-phase stimulation does not contribute to the growth. However, there exist some experimental evidences clinging to the other side. Hiller[4] pointed out that the possibility of dissociation in gas phase could not be excluded because the partial pressure within the restricted volume near the specimen was reduced rapidly by the action of electron beam. Foord and Jackman[121] reported that $Fe(CO)_5$ does not adsorb to clean Si at 300 K while iron deposition from $Fe(CO)_5$ at this temperature was observed by the other researchers[119], which indicates that the initial dissociation may be in the gas phase, over the sample. So far the proposal that the dissociation takes place on the surface is more plausible than the proposal sticking to gas-phase-dissociation, though the second one has not been completely excluded. More experimental proofs need to be obtained to endorse the first proposal.

The second question is what particles participate the dissociation reaction, secondary electrons, or backscattered electrons, or primary electrons (PE). Secondary electrons are considered most likely to decompose the gas molecules because their low energy gives them the largest cross-section for dissociation of the gas molecules[122]. Backscattered electron is also a possible candidate because the experimental evidences show that the sizes of the deposited structures are larger than the diameters of electron beam. In electron microscopy, this is called broadening effect which is usually caused by backscattered electrons. Backscattered electrons having a large energy can travel a long distance and come out of areas outside of the irradiated region. Primary electrons with energy of keV range have very small cross-section for dissociation of the precursor

molecules. However, some researchers argue that primary electrons can still produce a good yield of dissociation since the number of primary electrons is much larger and this can compensate the low cross-section for dissociation. Though generally secondary electrons are believed to play the role, experimental evidences have not ruled out backscattered electrons and primary electrons yet.

The purpose of this work is to provide experimental evidence to answer these two questions and to discover the correlation between the experimental factors and the physics of EBID. This research will benefit not only experimental applications which require a deeper understanding of the nature of EBID to control the deposition process by properly adjusting the factors but also simulation applications which need to mimic the true physics behind EBID.

3.4 Experiments and discussions

This section consists of two subsections. The first one was designed to find out the place where the dissociation reaction happens. The second one was designed to find out what particles, SE or BSE or PE, are driving the deposition.

3.4.1 Verification of assumption 1

3.4.1.1 Introduction

As stated previously, experimental evidences have shown that the dissociation occurs more likely on the specimen surface than in the gas phase. This point is supported by the author of this work. Therefore, experiments were required to provide more proofs to support the point that the dissociation takes place on the surface instead of in the gas phase. Here a set of experiments was designed to study how the growth rate varies with substrate temperature. It is believed that the growth rate should change with substrate temperature significantly and the growth rate should fit an Arrhenius relationship with the substrate temperature if the dissociation occurs on the sample surface. Whereas the

substrate temperature should have no influence or little influence on the growth rate if the proposal that the dissociation takes place in gas phase stands.

With respect to the influence of substrate temperature on the growth, the literature review has revealed a number of experiments that were carried out to investigate this subject[22, 26, 40, 60, 66]. A common observation that the deposited thickness increases to a great extent with decreasing substrate temperature has been reported[22, 26, 27, 60, 66]. Another interesting observation was that in the case of WF_6 precursor the W pattern was deposited at below ~50 °C substrate temperature while etching rather than deposition was observed on a silicon oxide thin film on the silicon substrate at above ~50 °C substrate temperature[22]. All these suggest that substrate temperature does affect the growth rate.

3.4.1.2 Experimental details

The experiments were performed on the Hitachi S-4300SE/N variable pressure scanning electron microscope as described in Chapter 2. The needle was positioned at a distance of 3mm from the substrate with an angle of 30° ~ 45°. Tungsten hexafluoride (WF_6) was chosen as the precursor gas and stored in the reservoir at 25°C, at which temperature it has a vapor pressure of around 1.15×10^5 Pa. The pressure in the microscope chamber was usually maintained below 8.0×10^{-4} Pa but was raised to a range 5.0×10^{-3}~6.0×10^{-3} Pa when the gas was admitted. The deposition was performed on a germanium (Ge) substrate, chosen to permit in-situ thickness determinations to be made by X-ray spectroscopy without the problem of overlap between the Si-K and W-M X-ray lines. The substrate was mounted on the EMITECH K25X Peltier cooling stage which gave a control of substrate temperature within a temperature range -30°C ~ 75°C.

Two groups of experiments were carried out by exposing the substrate with an electron beam in spot mode in the presence of WF_6. In the first group, an array of nanodots, as illustrated in Figure 3.7, was fabricated on the substrate for studying the temperature influence on the deposition at a fixed beam energy and varying beam

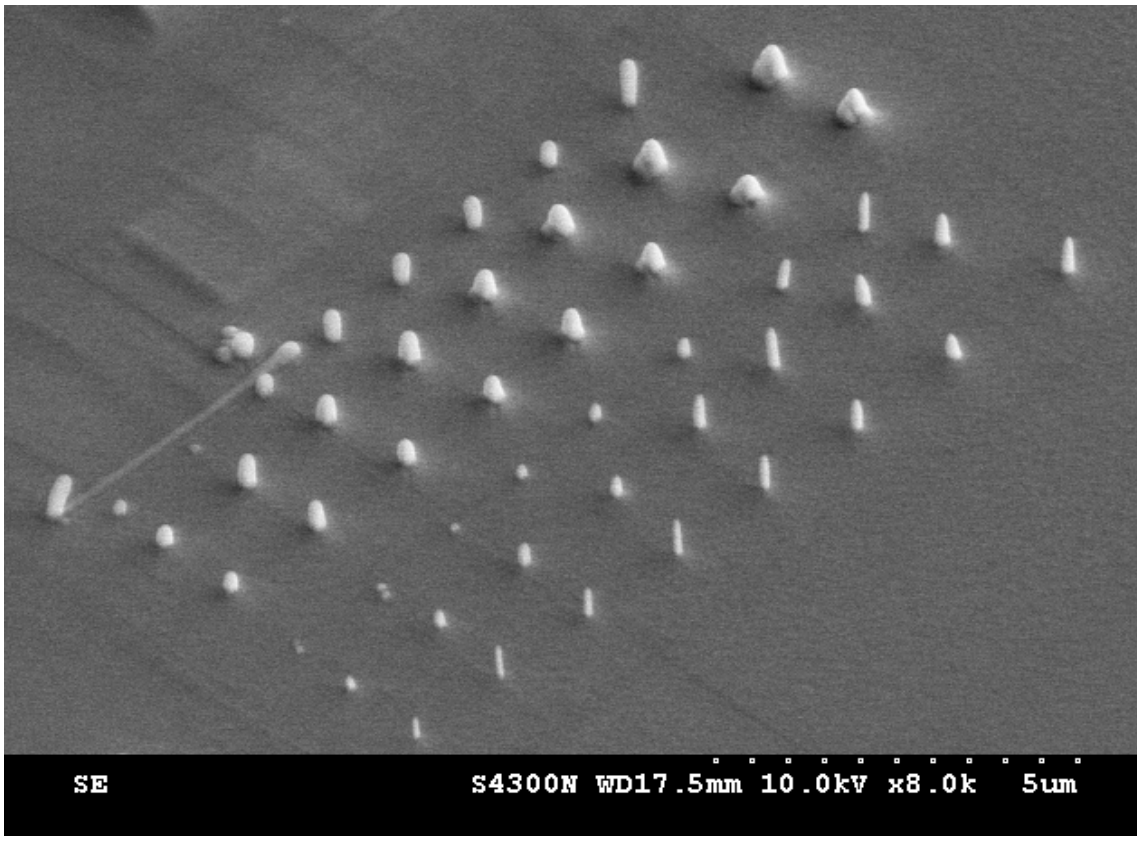

Figure 3.7 Electron Micrograph of W Nanofibers

An electron micrograph of an array of W nanofibers grown for studying the temperature influence on the deposition at a fixed beam energy and varying beam currents.

currents. Beam energy of 20 keV and beam currents of 3430, 403 and 51 pA were employed. For each beam current, a line of nanodots was fabricated under different substrate temperatures for an exposure time of 60 seconds. In the second group, another array of nanodots was deposited for studying the temperature influence on the deposition at a fixed beam current and varying beam energies. A beam energy of 5, 10, 20 and 30 keV and beam current of 140 pA were employed. The beam current of 140 pA was obtained by collecting the sample current via the grounding path before deposition for beam energy of 5, 10, 20 and 30 keV respectively and saved to the system and was reloaded during deposition. For each beam energy, a line of nanodots was fabricated under different substrate temperatures for an exposure time of 60 seconds. For both groups, the substrate temperature was changed from 75°C to -30°C in steps and for each substrate temperature a period of 3~5 minutes was allowed for stabilizing the substrate temperature. The chamber pressure was in a range 5.0×10^{-3}~6.0×10^{-3} Pa during the deposition and could be monitored by a Ferran Scientific Micropole^{TM} residual gas analyzer (RGA). In this work the pressure mentioned for EBID process was always referred to the base pressure, i.e. the chamber pressure and the local pressure was usually at least tens of times higher, depending on the distance and angel of the needle from the beam-irradiated area. The dimension of the deposits was measured from secondary electron (SE) image obtained by tilting the substrate under the electron microscope.

It is not yet clear how different the local temperature of the beam irradiated area was from the substrate temperature since the incident electrons deposit energy to the area. The direct measurement of local temperature change by electrons is impossible because there is no such a device that can provide enough spatial, temporal and thermal resolution. However, most of the work that has been done by analytical calculation[15, 51, 60, 123] and computer simulation[124] indicates that the temperature change caused by electrons can be negligible. Weber[125] investigated scattering of non-relativistic electrons in tip structure by using Monte Carlo simulation and found out that the pear-shaped spatial distribution of energy deposited in a flat surface is reduced to a much smaller volume when electrons scatter in a tip. As a consequence, the number of electrons leaving the

specimen after only a few scattering events is very high and the energy loss to tip structure should be much smaller than specimen with a flat surface. We also simulated the steady-state temperature profile of a tungsten nanofiber with height of 1000 nm and radius of 100 nm under irradiation of a 1.42 nA electron beam and the result showed that the largest temperature rise was less than 1 °C. Moreover, in the simulation only thermal conduction was considered and the black body radiation and the convection caused by the local gas flow were not included because of the complexity. This suggests that the real temperature rise would be lower than our simulation if those two means of heat dissipation had been considered. Therefore the temperature rise generated by electron irradiation was neglected in this study so that the local temperature of the electron beam irradiated area would be taken the same value as the cooling stage used in our experiment.

3.4.1.3 Results and discussion

A significant criterion to tell whether the dissociation happens on the surface or in the gas phase is the correlation between the growth rate and the substrate temperature. The growth rate should vary with the substrate temperature if the dissociation occurs on the surface. Otherwise, the growth rate should be independent of substrate temperature. For this purpose the growth rate should be measured for comparison. However the growth rate is not constant over the whole period. The literatures and our previous work indicate that the growth experiences a fast growth in the beginning which spans from 30 s to a few minutes depending on the beam current and then the growth rate slows down and eventually saturates. Besides, unlike thermal CVD which requires an induction time for nucleation to occur, in EBID the growth begins immediately after the electron beam is turned on[126]. In this work the growth rate was estimated by averaging the deposited volume over the deposition time of 60 s because it is very likely that within this 60 s the deposition was undergoing a fast growth and the growth rate had not decreased yet. Both our data shown in Figures 3.8 and 3.9 and the previous work[22, 26, 40, 60] confirm that the growth rate increases with a decreasing substrate temperature, and this would be an important supporting evidence for the proposal that electron beam induced deposition is a process involving adsorbed molecules on the surface.

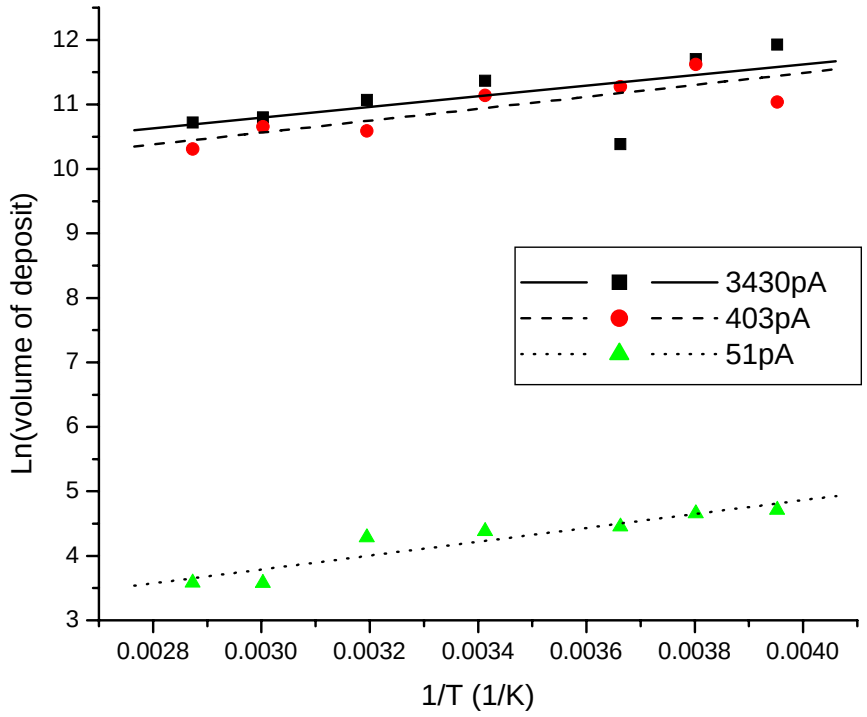

Figure 3.8 Temperature Dependence of Growth Rate under Varying Beam Currents

A plot of natural logarithm of the deposited volume vs. the inverse of the substrate temperature under varying beam currents (51, 403 and 3430pA) and 20keV.

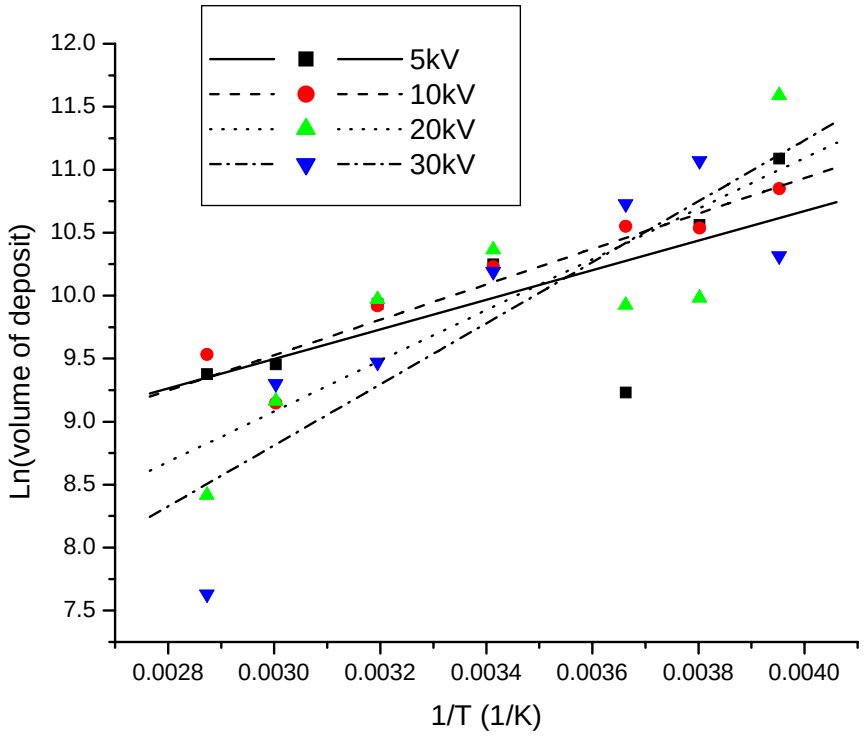

Figure 3.9 Temperature Dependence of Growth Rate under Varying Beam Energies

A plot of natural logarithm of the deposited volume vs. the inverse of the substrate temperature under varying beam energies (5, 10, 20 and 30keV) and 140pA.

Since the adsorption-desorption process is involved in EBID, the growth rate should be a function of the mean lifetime of adsorbed molecules. The mean lifetime τ is significantly dependent on the substrate temperature, as indicated by Eq. 3.2. Combining Eqs. 3.2 and 3.5 gives

$$R = \left(\nu \cdot N \cdot \tau_0 \cdot \exp\left(\frac{E_{des}}{k \cdot T} \right) \right) \cdot \sigma \cdot f \qquad 3.6$$

in which R is the growth rate, v the volume occupied by a dissociated molecule or its fractions, N the density of adsorbed molecules on the substrate surface, τ_0 the coefficient with a magnitude of 10^{-16} to 10^{-9} sec, E_{des} the activation energy for desorption, k Boltzmann's constant, T the substrate temperature, σ the cross section for dissociation of the adsorbed molecules under electron irradiation, and f the electron flux density. Eq. 3.6 explains why the growth rate fell off as the substrate temperature went up, as shown in Figures 3.8 and 3.9.

Two geometric types of deposits were found in this study. The first type, mostly found at a beam current of 403 pA and lower, has a cylindrical body and a conical top, as shown in Figure 3.10(a). The second type, mostly found at a beam current of 403 pA and higher, has only a conic body, as shown in Figure 3.10(b). Because of these different shapes, volume of the deposits, instead of height of the deposits, was measured to calculate the growth rate. Figures 3.8 and 3.9 depict a series of plots of the natural logarithm of the deposited volume vs. the inverse of the substrate temperature from the two experiments respectively. A significant linear trend was found in the plots, which agrees with the Arrhenius relationship deduced by Eq. 3.6. The desorption energies from the two experiments were obtained by measuring the slope of the Arrhenius plots and were plotted individually in Figures 3.11 and 3.12. It can be seen that the desorption energies are in a range between physisorption (~0.01 eV) and chemisorption (~1 eV), which supports the significant role of the adsorption-desorption process in interpreting the growth mechanism and thus supports the assumption that the dissociation occurs in the layer of molecules adsorbed on the surface. However, our result is much lower than

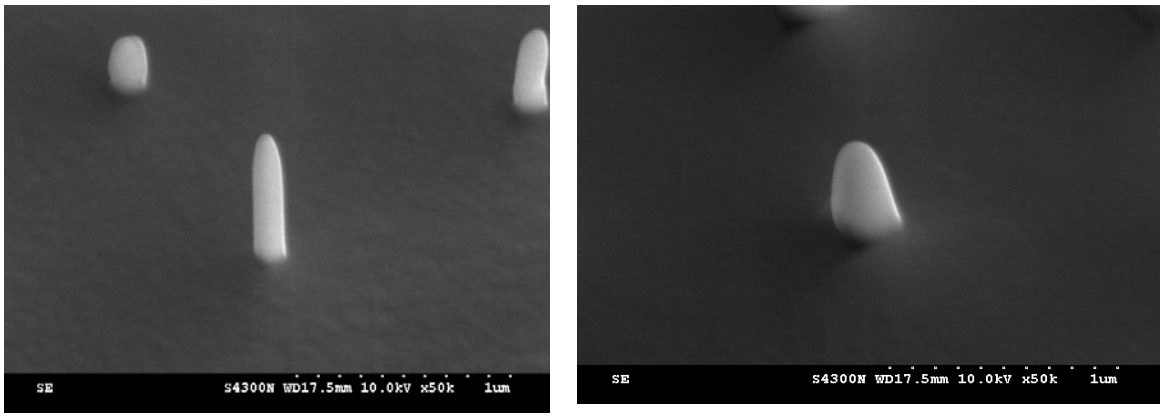

(a) (b)

Figure 3.10 Geometries for Nanofibers

Electron micrographs of two types of geometry for the nanofibers (a) the first type, mostly found at a beam current of 403 pA and lower, have a cylindrical body and a conical top; (b) the second type, mostly found at a beam current of 403 pA and higher, have only a conic body.

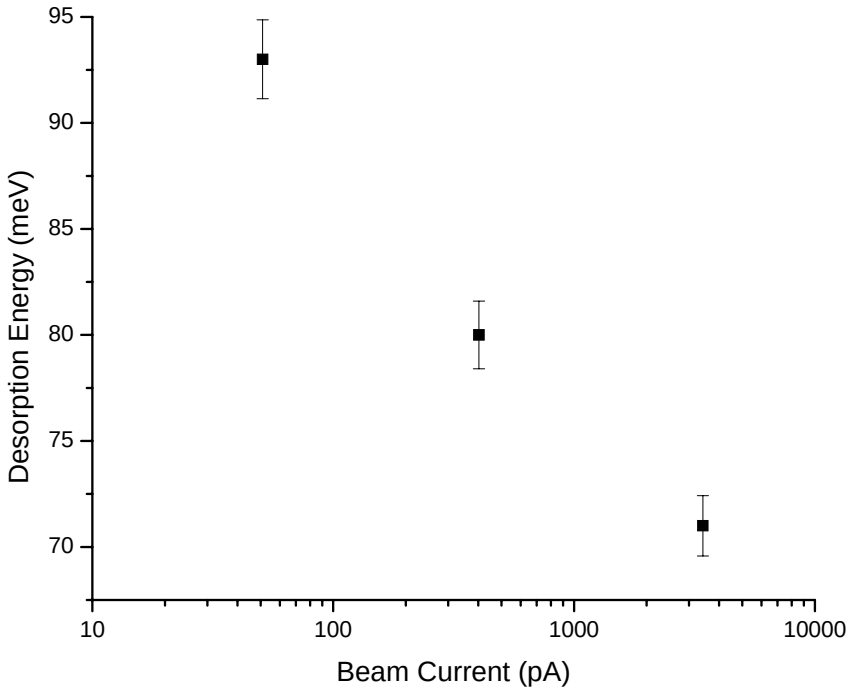

Figure 3.11 Beam Current Dependence of Pseudo Desorption Energy

A plot illustrates the variance of the pseudo desorption energy obtained from Figure 3.8 with the beam current at a beam energy of 20keV.

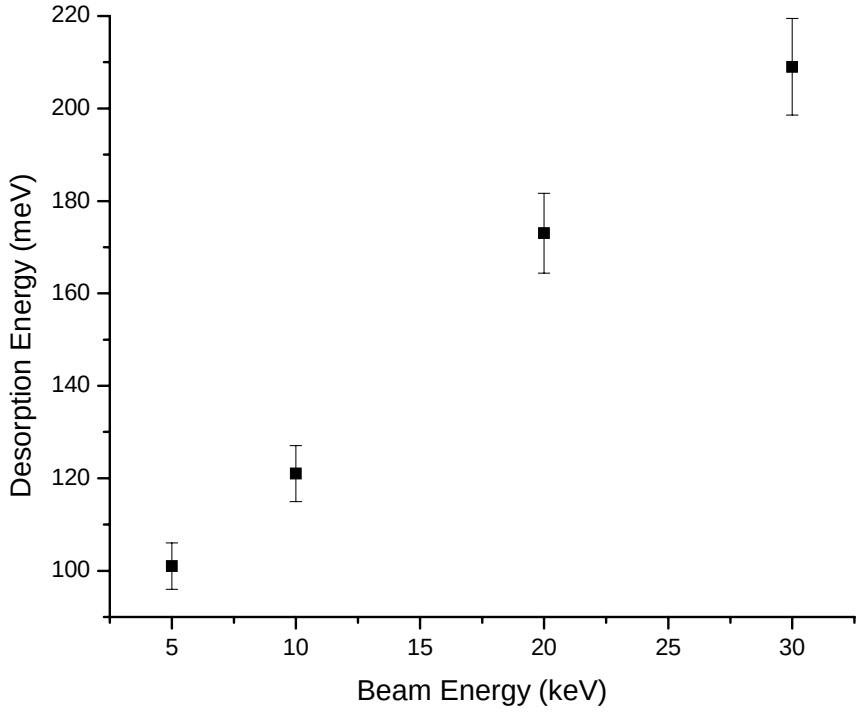

Figure 3.12 Beam Energy Dependence of Pseudo Desorption Energy

A plot of the variance of the pseudo desorption energy obtained from Figure 3.9 with the beam energy at a beam current of 140pA.

the desorption energy reported by Jackman et al.[127, 128] and Chen et al.[129]. Jackman et al.[127, 128] performed thermal desorption analysis and measured the thermal desorption energy of WF_6 on Si surface to be 0.35 eV, which agreed with 0.322 eV calculated using Redhead's formula[130]. The temperature programmed desorption (TPD) experiment conducted by Chen et al.[129] indicated the activation energy for WF_6 to desorb from W surface was 0.374 eV.

It is noted that the desorption energy which was obtained from the deposition at beam energy of 20 keV and beam current of 140 pA, as shown in Figure 3.12, does not fall in the desorption energy range estimated from the deposition at beam energy of 20 keV and beam current ranging from 51 to 3430 pA as shown in Figure 3.11. The possible reason for this inconsistency is that the two groups of deposition were not carried out within the same time period. The second group was done about one month after the first one. There probably was a significant change on the surface of the substrate in the second group because of the following reason. The surface of the substrate in the first group was fresh and clean. It was cleansed with Acetone before deposition. During deposition the surface was flooded with WF_6 which could attack substrates such as silicon and germanium through dissociative adsorption even at temperature as low as 150 K[127], which produces a tungsten monolayer on the surface. After deposition the substrate was removed from the vacuum chamber and exposed to the ambient environment in which the residual WF_6 molecules on the surface quickly reacted with water vapor in the air forming HF to erode the Ge surface. This led to W and subfluorides of W together with fluoride complex of germanium formed on the substrate surface. Moreover, during the time period before the substrate was used again for the second group of deposition, lots of contamination was adsorbed on the surface because the sample was not kept in a vacuum environment. All these could cause a change to the chemical property of the surface, which in return caused a change to the desorption energy and surface diffusion rate. Since for both groups no matter the substrate was a fresh and clean Ge surface or a contaminated Ge surface with hydrocarbon and tungsten subfluorides it took only an extremely short second to form a tungsten monolayer at the beam spot, the adsorption-

desorption process on the beam spot should be the same since it only involved with the same adsorbed species and the new tungsten surface. It is speculated that surface diffusion dominated the gas supply and from the fresh surface in the first group to the contaminated surface in the second group the surface diffusion might change the growth from the electron-limited region to the gas-limited region. However, in this work the interest was focused on the comparison within each group, not between the two groups. This means that the inconsistency does not affect how we compare and interpret the data within each group.

3.4.1.4 Further discussion

There are several possible factors responsible for why the desorption energies obtained from our experiment differ from the earlier researchers. First, unlike the TPD experiments carried out by the other groups where the subfluorides WF_x (x=1-5) were not formed until the critical temperature of each which is much higher than the room temperature was reached, in EBID the low-energy electrons assist to break the bonds and the activation energy of decomposition can diminish drastically[131] and all of the subfluorides WF_x could be formed around the room temperature. The surface in which we are interested also transited from germanium to tungsten once the deposition started. This led to a complex time-dependent adsorbate-substrate system. Whereas the analytic equations we adopted are based on a simplified model. This model assumes that the decomposition is one-step reaction in which WF_6 decomposes directly into W and F_2 instead of a multi-step pathway in which WF_6 could evolve into a series of subfluorides WF_x, F^- and F_2 and that the adsorbate-substrate system does not change throughout the experiment. Therefore the activation energies measured in this work were the mean activation energies of both the precursor WF_6 and intermediate products WF_x per se. Second, though we could neglect electron beam induced heat in this work, electron stimulated desorption (ESD), which played an important role in determining the residence time of adsorbed molecules as well as thermal desorption, should be considered. When the incident electrons hit a surface, electrons of a wide energy range will be emitted from the surface. Among them, SE, which are the electrons with energy below 50

eV, assist to dissociate the precursor molecules on the surface, and can also provide energy for desorption of the adsorbed species, which include the precursor WF_6, the intermediate products WF_x (x = 1-5), the radical F^-, the final by-product F_2 and the residue species from the chamber, from the surface. Since we are only interested in the adsorption-desorption process of the adsorbates which lead to the metal deposition, the 'adsorbed species' and 'adsorbed molecules' which are used in the discussion refer to WF_6 and WF_x, if not explained specially. In a review of ESD for studies of chemisorption, Madey and Yates[132] concluded that secondary electrons are capable of excitations leading to ESD since their energies are greater than ESD threshold energy (typically < 20 eV). The secondary electron excitation of a solid can cause changes to chemical states of a surface, especially a surface with an adsorbed layer. In fact all electrons with energy larger than the ESD threshold energy are capable of removal of adsorbates. However as ionization process ESD should follow the universal trend, as illustrated in Figure 3.6, that the ionization cross section arises from the threshold energy and reaches its peak at hundreds of eVs and tapers off after that. In EBID the incident electrons with energy of keVs generate two majorities of electrons. One is secondary electrons with energies below 50 eV and the other backscattered electrons (BSE) in keV range. It would be plausible to neglect the influence of BSE on ESD because of their small cross section. The adsorbed molecules are pumped to an excited level from a ground level by secondary electron excitation and the system try to relax by the excited molecules leaving the surface, thus lower the surface energy and impart kinetic energy to the excited molecules. These molecules will then appear in the gas phase and the desorption process is accelerated by secondary electron excitation. Therefore there were two desorption mechanisms, thermal desorption and ESD, in this experiment. In thermal desorption phonon, i.e. lattice vibration provides energy for adsorbed species to leave the surface while in ESD secondary electrons provide energy. Then an extra term E_{ESD} should be added into Eq. 3.6 to describe the effect of ESD and Eq. 3.6 becomes

$$R = \left(\nu \cdot N \cdot \tau_0 \cdot \exp\left(\frac{E_{des} - E_{ESD}}{k \cdot T} \right) \right) \cdot \sigma \cdot f \qquad 3.7$$

in which all terms are the same as in Eq. 3.6 except that E_{ESD} stands for the effect of ESD on the activation energy of desorption and is expressed in Eq. 3.8 as a function of beam energy and beam current .

$$E_{ESD} = function(i, E) \quad 3.8$$

The energy term estimated from the Arrhenius plot is actually E_{des}-E_{ESD}, which explains why the estimated activation energies in this work differ from the values in the literature review. Here for convenience the energy term E_{des}-E_{ESD} is call pseudo desorption energy.

It has been previously pointed out that secondary electrons are doing two jobs: removing the adsorbed molecules, which is unfavorable to the deposition, and dissociating the adsorbed molecules, which is favorable to the deposition. Therefore, there must be a competition between the desorption process and the dissociation process. This can explain the observation that the pseudo desorption energy decreased with beam current as shown in Figure 3.11 and that the pseudo desorption energy increased with beam energy as shown in Figure 3.12. Under a given beam energy, when the beam current was small the secondary electrons generated on the surface were limited and the influence of ESD was small compared with thermal desorption. As the beam current increased the influence of ESD became more dominant with increasing SE, which led to an increase of the term E_{ESD} and thus a decrease of the pseudo desorption energy. This gives an explanation why the pseudo desorption energy decreased with beam current as illustrated in Figure 3.11. Similarly under a given beam current when the beam energy was large the secondary electron yield was low and the number of secondary electrons was small. ESD had little effect on the pseudo desorption energy. But as the beam energy decreased the secondary electron yield was boosted and more secondary electrons were generated to provide energy for the adsorbed molecules to desorb from the surface. This made an increase of the term E_{ESD}, which explains the decrease of the pseudo desorption energy with the decreasing beam energy as illustrated in Figure 3.12. In general when the number of secondary electrons is low, which is the case of high beam energy and low

beam current, the thermal desorption is ruling and ESD has little influence on the pseudo desorption energy. As the secondary electrons increase to a high level, which is under a low beam energy and high beam current, ESD is more dominant and leads to a decrease of the pseudo desorption energy.

For the experiment under varying beam currents and a fixed beam energy the influence of the substrate temperature on the base width and height of deposit was investigated as shown in Figures 3.13 and 3.14 respectively. Figures 3.13 and 3.14 show that as the substrate temperature decreases two types of growth behavior occur. At a high beam current a lower substrate temperature resulted in an increase in base width, and the base width gained a larger increase when the substrate temperature dropped below 0°C. At the high beam current the height slowly increased as the substrate temperature fell and then started to decline when the temperature was below 0°C. An intermediate beam current followed a similar behavior. With respect to the low current, as the substrate temperature dropped, even down below 0°C, the base expanded but only to a small extent while the height increased with a decreasing substrate temperature over the whole range. The interpretation for the growth under high and intermediate beam currents could be put as follows. When electron beam irradiated the top of the deposit, a depletion zone was formed and the concentration gradient drove the adsorbed molecules to move from the bottom of the deposit to the depletion zone on the top. Meanwhile a number of the primary electrons traveled to the sidewall and produced secondary electrons on the sidewall surface. The adsorbed molecules that diffused along the sidewall were decomposed by these secondary electrons. The yield of the dissociation on the sidewall was determined by two factors. One is how many secondary electrons were emitted from the sidewall surface and the other is how many molecules were on the sidewall and how fast they could move. To study those factors, an understanding of interaction volume is necessary.

A Monte Carlo electron-trajectory simulation showed that for a given beam energy the size and shape of the electron-solid interaction volume stays constant with a varying beam current. Different beam currents only change the dose distribution

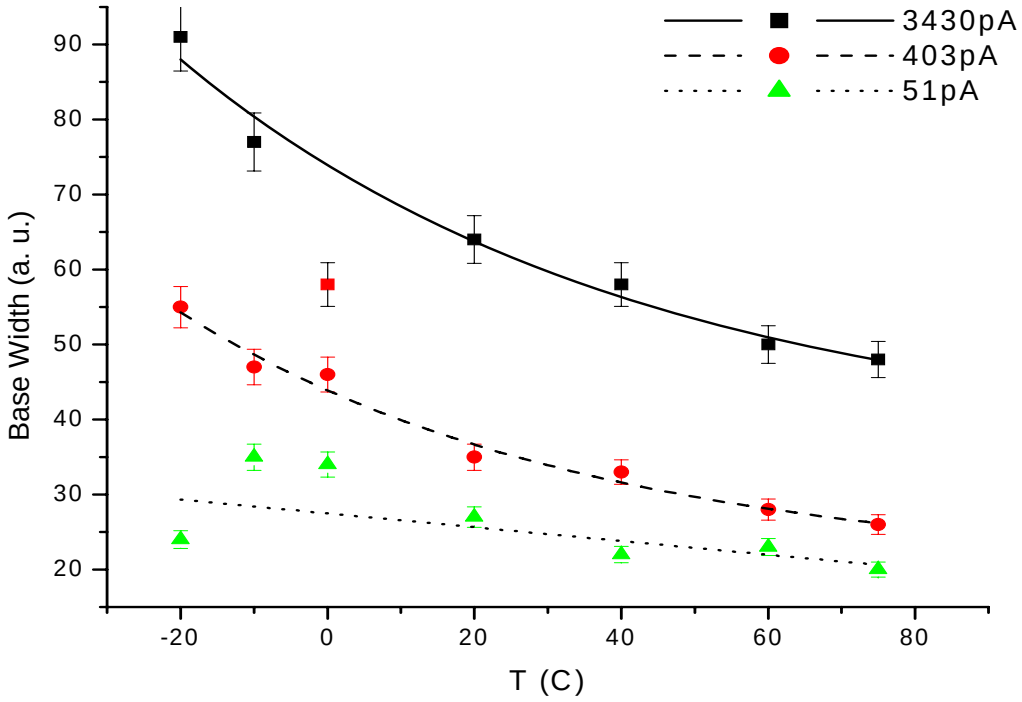

Figure 3.13 Temperature Depence of Base Width under Varying Beam Currents

A plot illustrates the variance of the base width of the deposits with the substrate temperature under varying beam currents (51, 403 and 3430pA) and 20keV.

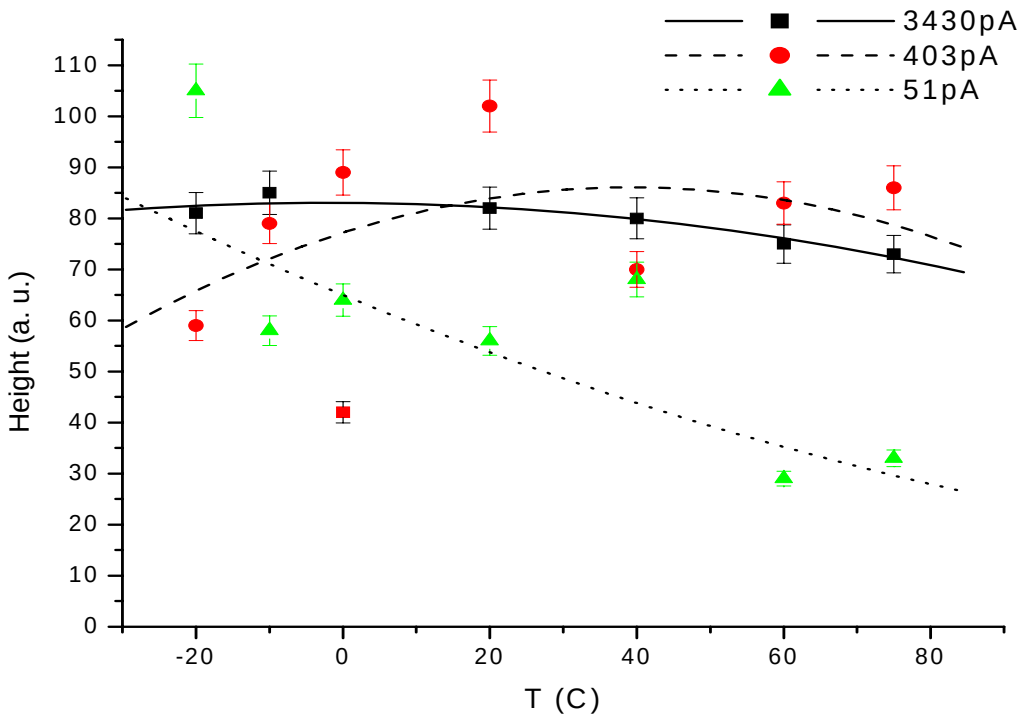

Figure 3.14 Temperature Dependence of Height under Varying Beam Currents

A plot illustrates the variance of the height of the deposits with the substrate temperature under varying beam currents (51, 403 and 3430pA) and 20keV.

inside the interaction volume. A concept of critical dose density is introduced here and defined as the minimum dose density of electrons that can generate enough secondary electrons to dissociate adsorbates and forms a visible deposit. In this experiment the contours of the critical dose density for both high and intermediate beam currents were far larger than the size of the deposits so there were a large amount of secondary electrons emitted from the surface and the flux of diffusing molecules on the sidewall was comparably insufficient. Under this condition, the deposition occurring on the sidewall was surface diffusion controlled. At room temperature and above a drop of substrate temperature resulted in more adsorbed molecules diffusing on the sidewall and the diffusion rate decreased but was still enough to drive an increasing number of molecules to reach the top with the decreasing substrate temperature. Thus the number of precursor molecules decomposed on the sidewall as well as on the top increased with the decreasing substrate temperature. This explains the increase of both height and base width of the deposits with a decrease in substrate temperature down to the room temperature. As the substrate temperature continued to fall, even below 0°C, the surface diffusion of adsorbed molecules was decelerated so much that the portion of the diffusing molecules, which decomposed on the side wall, was increasing significantly and the portion, which could reach the top, started to decline. This explains why the base width upsurged while the growth of the height lost momentum and started to decline as the substrate temperature continued to drop to below 0°C. Under a low beam current the contour of the critical dose density, however, was much slimmer and comparable to the size of the deposits. Far less primary electrons could travel to the sidewall surface and generate secondary electrons there. The number of secondary electrons was insufficient compared to the amount of molecules on the sidewall. Under this condition the deposition process occurring on the sidewall was secondary electrons controlled. As the substrate temperature fell through the whole experimental range, the portion of molecules, which got to the top without decomposition, kept growing because not enough secondary electrons were supplied on the sidewall for decomposition even though molecules on the surface became moving much slower under the freezing point. The portion, which decomposed on the sidewall, increased as well but at a much lower rate since few

secondary electrons were available for dissociation. This explains why throughout the whole experimental range both the height and base width grew with a decreasing substrate temperature.

For the experiment under varying beam energies and a fixed beam current the influence of the substrate temperature on the base width and height of deposit was also investigated as shown in Figures 3.15 and 3.16 respectively. These two figures illustrate a similar trend of growth behavior as shown in Figures 3.13 and 3.14 under the intermediate beam current.

In this work we did not observe anything similar to the etching of the substrate described by Matsui et al.[22] when the substrate was heated up to 75°C and irradiated by electron beam. However, when the electron beam was turned off and the substrate was exposed to WF_6 for hours at 75°C, there was a small etched region on the substrate. This could be explained by ESD theory as well. When the electron beam was turned off, the dissociation of adsorbed WF_6 molecules occurs even below room temperature[127, 129], forming F radicals which etch away the substrate. However, when electron beam is turned on, the F radicals rapidly desorb from the surface because of ESD[128] and no etching occurs to the substrate.

3.4.1.5 Conclusion

In summary, we have shown that the dissociation occurs on the surface instead of in the gas phase and the temperature dependence of the growth rate follows an Arrehnius relationship. Electron stimulated desorption has been found to have an important influence when there were a large number of SE emitted on the surface. Electron scattering in the tip and surface diffusion are involved in the process and determine the feature size of the deposits.

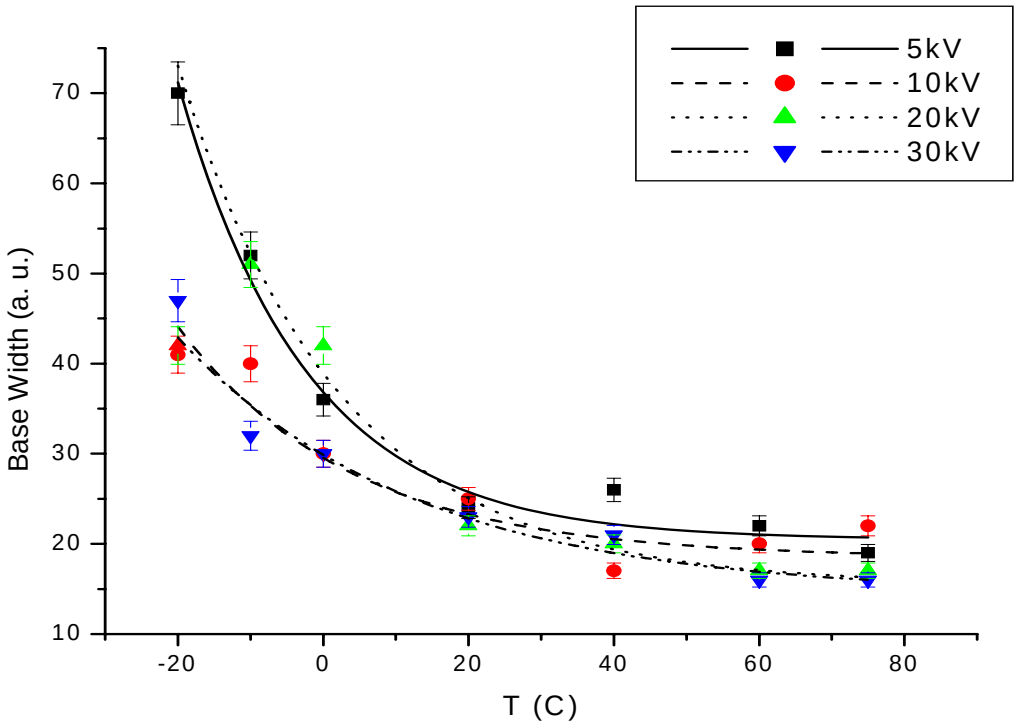

Figure 3.15 Temperature Dependence of Base Width under Varying Beam Energies

A plot illustrates the variance of the base width of the deposits with the substrate temperature under varying beam energies (5, 10, 20 and 30keV) and 140pA.

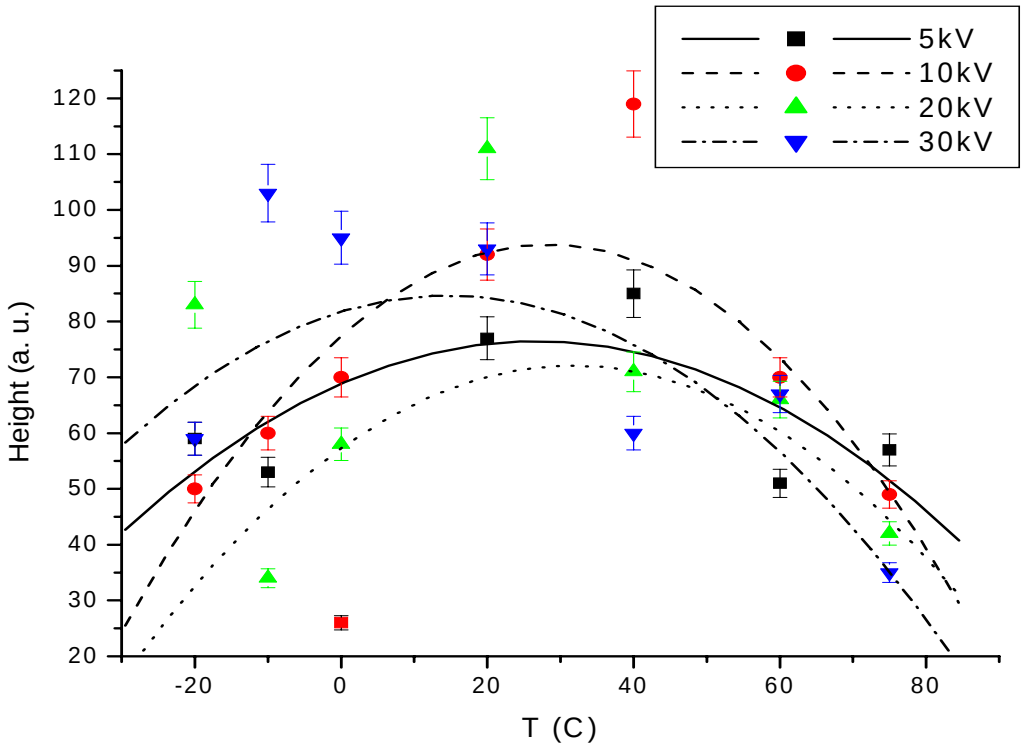

Figure 3.16 Temperature Dependence of Height under Varying Beam Energies

A plot illustrates the variance of the height of the deposits with the substrate temperature under varying beam energies (5, 10, 20 and 30keV) and 140pA.

3.4.2 Verification of assumption 2

3.4.2.1 Introduction

In Section 3.3, it has been mentioned that SE are generally believed to be the only particles to dissociate the precursor gases. Most of the models proposed so far are using SE to explain the growth of the deposited structures and it works on most situations. However, the broadening effect was observed in the deposited structures, indicating BSE have the capability to dissociate the precursor gases as well. Besides, the possibility that PE take part in dissociation of precursor gases has not been ruled out even though the high energies (~keV) of primary electrons, which associate with small cross-sections for dissociation, make that possibility quite obscure. One argument is that primary electrons have such a large number that the low cross-section for dissociation can be offset.

3.4.2.2 Bias experiment

3.4.2.2.1 Experimental set-up

The experimental work to be discussed in this section was focused on the influence of eliminating secondary electrons on the growth of the deposits. If secondary electrons, as generally believed, are the only particles for decomposition of precursor gases, suppressing secondary electrons should result in no deposition at all. Even if secondary electrons are not the only particles, but still the main participants for dissociation, eliminating secondary electrons should result in a significant decrease of the growth.

An HP 712C power supply was employed in this work to give a positive bias to the substrate so that secondary electrons emitted from the substrate surface would be reduced or eliminated. The power supply can provide a bias with range of –200 V to +600 V, and was plugged to the grounding port of the SEM, which is electrically connected to the sample stage inside the specimen chamber. A 1 mm tungsten foil was

chosen as the substrate because of its good conductivity. The surface of the tungsten foil was polished to a very fine scale to achieve a microscopically flat surface.

Twelve biases, 0, +50, +75, +100, +125, +150, +175, +200, +225, +250, +275 and +300 V, were chosen to compare the growth of the deposition at various biases. For each bias, the electron beam was focused on the tungsten substrate in spot scanning mode for 1 min. The growth condition (working distance, beam energy, beam current, chamber pressure and magnification) was kept the same throughout the experiment. The detail of the experimental condition was as follows: working distance 6 mm, beam energy 20 keV, beam current 73 pA (measured with a Faraday cup through the grounding port of the SEM), chamber pressure $3.0\times10^{-3} \sim 4.0\times10^{-3}$ Pa. The deposition was carried out at the magnification of ×50,000. It has been estimated that the local pressure at the electron-irradiated area is on the magnitude of 100 times greater that the chamber pressure as calculated by capillary flow equations[133]. Details of the EBID system set-up can be found in Chapter 2.

3.4.2.2.2 Results and discussions

The nano-rods grown on the tungsten substrate at different sample biases are illustrated in Figure 3.17. For the deposits grown at +50 and +75 V, the heights were shorter than the height of the nano-rod deposited at no bias. The possible explanation is that the local gas flux was not steady state throughout the experiment, which was reflected on the observation of periodic drop of the chamber pressure. Other than that, there was no significant difference between the heights of the nano-rod grown at no bias and those grown at positive biases. This result seems to indicate that the role of secondary electrons in EBID may not be as important as we expected since no deposition or a significant decrease of growth should have occurred if the SE is suppressed by a positive sample bias over +50V.

At first glance this argument sounds plausible. However, when the polarity of the detectors within the chamber is taken into consideration, this argument is challenged. As

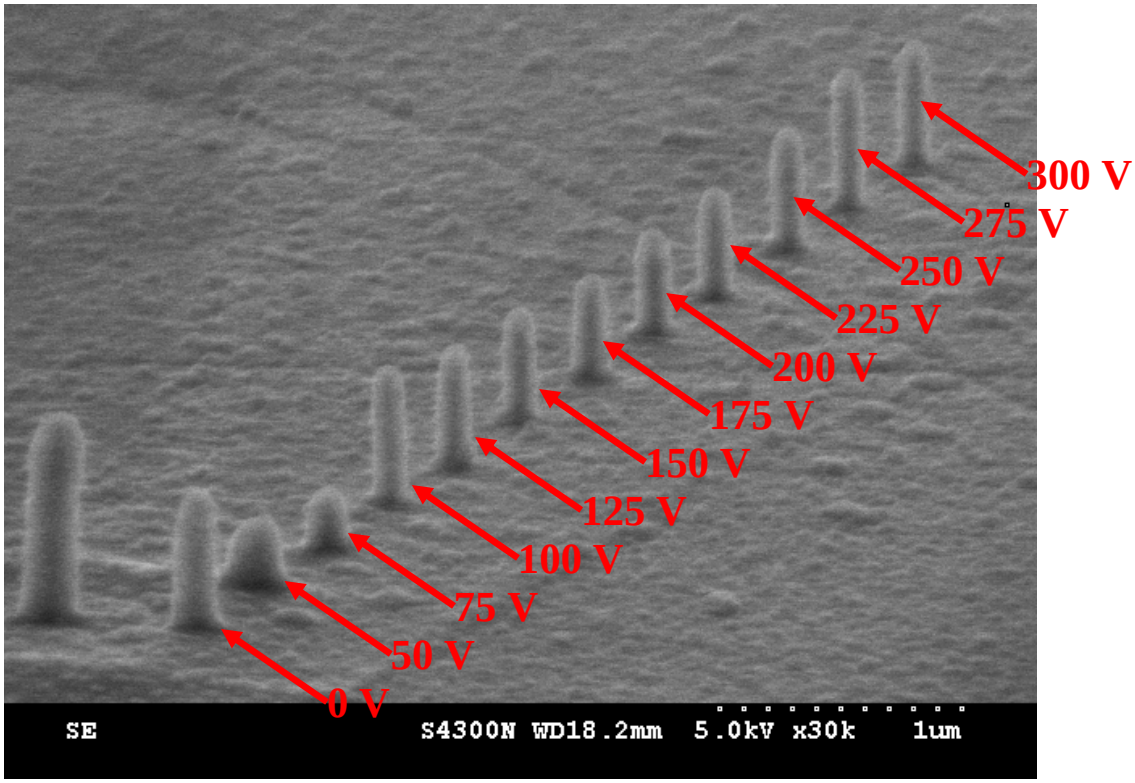

Figure 3.17 Effect of Sample Bias on Growth Rate

An electron micrograph of the nano-rods grown on a tungsten substrate at the twelve different sample biases, 0, +50, +75, +100, +125, +150, +175, +200, +225, +250, +275 and +300 V.

described earlier in Chapter 2, when the E-T detector is in SE mode, the Faraday cage is positively biased at +250 V so that secondary electrons can be efficiently collected. During deposition the detector was always turned on and in SE mode, and this positively-biased Faraday cage might generate an electric field whose field lines point out from the sample surface, as intuitively speculated. This electric field pulls secondary electrons out of the sample surface and the deposition occurs.

To verify this proposal, an attempt was made to introduce a negative bias to the Faraday cage, which, intuitively, should reverse the direction of the induced field lines to point into the sample surface and keep secondary electrons from coming out of the surface. This attempt led to an extended experiment for the Bias Experiment, which will be introduced next. Furthermore, an electron ray tracing simulation, by SIMION 3D^{TM} ion and electron optics simulator, would be introduced later on to reveal what the electron trajectories would look like in the chamber.

3.4.2.2.3 Extended experiment

In this section the influence of the polarity of the Faraday cage on the deposition and the electric field distribution within the chamber was investigated. The experiment focused on how the electric polarity of the Faraday cage affects the field distribution in the chamber and the deposition as a consequence.

The experimental procedure was the same as the Bias Experiment. The difference was that deposits were made at a set of selected sample biases under the conditions of a positively-biased Faraday cage and a negatively-biased Faraday cage respectively. Switching the electric polarity of the Faraday cage was achieved by selecting "SE" as "signal setup" to get the positive bias and "BSE" to get the negative bias. For the both conditions, a set of sample biases, 0, +50, +100, +150 and +200 V, were selected. The detail of the experimental condition was as follows: deposition time 90 sec, working distance 4 mm, beam energy 30 keV, and chamber pressure $7.0\times10^{-3} \sim 8.0\times10^{-3}$ Pa. The deposition was carried out at the magnification of ×50,000.

The resultant deposits are shown in Figure 3.18. It can be seen that switching the electric polarity of the Faraday cage had no significant effect on the deposition. The deposition can happen on an unbiased surface or a biased surface no matter the Faraday cage is positively or negatively biased. There are only two explanations for this observation. One is that the design of the experiment did not work. No matter how much the sample surface was positively biased and no matter the Faraday cage was positively or negatively biased, secondary electrons were not held back within the surface. They came out of the surface and made the dissociation happen. The other explanation is that secondary electrons are not the major element for dissociation and suppressing secondary electrons does not change deposition significantly. This explanation will lead to the experiments designed for verifying the role of the primary electrons and backscattered electrons, which will be discussed later. At this moment, we need to check the reliability of the Bias Experiment.

A further study of the influence of the sample bias on the work function of the sample material and the field distribution inside the chamber revealed the physics underneath. During our experiment it was seen that that the collected secondary electron signals dropped and the images faded away as a positive bias was applied to a conductive sample. This observation led to the misunderstanding that the positive sample bias could hold secondary electrons from coming out of the surface, which was the base for the Bias Experiment. The truth is that the sample bias cannot prevent secondary electrons from emitting from the surface.

First, the work function of the sample material is not changed with the bias given to the sample. The work function is the minimum energy needed to remove an electron from the Fermi level in a metal to a point at infinite distance away outside the surface. The work function is generally about half the ionization energy of a free atom of the metal and the ionization energy is determined by the atomic structure. Therefore the work function of tungsten, which is about 4.5 eV, keeps constant despite of the given bias. When generated within the escaping distance below the surface, the SE were not feeling difference because of the bias. They traveled to the surface and cross the solid-vacuum

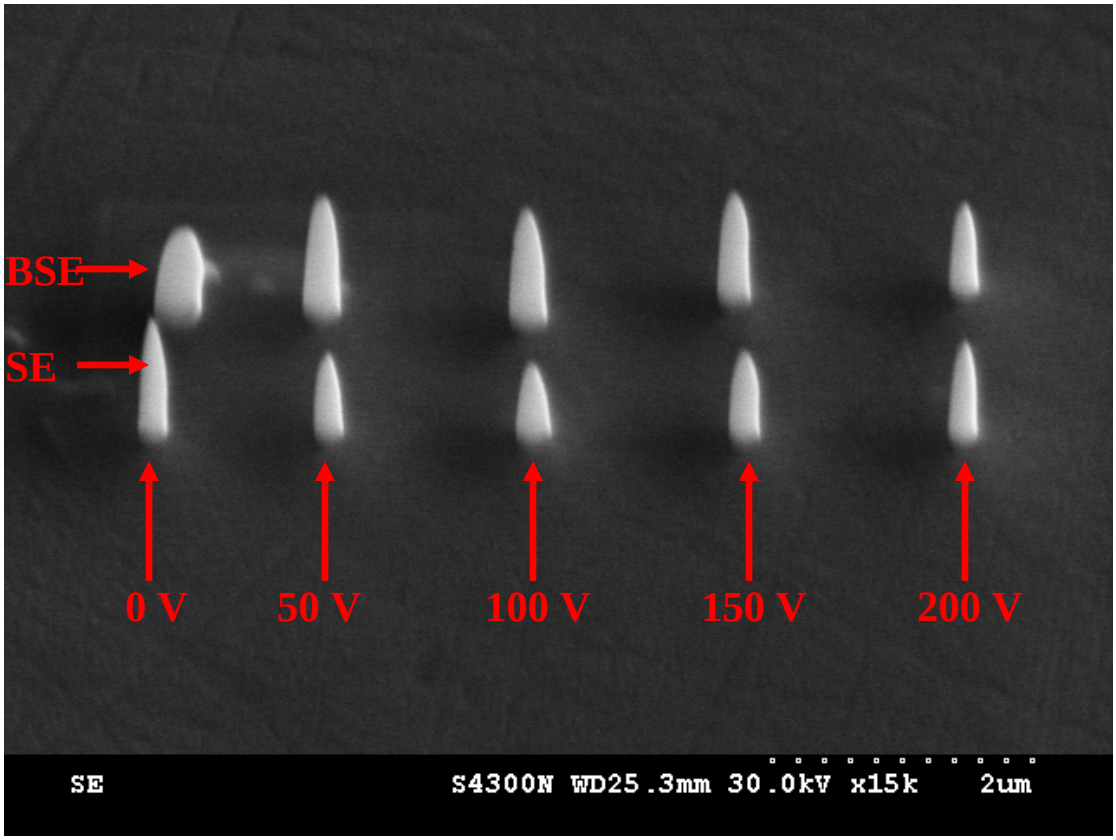

Figure 3.18 Comparison of Sample Bias Effect between SE and BSE Mode

An electron micrograph of the nano-rods deposited under the condition of a positively-biased Faraday cage and a negatively-biased Faraday cage. The selected sample biases were 0, +50, +100, +150 and +200 V.

interface by overcoming the same potential barrier, i.e. work function. This suggests that the number of SE emitted from the surface does not change whether the sample is positively biased or not.

Second, the electric field inside the chamber may not be able to prevent those SE at the surface from going through the adsorbate layer and breaking the bonding of the molecules. SIMION 3D^{TM}, an ion and electron optics simulator, was employed to mimic the trajectories of the secondary electrons by changing the biases on the sample and Faraday cage. A geometry file was written to define the major electrodes, which include a grounded chamber, a sample stage with a substrate mounted, a biased detector and a ground needle for gas injection. The script for the geometry file is shown in Appendix A. The cross section of the system is shown in Figure 3.19(a). Eight electrons were set for ray-tracing simulation and their kinetic energies were set as 5, 10, 15, 20, 25, 30, 35 and 40 eV, which are within secondary electron energy range. The systems working in SE and BSE mode are illustrated in Figures 3.19(b) and 3.19(c) respectively, which suggest a good approximation for the realistic geometric configuration since SE are all collected by the detector under SE mode and all repelled from the detector under BSE mode.

The flying trajectories of SE under SE mode are illustrated in Figure 3.20(a)-(d). It can be seen that all SE are all flying toward the detector when the sample is not biased. When the sample is positively biased, part of the SE are pumped up from the surface and then pulled back into the sample or stage. As the bias increases, this portion of SE increases and the portion of SE which reach the detector decreases, which agrees with the observation that the brightness of the SE image decreased with the positive sample bias. The simulation shows that no matter eventually the SE were collected by the detector or pulled back to the sample or stage they are all able to pass through the adsorbate layer on the surface and the dissociation happens. Similarly the flying trajectories of SE under BSE mode were simulated and illustrated in Figure 3.21(a)-(d). The trajectories at zero sample bias show that the SE travel straightly toward the column instead of being deflected toward the detector. When the sample is positively biased, all the SE are pumped up from the surface and then pulled back into the sample or stage. As the bias

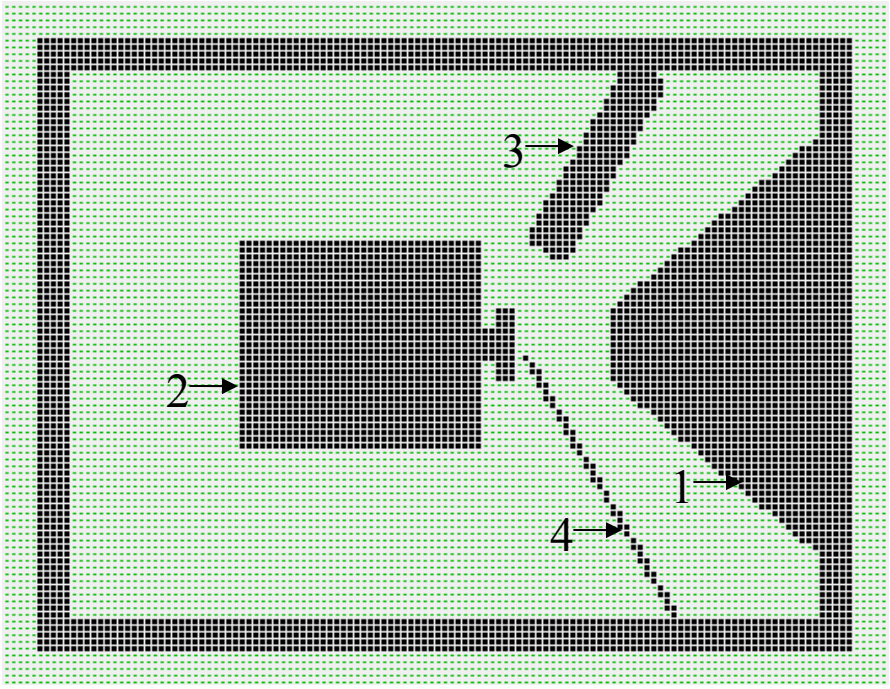

(a)

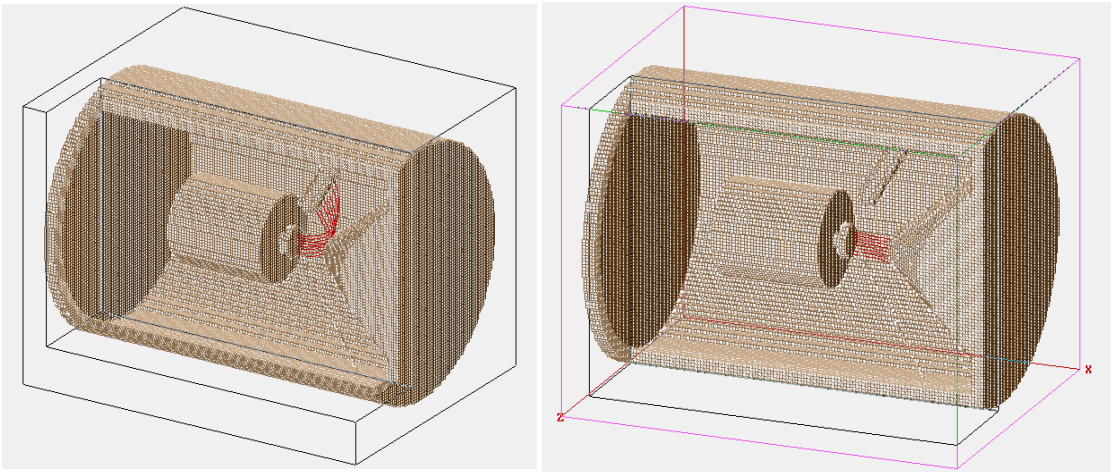

(b) (c)

Figure 3.19 Configuration for Electron Ray Tracing

Images generated in SIMION 3D™ present (a) a cross section of the system which consists of (1) a grounded chamber, (2) a sample stage with a substrate mounted on, (3) a detector and (4) a ground needle for gas injection; (b) a cut-away view of the system in SE mode; and (c) a cut-away view of the system in BSE mode.

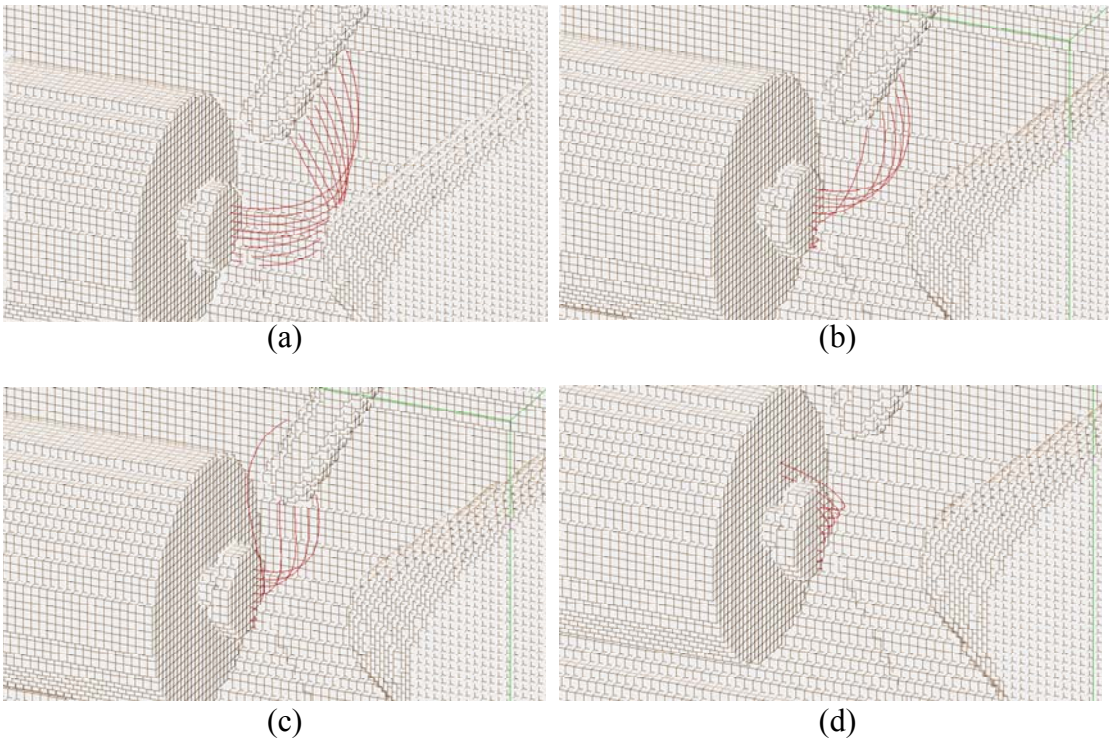

Figure 3.20 Electron Ray Tracing Simulation of SE in SE Mode

A series of images present the electron ray tracing of SE by SIMION 3D^{TM} in the case of the detector in SE mode (+250V) and the sample biased at (a) 0V, (b) 50V, (c) 100V and (d) 200V.

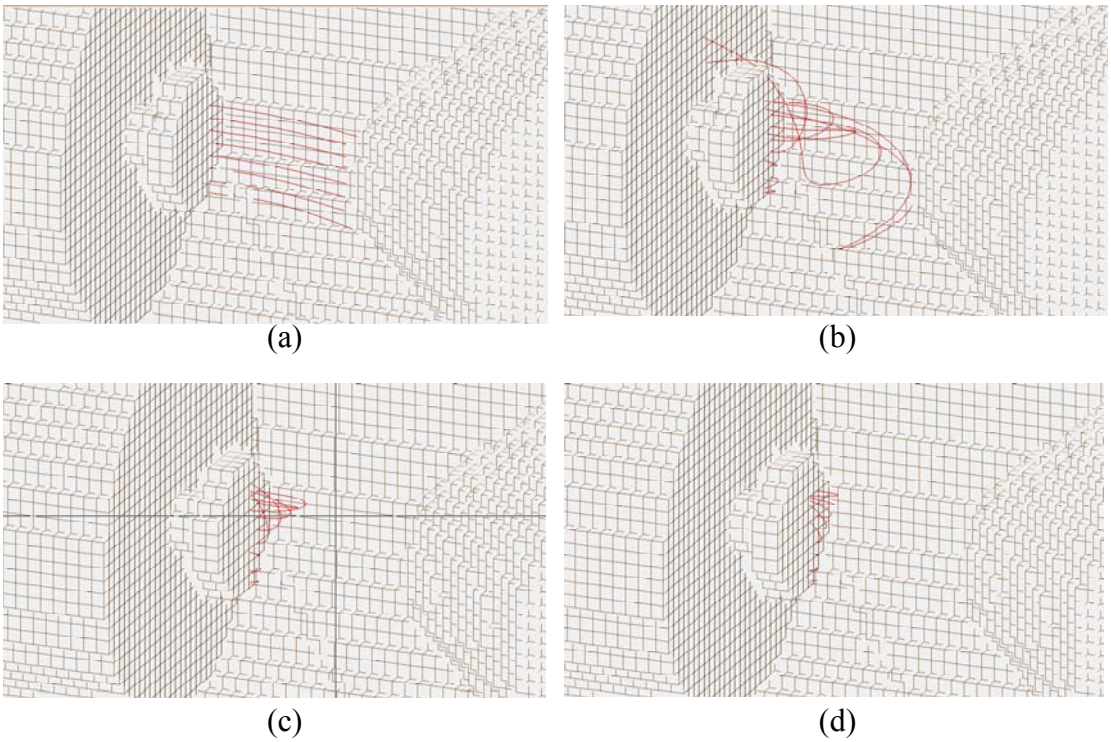

Figure 3.21 Electron Ray Tracing Simulation of SE in BSE Mode

A series of images present electron ray tracing of SE by SIMION 3D^{TM} in the case of the detector in BSE mode (-50V) and the sample biased at (a) 0V, (b) 50V, (c) 100V and (d) 200V.

increases, the distance which the SE can travel away from the surface is shortened, but they can still interact with and decompose the molecules in the adsorbate layer. Therefore as illustrated by the simulation the sample bias can not prevent the SE from interacting with the adsorbate layer and the dissociate happens no matter whether the sample is biased, no matter how much the sample is biased or no matter the detector is in SE mode or BSE mode.

In conclusion, it is proven that because of its intrinsic flaw this Bias Experiment could not achieve its purpose as it was supposed to be. A new approach needs to be taken to verify the role of secondary electrons in EBID.

3.4.2.3 The SE-Yield experiment

3.4.2.3.1 Introduction

Since it is not practical to suppress secondary electrons from the surface, other methods have to be sought to verify the correlation between the deposition and the number of secondary electrons. Changing SE yield of substrates would be promising because the factors on which SE yield dependent are already well known. In this experiment we will find out whether the growth of deposits changes with SE yield of substrates and how they are correlated if the growth is influenced by the SE yield.

As stated earlier, there are three major factors determining SE yield. These factors are specimen composition, beam energy and specimen tilt. Without *in situ* surface cleaning the compositional dependence might not be strong. But at low beam energies the influence of chemical composition on SE yield is prominent even when the surface is not clean. With respect to the beam energy dependence, SE yield increases with beam energy starting from threshold energy until it gets to the peak and then falls back. While the specimen tilt dependence is well described by a secant function.

An experiment was designed to find out the correlation between EBID growth rate and SE yield of substrates.

3.4.2.3.2 Experimental setup

The work to be discussed in this section was focused on the influence of varying the SE yield on the growth rate. If SE are the only particles or the major particles responsible for the dissociation, a significant change of the number of secondary electrons should lead to a significant change of growth rate. Three factors, material type, beam energy and sample tilt, were selected to control the yield of secondary electrons. For each factor, two levels were selected for comparison. In this experiment, silicon and tungsten, 5 kV and 20 kV, 0° and 60°, were chosen for the two levels for material type, beam energy and sample tilt respectively. The material type and beam energy were selected in this way because the SE yield of these two materials under these beam energies are so different that a good comparison would be illustrated if the growth rate is correlated with the secondary electron yield. The yields of silicon and tungsten at 5 and 20 kV obtained from the literature were shown in Table 3.1. For the same material and beam energy, a 60°-tilted surface has twice the yield than the non-tilt surface as indicated by the secant relation.

The silicon and tungsten substrates in this work came from a standard (100) silicon wafer and an Alfa Aesar tungsten foil with purity of 99.95%. The tungsten substrate was chemical-mechanically polished to obtain microscopic flatness. During deposition, the chamber pressure was controlled at ~ 5.1×10^{-3} Pa, and the working distance was set between 0.8 to 1.5 mm. The beam currents under 5 and 20 kV were calibrated to ~54.7 pA. The electron beam was focused on the substrates in a spot scan mode. The experiment included two blocks. In the first block all the substrates were not tilted. Deposition was made under the two beam energies on each substrate. Under each beam energy the deposits were grown for 1, 2 and 3 minutes respectively. In the secondary block all the substrates were at a tilt angle of 60° with the electron beam by the aid of a wedge. The procedure was the same as the first block, which explored all the combinations of material types and beam energies. Under each combination, three runs were carried out for 1, 2 and 3 minutes respectively.

Table 3.1 Yield of Secondary Electron of Silicon and Tungsten at 5 kV and 20kV

	5 kV	20 kV
W	0.8	0.4
Si	0.24	0.1

* Courtesy of Yinghong Lin

3.4.2.3.3 Results and discussions

Figures 3.22 and 3.23 demonstrate the SEM images of the nano-rods deposited in a non-tilted position and tilted position respectively. All the deposits were taken images at a tilt angle of 45° from the upright position of the nano-rods and the height and width of each was measured. The deposited volume was then calculated based on the height and width of each deposit. The deposited volumes for 1, 2 and 3 minutes under each condition were plotted and the growth rate was then calculated. The normalized growth rate for each condition was listed in Table 3.2. From the table we can see the growth rate is changing with material types, beam energies and sample tilt angles. However, the influences of these three factors on the growth rate shown in Table 3.2 do not match the predicted correlation with those on the secondary electron yield illustrated in Table 3.1. When the substrates were not tilted, for both tungsten and silicon the growth rate at 5 keV was almost double of that at 20 keV though the high yield of secondary electrons from the tungsten substrate was not reflected in the growth rate. For the tilted substrates, there was no correlation between the growth rate of the deposition and the secondary electron yield with respect to the material type or beam energy. Comparing the cases of the tilted substrates and non-tilted substrates, we can see that the growth rates for the tilted substrates were generally larger than the non-tilted substrates except the deposition on the tungsten substrate at 5 keV. Though the growth rate ratios of the tilted substrates to the non-tilted substrates were not a factor of 2 as we expected.

To explain this observation, we have to understand an important fact that in EBID the material with which electrons interacted was not always the substrate. As the deposition went on, the interaction gradually transited from between electrons and the substrate material to between electrons and the deposited material. This indicates that only at the very beginning of the deposition the secondary electron yield was solely determined by the substrate material. Once when it started to form a thin layer of deposited material (less than escape distance of SE) on the substrate surface, both the substrate material and the deposited material made contributions to the secondary electron yield since the dimension of this thin layer of deposited material is comparable

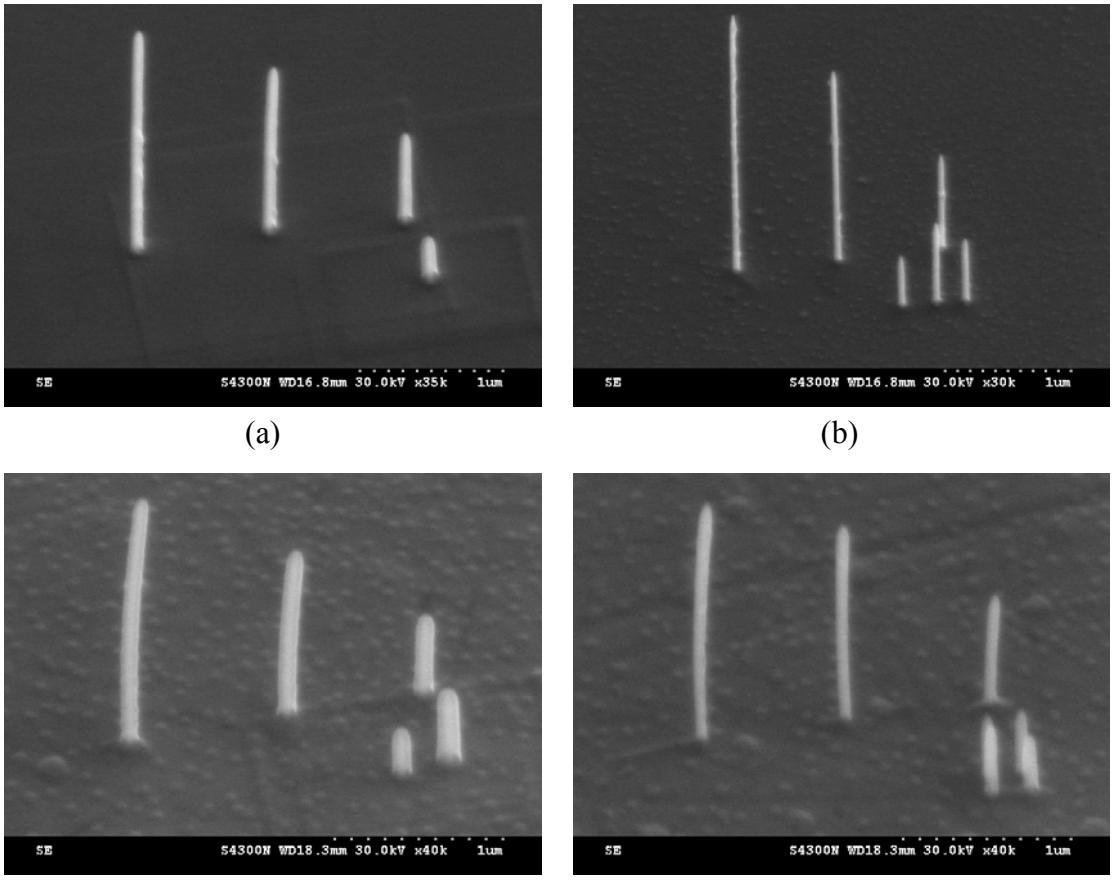

(a) (b)

(c) (d)

Figure 3.22 Growth Variance with Beam Energy and Sample Material for a Flat Surface

A series of electron micrographs show the nano-rods grown for 1, 2 and 3 minutes under the following conditions: (a) 5 kV and Si substrate, (b) 20 kV and Si substrate, (c) 5 kV and W substrate, and (d) 20 kV and W substrate. The substrates were not tilted.

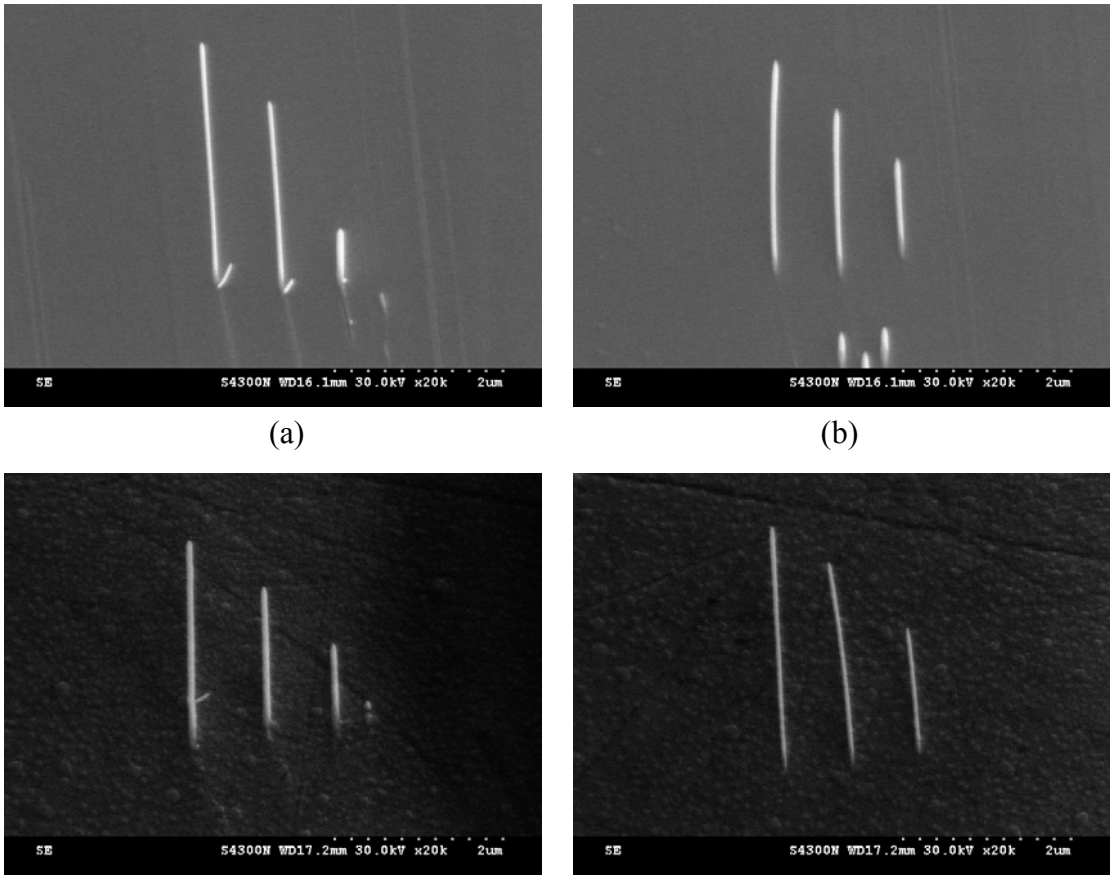

(a) (b)

(c) (d)

Figure 3.23 Growth Variance with Beam Energy and Sample Material for a Tilted Surface

A series of electron micrographs show the nano-rods grown for 1, 2 and 3 minutes under the following conditions: (a) 5 kV and Si substrate, (b) 20 kV and Si substrate, (c) 5 kV and W substrate, and (d) 20 kV and W substrate. The substrates were tilted for 60°.

Table 3.2 Normalized Growth Rate of Deposits Grown under Various Combination of Material, Beam Energie and Sample Tilt

0° degree tilt		5 kV	20 kV
	W	1	0.359
	Si	0.629	0.306
60° degree tilt		5 kV	20 kV
	W	0.592	0.563
	Si	0.734	0.559

to the escape distance of SE. As the deposition continued, more portion of the interaction volume moved into the deposited material and the secondary electron yield continued to change. This change continued until eventually the whole interaction volume entered the deposited material and the secondary electron yield was then contributed only from the deposited material. Thus this explanation suggests the growth rates of the deposition we obtained in this experiment were the results from both the substrate materials and deposited material.

Since now we understand the transition from the electron-substrate interaction to the electron-deposit interaction, we can explain why the correlation between the growth rate and the SE yield was not as we predicted. First, as to the group of the non-tilted substrates, we saw that the growth rates on the tungsten substrate were only slightly larger than those on the silicon substrate instead of by a factor of 4. This is because once the tungsten deposit formed on the silicon substrate the secondary electron yield was boosted and kept increasing until the interaction volume completely moved into the deposited material. This boost of secondary electron yield drove the deposit to grow at a higher rate. However, the correlation between the growth rate and the secondary electron yield with respect to the beam energy was strong. This makes sense since both tungsten and silicon have a secondary electron yield twice as high at 5 keV as at 20 keV. No matter the solid interacting with the electrons is a silicon substrate with a tungsten deposit or a tungsten substrate with a tungsten deposit, it will give an overall secondary electron yield twice as large at 5 keV. This factor of 2 in the secondary electron yield was reflected on the growth rate. Second, as to the tilted substrates, the correlation between the growth rate and SE yield with respect to the material types and beam energies were both very weak and it seems like that the growth rate is independent of both material type and beam energy. At this point we have no plausible explanation for this and a better understanding of the physics behind this is needed to interpret this result.

Before we make a conclusion for this SE-yield experiment, we need to verify that the secondary electron yields of the substrate materials in this experiment is the same or close to those obtained from the literature since many factors such as purity and crystal

orientation can affect the secondary electron yield. A simple experiment was conducted for this purpose in the following steps:

Step (1) a Faraday cup was used to collect the beam current I_b;

Step (2) the substrate was irradiated by the same electron beam as in Step (1) and a sample current I_{sc1}, which is $I_b \cdot (1-\delta-\eta)$, was collected;

Step (3) a positive bias of +50 V was given to the substrate while it was irradiated by the same electron beam as in Step (1) and a second sample current I_{sc2}, which is $I_b \cdot (1-\eta)$, was collected. Then the secondary electron yield δ can be calculated by the expression

$$\delta = \frac{I_{sc2} - I_{sc1}}{I_b} \tag{3.9}$$

The yield measurement of both the tungsten foil and the silicon wafer at 5 and 20 keV confirmed that the secondary electron yields of the substrates in this experiment were generally the same as the literature.

The discussion in this section indicates that the interaction transits from between the electrons and the substrate material to between the electrons and the deposited material and the interaction volume moves from the substrate material into the deposited material, which is interesting. Based on that indication, a proposal was brought out that the diameter of the deposited structure might be dependent on the size of the interaction volume passing through the main body of the deposit. This proposal suggests that the observation in the Section 3.4.1 that a large beam current led to a structure with only a conical body and a small beam current led to a structure with a cylindrical body and a conical top might be fallacious. Since after the interaction volume completely moves into the deposited material it is expected not to vary with the distance it passes through and thus the deposited structure should have a uniform diameter everywhere except the

conical top. In another word, no matter what the beam current is, the deposited structure should have a cylindrical main body and a conical top given enough time to grow. To verify this proposal, an experiment would be carried out to examine the shape of the deposited structures grown at various beam currents for enough time. In addition, the sample current would be monitored to provide information about how electrons interact with the deposited material.

3.4.2.3.4 Extended experiment I and discussion

In this section an experiment would be conducted to study the shape of the deposited structures at different beam currents. The result will be used to verify whether all the deposited structures have both a cylindrical main body and a conical top no matter what the beam current is and this can help us understand the physics of electrons interacting with the deposited material. The sample current would be monitored to provide information of SE and BSE emission and information of growth. Time-resolved measurements of sample current for EBID was previously performed by Bret et al.[134-136] to investigate *in situ* control of EBID process. He reported that during EBID the sample current experienced a continuous decay until a plateau was reached and this current loss resulted from emission of SE and BSE, which depends on the diameter, composition and density of the deposits. Wang et al. [103] plotted correlation between the sample current change and the thickness of the deposited film and used the plot as a calibration to measure the film thickness by monitoring the sample current change.

The deposition was carried out on a germanium substrate. The beam energy was 20 kV and the chamber pressure was 5.5×10^{-3} Pa. Two beam currents, 50 and 2922 pA, were used since previously in both our work and the experiment results from the other group[17] expected that the first beam current would lead to a structure with a cylindrical main body and a conical top while the second beam current would give a structure with only a conical body. Under the beam current of 50 pA the deposition was made for 30, 60, 90, 120, 150, 210 and 600 s. Under the beam current of 2922 pA the deposition was made for 120, 150, 180, 210, 240, 270, 300, 360 and 600 s. During EBID process time-resolved

sample currents was collected for both beam currents by a Keithley 6485 Digital Picoammeter through the grounding port of the SEM and was plotted by ExceLINX software on a computer afterwards. During the measurement the picoammeter read the sample current every 0.3 s for 600 s. After the experiment all the deposits were taken images by being tilted for 45°. The results were shown in Figures 3.24 and 3.25 respectively.

The deposits grown for 600 s at 50 and 2922 pA confirm that eventually the deposits grew into a structure with a cylindrical main body and a conical top given a long enough growth time. As speculated previously, the interaction volume moves from the substrate material into the deposited material and once it leaves the substrate material the diameter of the deposit will be determined by the size of the interaction volume in the deposited material. The size of the interaction volume in the deposited material will not change with time and thus it leaves a uniform cylindrical shaft behind as it moves upward. Thus the deposited structure should always have a cylindrical shaft and a conical tip regardless of the beam current. Here the interaction volume is not the same definition as in the other books. Goldstein et al.[137] defined the interaction volume by the Bethe range, which is a function of beam energy, atomic number of the specimen, specimen thickness and specimen tilt. Since the beam energy in this experiment was the same for both beam currents the size of the interaction volume should be the same according to the definition of interaction volume, which could not yet explain why the diameter of the deposit under the higher beam current was larger. The interaction volume adopted above is actually a pear-shaped contour of the critical electron dose at a given beam energy as introduced in Section 3.4.1.4. For short we will call this contour of the critical electron dose the critical interaction volume and this concept will be frequently used in the coming-up discussions. This critical interaction volume expands with the beam current and the diameter of the critical interaction volume increases, which explains the observation that the diameter of deposit usually increases with beam current.

The measurement of the tip angle of the deposits under the two beam currents shows that the low beam current gave a sharp tip while a high beam current a blunt tip,

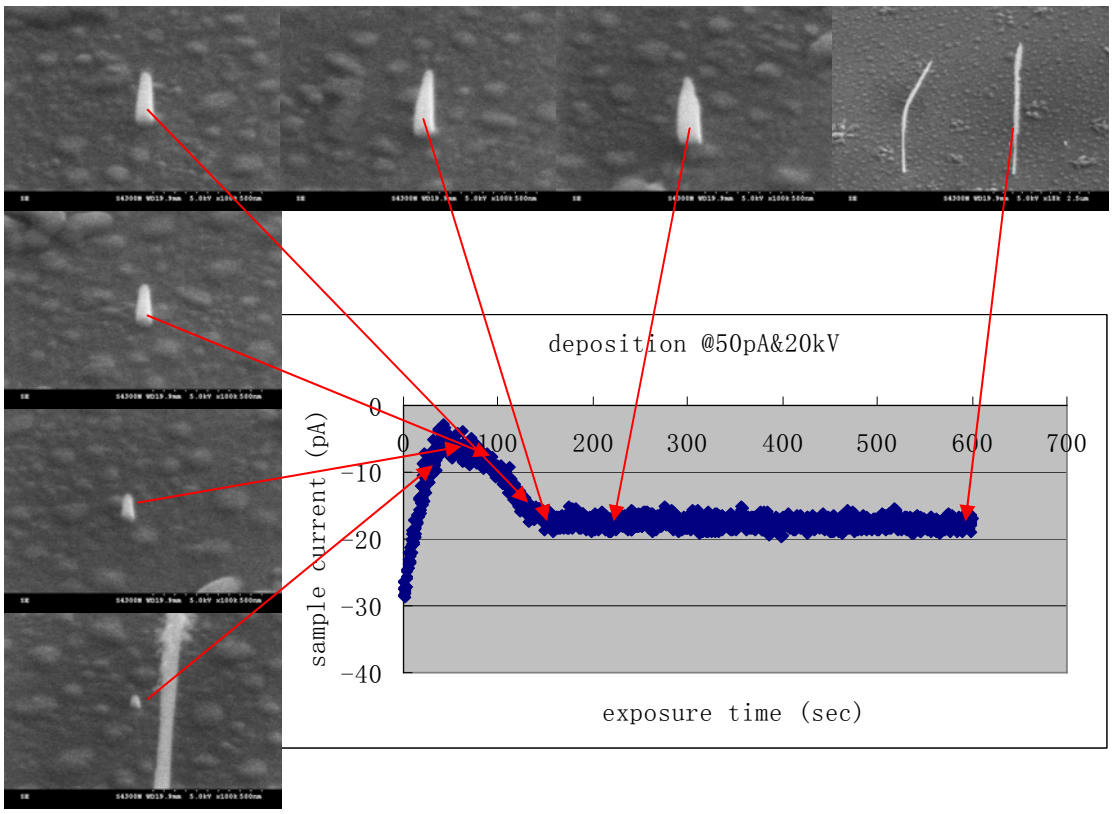

Figure 3.24 Sample Current Monitoring at 50pA

A plot of the time-resolved sample current during the deposition at the beam current of 50 pA and beam energy of 20 kV embedded with the SEM images showing the structures formed at different time phases.

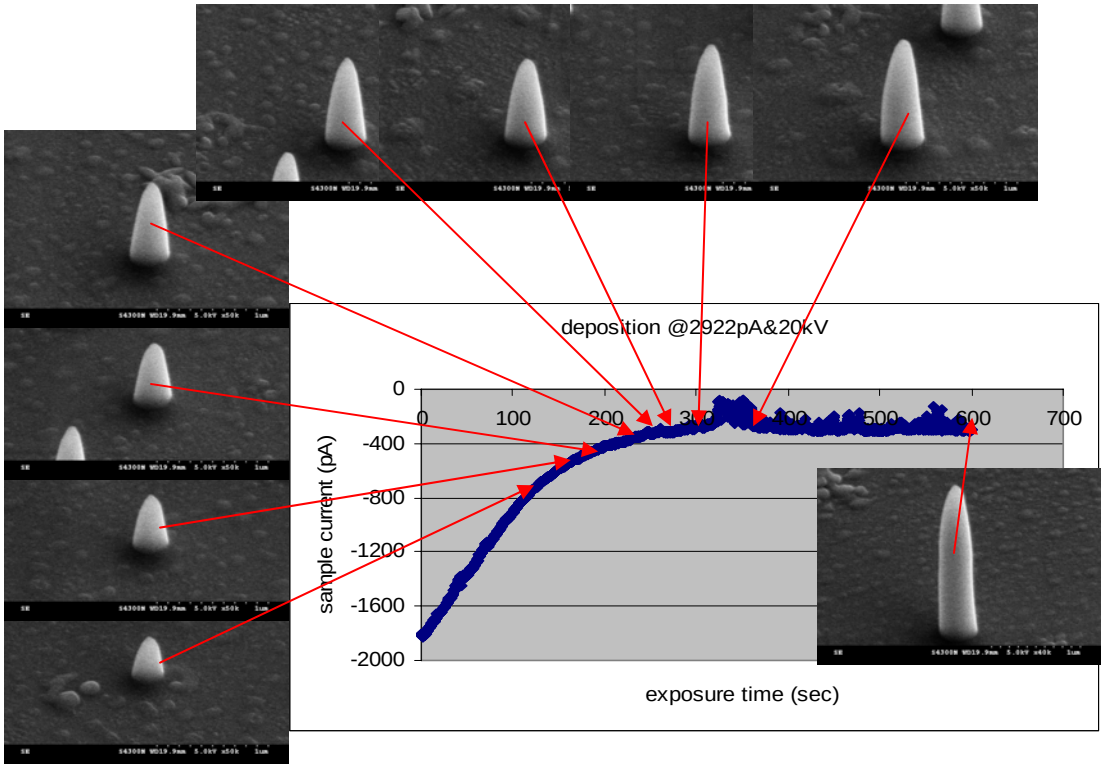

Figure 3.25 Sample Current Monitoring at 2922pA

A plot of the time-resolved sample current during the deposition at the beam current of 2922 pA and beam energy of 2922 pA embedded with the SEM images showing the structures formed at different time phases.

which is consistent with the observation from Schiffmann[17]. This is related to the critical interaction volume as well. As beam current increases, the electron density within the interaction volume increases and the contour of the critical electron dose expands. Therefore the solid angle of the neck of the pear-shaped critical interaction volume increased with the beam current and the tip angle of the deposits increased with the beam current. Similarly it can be expected that the tip angle should decrease with increasing beam energy since high-energetic PE are more likely to keep their original direction after being scattered. The critical interaction volume becomes longer and more acute as beam energy increases. This is supported by the observation in Figures 3.22 and 3.23. It can be seen from both pictures that 20 keV beam gave a sharper tip than 5 keV beam. This information is important because in field emission (FE) tip fabrication by EBID the sharpness of the tips is very critical. By lowering beam current and increasing beam energy a sharper FE tip can be obtained.

Another observation is that the tip angle kept constant throughout the entire deposition, even during the fast growth of the growth, which corresponds to the decay period of sample current. This suggests that the ratio of vertical growth rate to lateral growth rate kept constant during deposition. Assuming the gas supply and dissociation cross-section are the same all over the tip, information about electron flux distribution on tip can be deduced. In addition, a growth model named “Snow-cone Cup” model, illustrated in Figure 3.26, is proposed based on this observation. Conical top is selected in the illustration for simplicity. In this model a small bottom of the cup is laid upside down on the substrate, resembling the start of the deposition. Then a bigger bottom of the cup is laid upside down over the previous one, and the same procedure repeats until a full cup is laid upside down over a previous one. This full cup resembles the contour of critical interaction volume since now the base stops growing as not enough electron flux comes to the surface for dissociation. This is the fast growth stage, in which sample current drops rapidly to a plateau. Then the steady state growth, in which sample current keeps constant, begins, resembled by a new full cup being laid upside down over the previous full cup. The same procedure repeats and a cylindrical body is formed. This model is

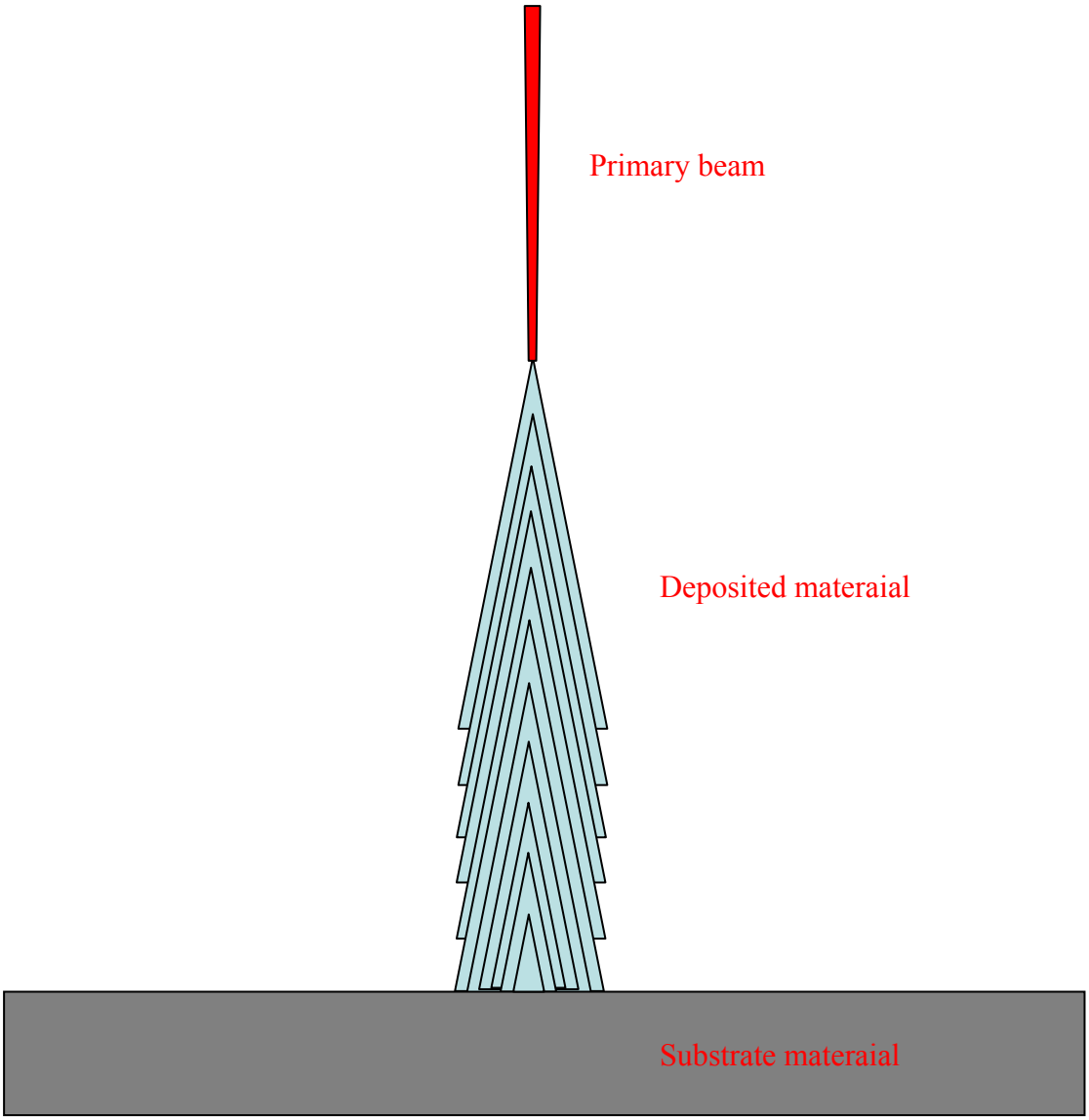

Figure 3.26 Snow-cone Cup Model

A schematic of the proposed "Snow-cone Cup" model for EBID growth which suggests that the deposit consists of layers and new layer always keep the geometry of the tip constant.

simple but crucial for simulation of EBID growth and may answer questions like how the structure affects the electrical property and composition.

In addition, we can predict that the nanofiber has uniform chemical composition along its length. The simulation by Weber et al.[51] indicated that the cone angle should increase with atomic number of tip material due to the increase of the characteristic angle for elastic scattering with the atomic number of the target. If the composition was not uniform along the length, the cone angle would vary along the length. This would be contradictory with the same cone angles illustrated by the inset micrographs in Figure 3.25. Another support comes from the unchanging sample current in the plateau stage. If the composition was not uniform during the deposition, the sample current would change with time because the varying composition would affect the emission of BSE and SE and then change the sample current.

Figures 3.24 and 3.25 are the plots of the time-resolved sample current with SEM images showing the deposits at different growth phase under two conditions of beam current. Both plots illustrate that the sample current decreased rapidly in the very beginning which corresponds to the growth of the conical tip and then the sample current reached a plateau stage once the cylindrical shaft appeared. Once again the critical interaction volume could be adopted to interpret this observation. From the plots the growth can be generally divided into two stages. In the first stage, the sample current drops rapidly as the conical tip grows. This is because in the very beginning the entry point of the primary electrons moves into the deposited material as the deposit starts to build up on the surface, which allows an increasing fraction of the incoming electrons to be able to escape from the sidewall of the deposit after few scatterings. In addition, these escaping electrons interact with tungsten in the tip and generate much more secondary electrons on the sidewall, which further contributes to the rapid decrease of the sample current. As secondary electrons generated on the surface of the tip drives the growth of the tip more fraction of the critical interaction volume moves upward into the deposited material, which in return allows more incoming electrons to escape and a continuous drop of the sample current. This positive feedback loop continues until the critical interaction

volume completely moves into the deposited material and then the chance for the incoming electrons to escape is not changing any more and the sample current reaches a plateau stage, which is the second stage of the growth. In this plateau stage the sample current stays constant and the cylindrical shaft starts to appear. Therefore, the number of the incoming electrons which escape from the sidewall and participate the dissociation reaches its maximum once the growth enters the second stage, which explains the sample current in the second stage is reaching lowest. It is noticed that in the case of the low beam current in the very beginning the sample current dropped to a very low level, in which the sample-current-to-beam-current ratio was close to that of the plateau stage in the high beam current deposition. Then the sample current bounced back a little and reached the plateau phase. This was the only observation that the sample current dropped to a low value and then jumped back to a higher value in all the sample current measurements.

A comparison of Figures 3.24 and 3.25 shows that the sample current took a longer time to drop down to the saturation level when an electron beam of higher current was employed, which is consistent with the observation from Bret et al.[134]. Here the amount of time that the sample current needs to reach the saturation is defined as the decay time. As we have learned previously, a cone tip is developed within the decay time and after that the growth switches the gear to a steady-state growth of a cylindrical shaft. And a larger beam current leads to a critical interaction volume with larger width and depth and it takes more time for the critical interaction volume moves out of the substrate material. Thus it is plausible that given the same gas supply it took a longer decay time for a higher beam current to complete the cone-growing stage in which the base width of the cone saturated.

In conclusion, we found out that by lowering beam current or increasing beam energy a sharp tip can be obtained. The chemical composition and density of the deposit was suggested uniform along its axial direction based on the observation that the saturation current does not vary with time. A “Snow-cone Cup” model was proposed for the deposit growth by EBID. Time-resolved sample current measurements revealed the

transition of critical interaction volume from the substrate material into the deposited material and this transition is dependent on beam current.

In the next section, we will take a break from the experiments and look at a new Monte Carlo simulation program and learn how it can be applied to our study on EBID.

3.4.2.3.5 NISTMonte and its application in complex sample geometries

Monte Carlo simulations of electron scattering provide a valuable tool for understanding the various signals that are generated when energetic electrons interact with solid. Many Monte Carlo simulations have been implemented for modeling the electron-solid interaction. Some of the well-known implementations are Joy's Monte Carlo[138], MOCASIM[139], NBSMonte[140], PENELOPE[141], Electron Flight Simulator[142], CASINO[143] and Win X-Ray[144]. However, there are two limitations for most programs. The first limitation is the capability to handle samples of complex geometries and the second the availability of source code. Electron Flight Simulator, CASINO and Win X-Ray do not provide open source code and are limited to simple sample geometries as well. NBSMonte and Joy's Monte Carlo models are available in source code but cannot deal with samples of complex geometries. PENELOPE is capable of complex geometries and provides source code but is far more complex and sophisticated. MOCASIM, which was developed by Dr. Ludwig Reimer and represented by Plano GmbH, was able to simulate electron scattering in complex sample geometries. After Dr. Reimer passed away, MOCASIM has been ceased in the market and excluded from the public.

NISTMonte[145], developed by Dr. Nicholas Ritchie from National Institute of Standards and Technology (NIST), is a new Monte Carlo simulation program for electron scattering, X-ray generation and transmission in complex sample geometries. NISTMonte adopts the Mott cross section [109, 146] to model elastic scattering and the Joy-Luo expression[147] to model energy loss. The ionization cross sections are modeled using

the empirical expression of Casnati[148]. The mass absorption coefficients are those of Heinrich[149].

Unlike the other Monte Carlo simulation programs, NISTMonte is an open source program and has the flexibility of defining complex sample geometries. And it provides a set of basic modules that could be combined to build complex sample shapes. Furthermore, inhomogeneous sample or structured samples could be modeled by embedding shapes within shapes.

The application has been developed in Java J2SE 1.4 for platform independence. The source code is available on the NIST web site. All the java classes have been built into the NISTMonte library and Jython, a Java implementation of the high-level, dynamic, object-oriented (OO) language Python seamlessly integrated with Java platform, is adopted to access the NISTMonte library to run Monte Carlo simulations.

In the NISTMonte samples are constructed from two types of objects – Materials and Shapes – which are combined to form Region objects. Complex samples could be formed by a combination of multiple region objects. The Material class represents what a region is made of and the Shape class represents the shape of the region. The original NISTMonte library offers four basic building blocks and two methods to combine these building blocks. The four basic shape classes include Sphere, SimpleBlock, MultiPlaneShape and CylindricalShape, as illustrated in Figure 3.27 and the two combining methods contain ShapeDifference and SumShape, as shown in Figure 3.28. The Sphere class constructs a spherical object with the specified center and radius. The SimBlock class constructs a simple block shaped object with its edges aligned with the coordinate axes and the size of the block is defined by two corners. The MultiPlaneShape class constructs a substrate, a block or a film or adds a bounding plane. The CylindricalShape class constructs a cylindrical object of arbitrary axis and radius. The ShapeDifference class creates a new shape by removing one shape from another. The SumShape class creates a new shape by summing up an array of shapes.

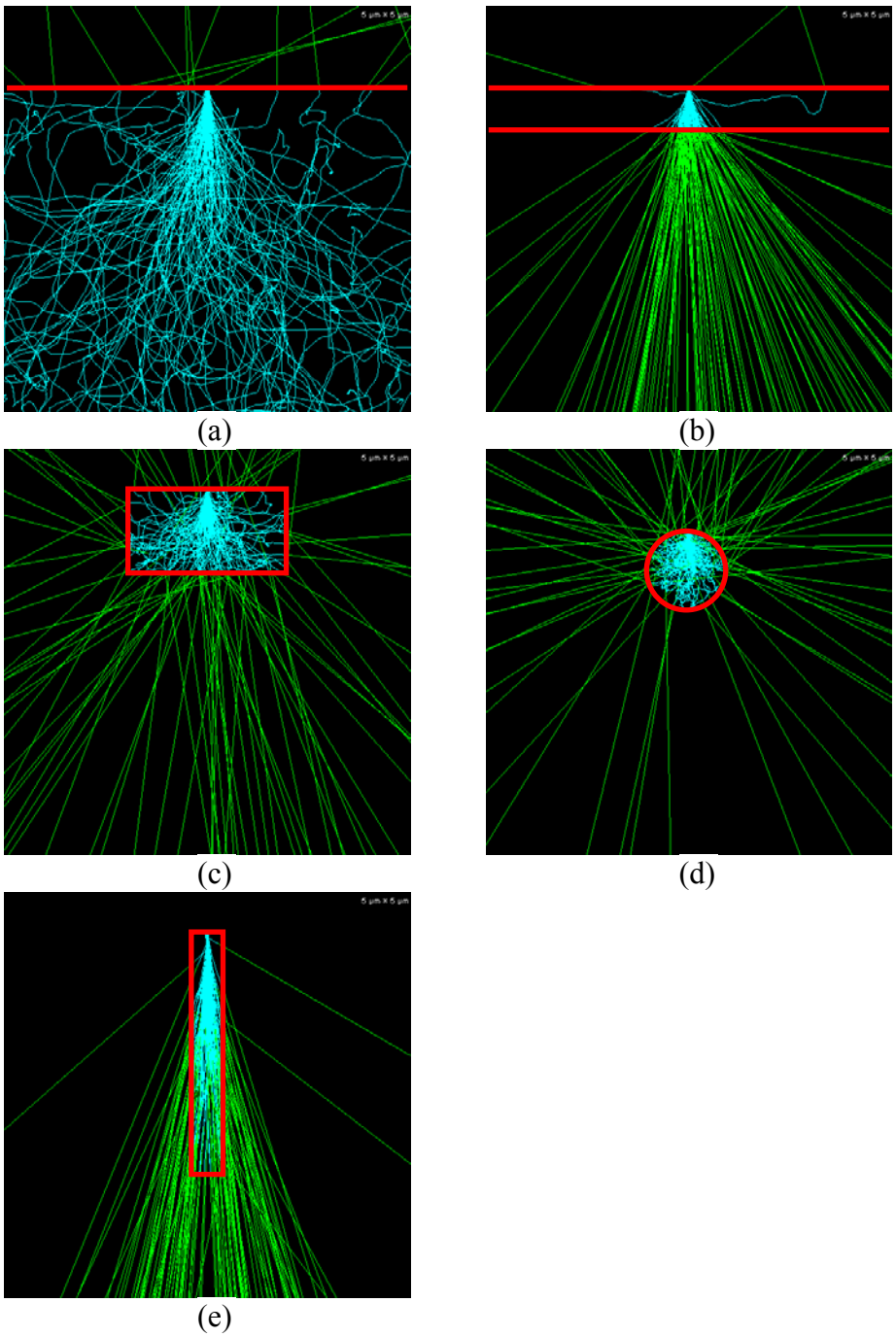

Figure 3.27 Geometries in NISTMonte

A series of images illustrate the five shapes provided in NISTMonte including a (a) bulk substrate, (b) thin film, (c) simple block, (d) sphere and (e) cylinder. The red lines form the geometry contours. The blue lines stand for the trajectories of electrons scattered in the solid and the green lines the trajectories of electrons traveling in vacuum.

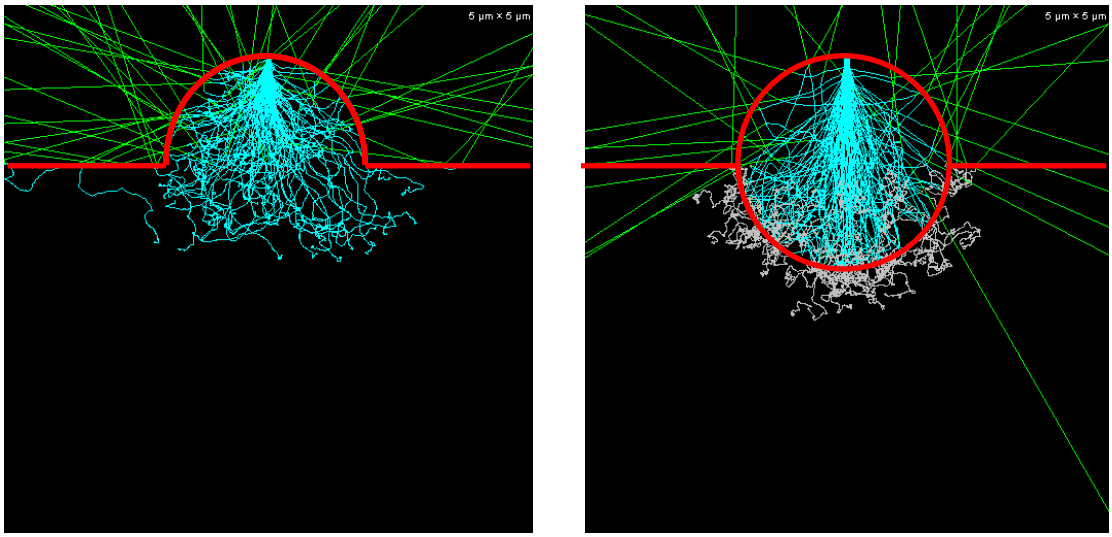

(a) (b)

Figure 3.28 Geometrical Operation in NISTMonte

A series of images illustrate the two combining methods provided in NISTMonte which include (a) SumShape that forms a bulk substrate with a hemispherical bump, and (b) ShapeDifference that forms a spherical particle embedded in a bulk substrate. The red lines form the contour of the geometries. The blue lines stand for the trajectories of electrons scattered in the solid. The green lines stand for the trajectories of electrons traveling in vacuum.

Though the NISTMonte library provides a number of useful basic shapes, the need for constructing a conical shape to model tips grown in EBID process is not quite well satisfied. The tips fabricated by EBID are of conical shape, and most of the tips in which we are interested are very sharp, i.e. they have a very small opening angle. The opening angle here is defined as the vertex angle made by a cross section through the apex and center of the base. As to the cones with large opening angle (about 90°) a hemisphere is a good approximate. As the opening angle of the cones shrinks down to less than 60°, a hemisphere is no longer a valid approximate for a cone. Thus it is desirable to implement a new shape class to approximate a cone.

In this work a TruncatedConicalShape java class was coded for this purpose and was included in the package gov.nist.microanalysis.NISTMonte. The TruncatedConicalShape implementation requires four inputs: the center position and radius of both the top end and the bottom end. By properly choosing the value of the radii the implementation can define a cone with one end of infinitesmal radius, or a frustum with two ends of unequal radius, or a cylinder with two ends of equal radius, as illustrated in Figure 3.29. The Java implementation is presented in Appendix B.

TruncatedConicalShape Class

{ Define an object constructor called TruncatedConicalShape() to create a TruncatedConicalShape object with specified end points and radii;

Define a method called clone() to create and return a copy of the object;

Define a method called closestPointOnAxis() to return the parameterized coordinate of the closest point on the object axis to the specified point;

Define a method called distanceSqr() to calculate the distance (squared) from the parameterized point on the object axis to the specified point;

Define a method called resultingRadius2() to calculate the closest distance (squared) from the parameterized point between two scattering positions to the object axis;

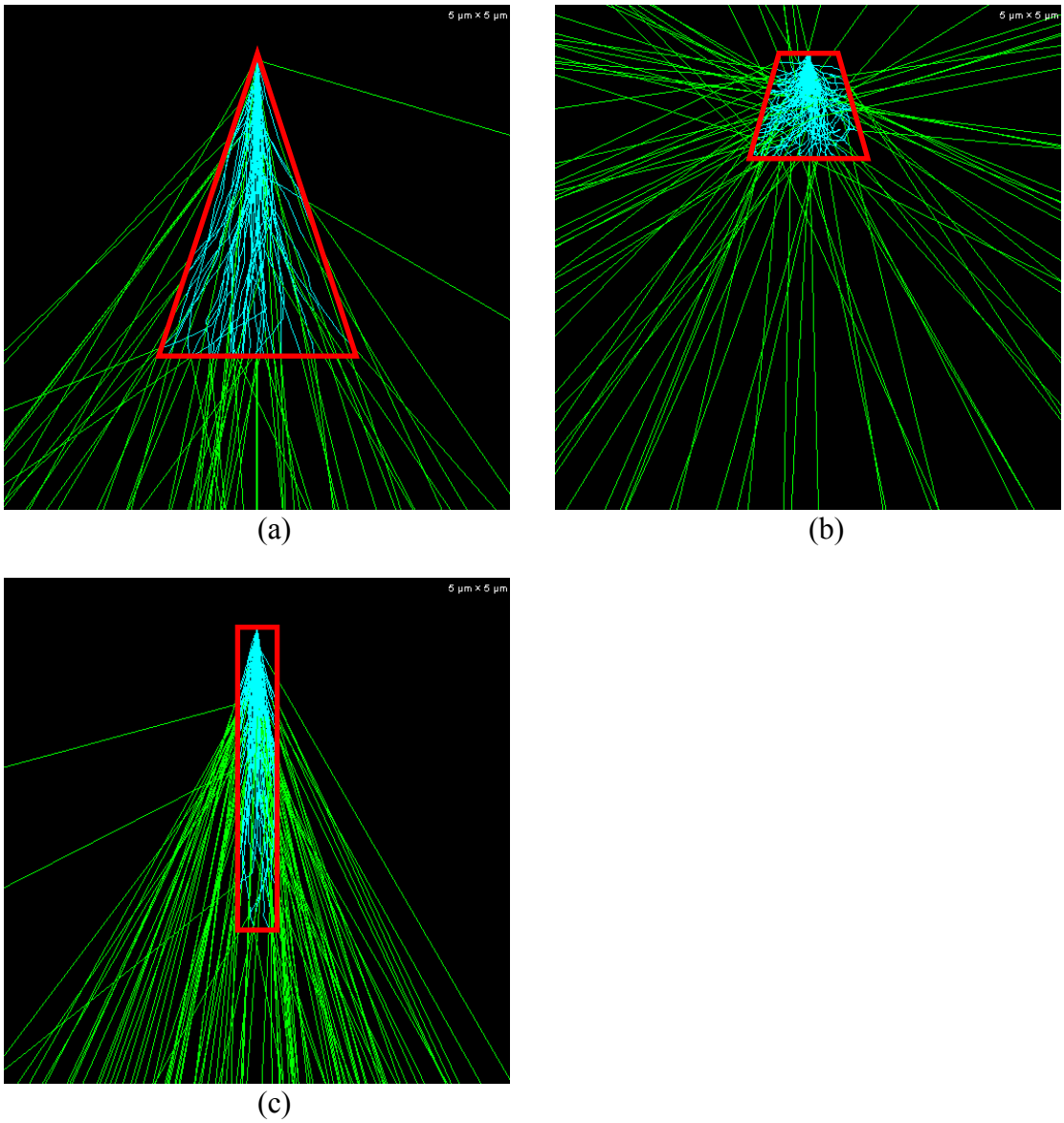

Figure 3.29 Geometries Provided by TruncatedConicalShape

A series of images show the TruncatedConicalShape implementation which provides three kinds of geometries: (a) cone, (b) frustum and (c) cylinder. The red lines form the contour of the geometries. The blue lines stand for the trajectories of electrons scattered in the solid. The green lines stand for the trajectories of electrons traveling in vacuum.

Define a method called surfaceRad() to calculate the radius of the circle formed by intersection of the object surface and a plane which is perpendicular to the object axis and contains the specified point;

Define a method called contain() to determine if the specified point is contained within the object boundary;

Define a method called getRadius0() to get the radius of the first end surface of the object;

Define a method called getRadius1() to get the radius of the second end surface of the object;

Define a method called getEnd0() to get the center position of the first end surface of the object;

Define a method called getEnd1() to get the center position of the second end surface of the object;

Define a method called isNearWall() to determine whether the parameterized point which is located between two scattering positions is near the specified wall;

Define a method called nearWall() to determine which wall the parameterized point which is located between two scattering positions is near;

Define a method call getFirstIntersection() to determine whether the travel path between two scattering positions intersects with the boundary of the object and if it does the fraction of the travel path within the object will be returned. getFirstIntersection() is an important method in this class and its algorithm will be detailed as follows:

{ The output value is set as the max value in Double format;

If the intersection point is located at the first end surface

{ Calculate the fraction, which is within the object, of the travel path between the two scattering positions and set it as the output value;}

Else if the intersection point is located at the second end surface

{ Calculate the fraction, which is within the object, of the travel path between the two scattering positions and set it as the output value;}

Else

{ Solve a quadratic equation to find the intersection position. The left side of the equation is a function of the intersection position to calculate the closest distance between the intersection position and the object axis and the right side of the equation is a function of the intersection position to calculate the radius of the circle formed by the object boundary and the plane which is perpendicular to the axis and also contains the intersection position. If there are solutions, it means the intersection point is on the sidewall. But we need to ensure the intersection point is between the two scattering points and also between the two end surfaces. Only when these two conditions are satisfied the solution gives the right answer and the output value will be set;}

Return the output value;}

Define a method called rotate() to rotate the object;

Define a method called translate() to translate the object;}

Below is shown a simple Jython example how to construct a WC nanofiber on a Si substrate and simulate electron scattering within the nanofiber and substrate and the simulated trajectory is shown in Figure 3.30. The script is shown as follows:

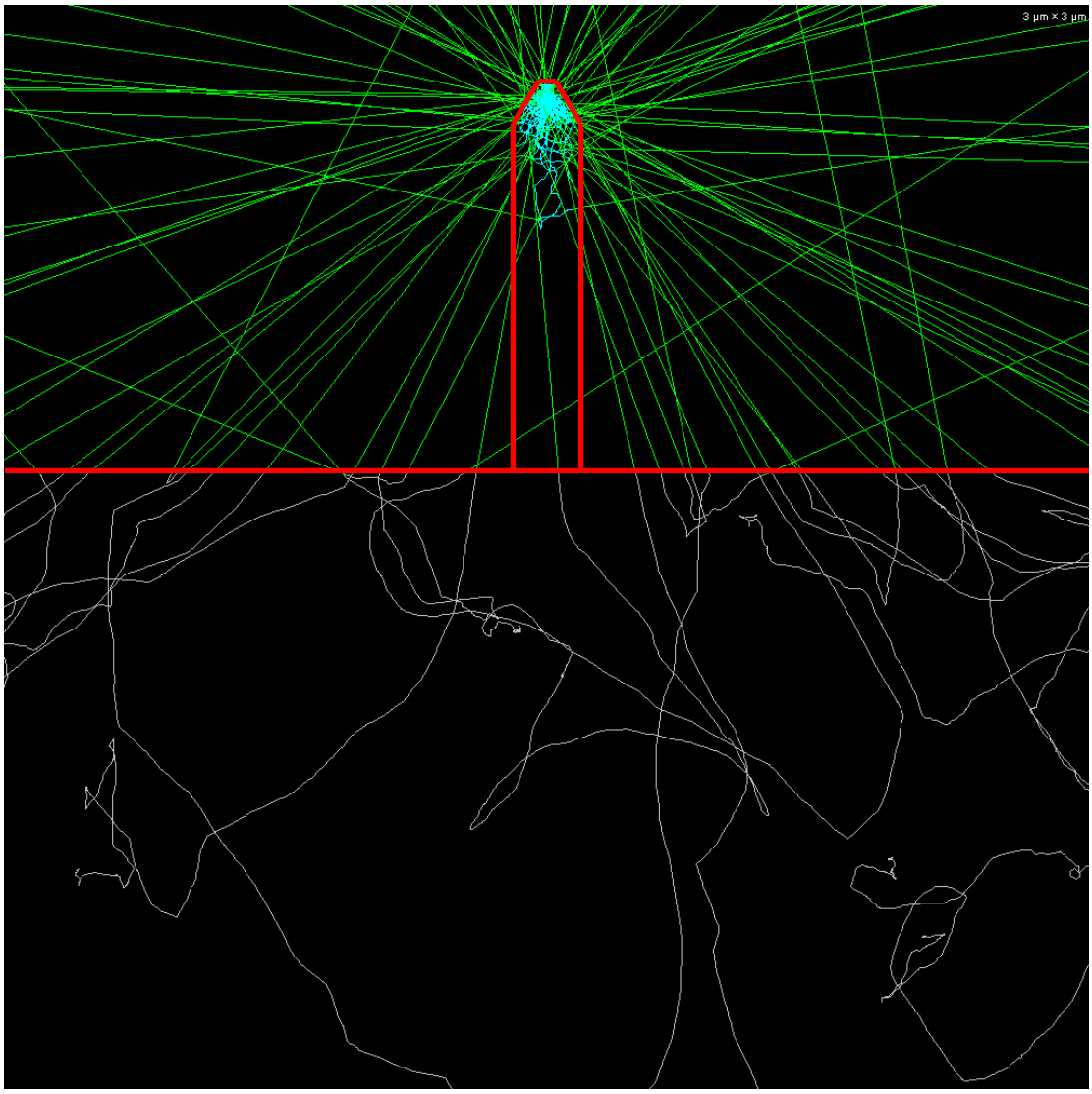

Figure 3.30 NISTMonte Application in EBID

An electron trajectory image simulating electron scattering in a WC nanofiber and Si bulk substrate constructed by NISTMonte. The red lines form the contour of the geometries. The blue lines stand for the trajectories of electrons scattered in the nanofiber and the white lines in the substrate. The green lines stand for the trajectories of electrons traveling in vacuum.

(1) Importing external libraries

The scripting environment provides some built-in basic functionality and the external libraries could be loaded to access these functionality. The NISTMonte library is loaded using the statement:

```
import gov.nist.microanalysis.NISTMonte as nm
```

The “nm” is an alias for the NISTMonte library. And the other libraries required for this example are imported as follows:

```
import gov.nist.microanalysis.EPQLibrary as epq

import java.io as io

import java.imageio as imgio
```

(2) Configuring an electron gun and constructing a substrate and nanofiber

An electron gun is defined and configured. The electron gun is defined as a Gaussian beam with beam energy of 50keV and probe size of 10nm.

```
monte=nm.MonteCarloSS()

monte.setBeamEnergy(epq.ToSI.keV(20.0))

monte.setElectronGun(nm.MonteCarloSS.GaussianBeam(monte,10.0e-9))
```

The materials for the substrate and nanofiber are defined. The substrate is silicon, and the nanofiber is WC.

```
mat1=epq.MaterialFactory.createPureElement(epq.Element.Si)

mat2=epq.Material()
```

```
mat2.defineByMoleFraction([epq.Element.W,epq.Element.C],[1.0,1.0])

mat2.setDensity(epq.ToSI.gPerCC(15.8))

mat2.setName("WC")
```

The shapes for the substrate and nanofiber are constructed. The silicon substrate is a bulk and the WC nanofiber has a cylindrical shaft with length of 1μm and radius of 80nm and a frustum top with length of 80nm and radii of 20nm and 80nm.

```
subs = nm.MultiPlaneShape.createSubstrate([0.0, 0.0, -1.0],[0.0, 0.0, 1.0e-6])

subReg = monte.addSubRegion(monte.getChamber(), mat1, subs)

cylinder = nm.CylindricalShape([0.0,0.0,0.0],[0.0,0.0,1.0e-6],80.0e-9)

cone=nm.TruncatedConicalShape([0.0,0.0,-80.0e-9],[0.0,0.0,1.0e-9],20.0e-9,80.0e-9)

fiber= nm.SumShape(cone,cylinder)

monte.addSubRegion(monte.getChamber(), mat2, fiber)
```

(3) Running the simulation and outputting the trajectory image

A trajectory image with resolution of 2048×2048 and size of 3μm×3μm is generated and saved to the desired folder.

```
img=nm.TrajectoryImage(2048,2048,3.0e-6)

monte.addActionListener(img)

monte.runMutipleTrajectories(1000)

dest="c:\\temp\\fiber\\"
```

```
io.File(dest).mkdirs()

img.dumpToFile(dest)
```

3.4.2.3.6 Extended experiment II and discussion

In this section we are going to revisiting the SE-yield experiment in which the deposition was made on both silicon and tungsten substrates using 5 and 20 keV electron beam. This time the measurement of time-resolved sample current would be performed and it can give us an opportunity to investigate the growth kinetics under various conditions.

The experiment procedure was basically the same as in the SE-yield experiment except no tilted samples this time. The beam currents of both the 5 and 20 keV electron beams were calibrated to about 60 pA using a Faraday cup under a base pressure of 6.8×10^{-5} Pa. The deposition was carried out on the silicon and tungsten substrates individually and for each substrate both the 5 and 20 keV electron beams were adopted for deposition. The chamber pressure was set to around 6×10^{-3} Pa during the deposition. Every time when a deposit was grown, a time-resolved sample current was collected by a Keithley 6485 Digital picoammeter through the grounding port of the SEM and plotted by ExceLINX software on a computer. During the measurement the picoammeter read the sample current every 0.1 s for 200 s. The plots of time-resolved sample current for the four growth conditions are illustrated in Figure 3.31.

The measurement from the SEM micrographs shows that the cone length of the nanofibers grown at beam energy of 20kV was slightly larger than 5kV by roughly 10~20nm. This agrees with the observation by Schiffmann[17] that the cone length increased with the accelerating voltage even though the difference was not significant in this experiment. The beam-energy dependence of cone length sounds reasonable because the length of the interaction volume under high beam energy is longer as high energy electrons can penetrate deeper into the sample. The possible explanation for the insignificant difference of cone length under different beam energies is that in the case of

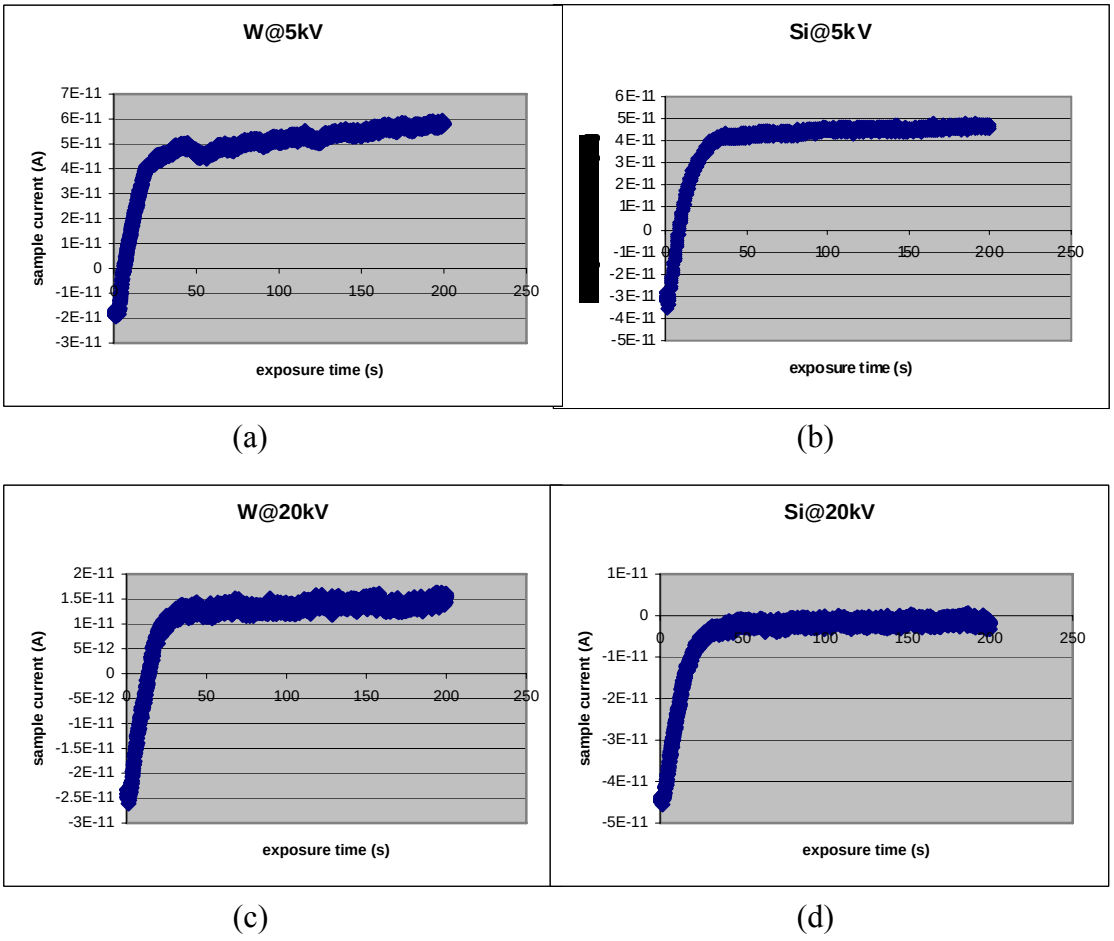

Figure 3.31 Sample Current Monitoring under Various Conditions

A series of plots illustrate the time-resolved sample current measured under the following growth conditions: (a) 5 keV beam energy and W substrate; (b) 5 keV beam energy and Si substrate; (c) 20 keV beam energy and W substrate; (d) 20 keV beam energy and Si substrate.

small beam current (~50pA) the lengths of the critical interaction volumes under both 5 and 20keV were not significantly different. The dimension difference of the critical interaction volumes under these two beam energies would have become significant if the beam current had increased to a larger extent (~nA).

From the plots shown in Figure 3.31 it can be seen that for all growth conditions the sample current decreased rapidly and reached the plateau stage within about the same amount of the decay time which is defined as the time between the starting point of the deposition and the turning point from the decay region to the plateau region. For most conditions the sample current dropped so much that it entered the positive-current region. The rapid decrease of the sample current has been explained in Section 3.4.2.3.4. Here what is interesting is that the sample current changed from negative value to positive value, which indicates that more electrons were scattered away from the sample and entered into vacuum than the incoming electrons. The explanation exists in SE. The incoming electrons enter the apex of the nanofiber, and some of them are scattered back into the vacuum immediately while most of them experience a number of scattering and then escape from the sidewall of the nanofiber. A fraction of these escaping electrons reach the sample and are collected as sample current. All these scattering events generate BSE or SE: elastic scattering causes BSE and inelastic scattering causes SE. BSE originate from the incoming electrons and they do not induce positive charges, i.e. holes. On the contrary, SE are the electrons knocked out from the sample and nanofiber by incoming electrons, and those slow SE of <50eV in the near surface and fast SE of high kinetic energy in the deep region are capable to flee from the solid. Thus, their escape leaves holes within the sample or nanofiber. When the total number of holes generated by SE exceeds the number of the incoming electrons absorbed by the sample and nanofiber, the sample and nanofiber are then positively charged and a positive sample current is observed. The SE yield data in Joy's Electron Solid Interaction Database[150] indicates that the SE yield exceeds 1 at excitation energy between 200 and 600eV.

Figure 3.31 indicates that under the beam current employed in this experiment the decay time in which the critical interaction volume completely enters the deposited

material was independent of substrate material and beam energy. This disagrees with the commonly accepted dependence of growth on beam energy and material type. Especially during the decay region in which the rapid sample-current drop occurs it is generally thought that a 20keV beam forms a longer interaction volume and causes a slow deposition rate than a 5keV beam and therefore it takes longer for the sample current to reach the steady-state value in the case of the 20keV beam than the 5keV beam. The reason for this discrepancy is not very clear. One possible explanation is that the interaction volumes for 5 and 20keV are comparable because the beam current was not large enough as suggested from the measured cone lengths. Meanwhile the vertical growth seems to be driven by the incoming PE, which will be discussed later in Section 3.4.2.5. Both 5 and 20keV electrons are in the tail of the ionization cross-section curve for WF_6, which indicates their ionization cross-section are similar. And in this study the beam current for both beams was calibrated to the same. The vertical growths for both beams were then comparable due to the same beam current and the comparable ionization cross-section. Therefore the time for the current decay under the two conditions are similar.

In addition, compared with Figures 3.24 and 3.25, it can also be seen that the decay time was a function of beam current and increased with the beam current, which agrees with our proposed theory that a larger beam current causes a larger critical interaction volume and it takes a longer time for a larger critical interaction volume to move into the deposited material from the substrate.

Once the sample current reached the plateau region at which the critical interaction volume entered the deposited material completely, it remained stable at the saturation value. The cylindrical growth began to take place of the conical growth. It is speculated that during cylindrical growth most of the critical interaction volume resides within the conical top of the deposit and the maximum width of the critical interaction volume occurs around the bottom edge of the conical top. The reasoning is put as follows. From definition the critical interaction volume is the volume within whose boundary the electron density and dissociation cross-section of electron flux are efficient enough to

make deposition happen. And outside this volume the electron flux cannot dissociate the precursor molecules and no deposition happens. If the maximum width of the critical interaction volume occurs somewhere below the bottom edge of the conical top, the solid angle of the critical interaction volume is smaller than that of the conical top. Then the deposition between the two solid angles should not have happened since it is outside of the critical interaction volume. If the maximum width of the critical interaction volume occurs above the bottom edge of the conical top, the solid angle of the critical interaction volume is larger than that of the conical top. So the solid angle of the conical top will increase as the deposition continues, which is contradictory to the observation in our work that the solid angle of the conical top never changes during deposition. Therefore, the geometry of the critical interaction volume above its maximum width should be the same as the conical top. This information is very useful as we can estimate the density and energy distribution of electron flux on the surface of the conical top by Monte Carlo simulation, and use this information to write simulation programs to model the deposition process.

In Section 3.4.2.3.4 we have learned that the cone angle increased with beam current because of the expanding critical interaction volume. Now looking at Figure 3.22, we can easily see that the cone angles increased with decreasing beam energy while they were insensitive to substrate material. The fact that the cone angles increased with decreasing beam energy agrees with the observation from the other groups[17, 51, 82, 125]. Schiffmann[17] suggested that the conical part of the tip is defined by the mean maximum electron path length inside the tip. As the total cross section for electron scattering and the mean scattering angle decrease with electron energy, the path length increases with electron energy. In other words, increasing beam energy makes the critical interaction volume longer and more acute and the cone becomes longer and more acute. Further, the result that the cone angles were not affected from the substrate materials indicates that the compositions of the deposits were not influenced by the substrate materials. Otherwise, the cone angle of the deposits on different substrates would have been different even though the beam current and beam energy were the same, as

suggested by the simulation of Weber et al.[51] that the cone angle should increase with atomic number of tip material. In conclusion, besides that low beam current gives sharp field emission tips as discussed in Section 3.4.2.3.4, there are two more suggestions for growing sharp field emission tips: using high beam energy and the substrate materials do not matter.

Next we will discuss the relation between sample current and electron scattering events. The general form of sample current for a flat surface can be expressed in Eq. 3.10.

$$i_{SC} = i_{PE} - \left(i_{BSE} + i_{SE}\right) - \frac{dQ}{dt} \qquad 3.10$$

in which i_{SC} is sample current, i_{PE} is primary electrons, i_{BSE} is backscattered electrons, i_{SE} is secondary electrons and $\frac{dQ}{dt}$ is the charging term, which in semiconductors and metals can be eliminated. Eq. 3.10 can be used for the sample current at the starting point of the deposition. The time-resolved sample currents in Figure 3.31 show under different conditions the sample currents at the starting point were different. At the starting point the primary electrons only interacted with the substrate materials and no new material was deposited on the substrate yet. The sample current was determined by the yield of backscattered electrons and secondary electrons from the substrate materials. By comparison of the yields of backscattered electrons and secondary electrons of both tungsten and silicon at 5 and 20 kV, it can be easily seen that the sample currents at the starting point of the measurement is consistent with Eq. 3.10.

However, as the deposit starts to appear, Eq. 3.10 is not valid any longer. A new expression for the sample current needs to be derived. Figure 3.32 is a schematic illustration of electron scattering within the deposit and sample. Three types of backscattered electrons and secondary electrons are defined. BSE1 and SE1 are the backscattered electrons and secondary electrons which are generated by the primary electrons from the tip of the deposit and travel at a deviation angle of 90° or larger off the direction of the primary electrons. They are not able to be collected as the sample current.

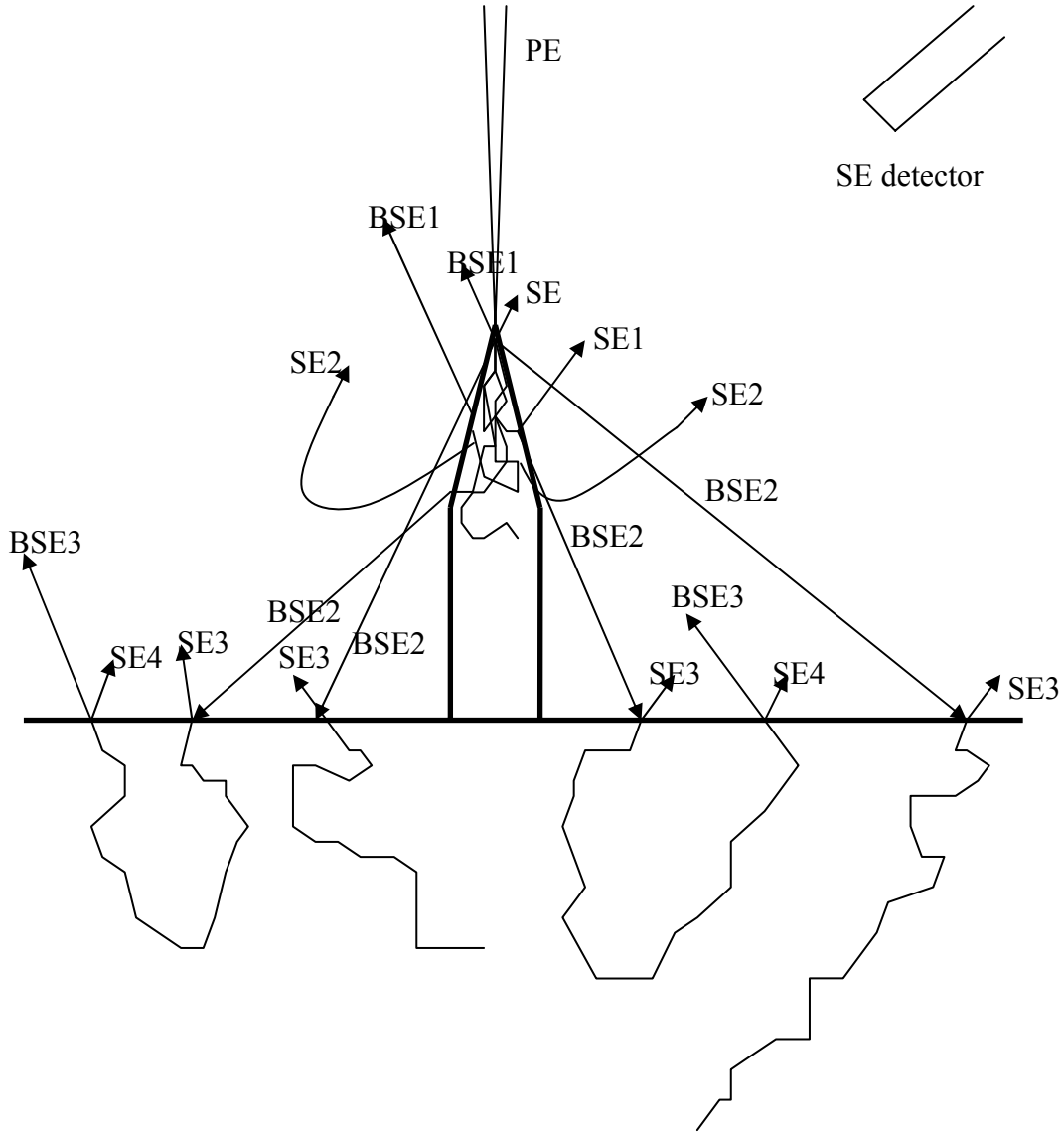

Figure 3.32 Schematic Electron Scattering during EBID

A schematic diagram of electron scattering in both the tip and the substrate. PE stands for primary electrons, BSE1 and SE1 stand for the backscattered electrons and secondary electrons which escape from the tip and travel at a deviation angle of 90° or larger off the incident direction. BSE2 and SE2 stand for the backscattered electrons and secondary electrons which escape from the tip and travel at a deviation angle of less than 90° off the incident direction. BSE3 stands for the backscattered electrons which escape from the substrate. SE3 and SE4 stand for the secondary electrons which are emitted on the surface, respectively, at the entry of BSE2 and the exit of BSE3.

BSE2 and SE2 are the backscattered electrons and secondary electrons which are also generated by the primary electrons from the tip but travel at a deviation angle of less than 90° off the direction of the primary electrons. Here the tip height is several orders smaller than the dimension of the sample and the sample surface can be treated as infinite-large so that BSE2 can reach the sample surface and continue to be scattered in the sample. SE2 cannot reach the sample as sample current since the bias on the SE detector eventually pull all the SE2 away from the sample. BSE3 and SE3 are the backscattered electrons and secondary electrons which are generated by BSE2 from the sample. They escape from the sample and are not collected as the sample current. It should be aware that three types of BSE and SE are different from Type I and II of BSE and SE defined previously. Therefore, Eq. 3.10 can be evolved into Eq. 3.11.

$$i_{SC}^{sat} = i_{PE} - \left(i_{BSE1} + i_{SE1}\right) - i_{SE2} - \left(i_{BSE3} + i_{SE3} + i_{SE4}\right) \qquad 3.11$$

From Figure 3.31 it can be seen that the sample current varied with the beam energy and substrate material. The deposition at 5kV gave a saturation current of around +50pA for both the tungsten substrate and the silicon substrate. The deposition at 20kV gave a saturation current of around +13pA for the tungsten substrate and around –4pA for the silicon substrate. From that two conclusions are made here.

First, the current drop at low beam energy was larger than at high beam energy since the beam current was -60 pA. NISTMonte simulation program was used to model electron scattering in the nanofiber and substrate and the results are shown in Figure 3.33. The simulation shows that at 5kV only a small fraction of the incoming electrons can travel toward to the sample after scattered out the nanofiber while at 20kV over half of the incoming electrons can reach the sample. In other words, at 5kV the number of BSE1 was close to that of PE and also generated a large number of SE1 because of the high SE yield of tungsten at low energy. This is why during deposition at 5 kV the sample current not only dropped to positive region but also reached a large positive value. At 20kV the BSE1 was less than half of PE and the SE1 and SE2 were low as well due to the comparably low SE yield of tungsten at 20 kV. In addition, at 20kV the BSE2 arriving at

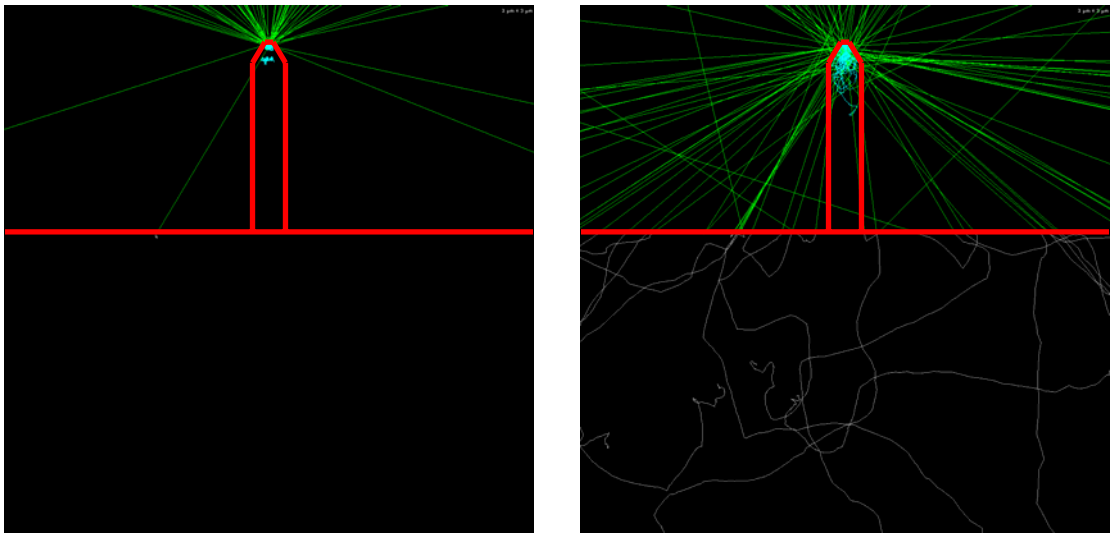

(a) (b)

Figure 3.33 Interpretation of Sample Current Results by NISTMonte

A series of images show the Monte Carlo electron scattering simulation of a (a) 5keV and (b) 20keV electron beam within a W nanofiber and a Si substrate on which the nanofiber sits on. The simulation was carried out by using NISTMonte.

the sample had low SE yield because the BSE2 were almost as energetic as PE due to the only few scattering in the nanofiber and they generated low number of SE3 on the sample surface. So most of the BSE2 were absorbed by the sample while the holes generated by the emitted SE1, SE2, SE3 and SE4 were small compared with the case at 5 kV. All above contributed to the result that the sample current loss at 5 kV was double the current loss at 20 kV.

A more intuitive illustration will be presented in this paragraph to simplify the rationality narrated above. Here let us consider $PE = 1000$. With the help of NISTMonte simulation shown in Figure 3.33 and available BSE and SE yield data[151, 152], sample current drop for both cases of 5keV and 20keV beams can be estimated for comparison with the experimental result. It should be noted that the simulations only show the trajectories of BSE while SE can only be estimated from the yield data. In the case of 5keV beam, Figure 3.33(a) shows almost all electrons are backscattered, i.e. $BSE1 \approx 1000$ and $BSE2 \approx 0$. Thus BSE3, SE3 and SE4 can be neglected and only BSE1, SE1 and SE2 are considered. The total number of SE1 and SE2 is determined by the number of BSE1 and the SE yield of 5keV electrons on tungsten, as shown in expression $SE1 + SE2 \approx BSE1 \times \delta = 1000 \times 0.6 = 600$. Then $SC = PE - BSE1 - SE1 - SE2 = -600$. While at the beginning electrons only interact with the Si substrate, the sample current is determined by the expression $SC' = PE - BSE - SE = 1000 \times (1 - 0.2 - 0.24) = 560$. Thus the sample current drop is $\Delta SC = SC' - SC = 1160$. In the case of 20keV beam, Figure 3.33(b) shows about one third of PE are scattered backward and the rest reach the substrate and only a small portion (about 10% of PE) then leave the surface, i.e. $BSE1 \approx 300$, $BSE2 \approx 700$ and $BSE3 = 100$. Since the SE yield of 20keV electrons on tungsten is 0.3, $SE1 + SE2 \approx (BSE1 + BSE2) \times \delta = 300$. When BSE2 reach the Si surface, they generate $SE3 \approx BSE2 \times \delta = 700 \times 0.1 = 70$. Only a small portion which is estimated to be 10% of PE can eventually escape from the substrate and these are of very low energies but high SE yield estimated to be 0.9. This portion is $SE4 \approx BSE3 \times \delta = 100 \times 0.9 = 90$. The sample current is then $SC = PE - (BSE1 + SE1) - SE2 - (BSE2 + SE3 + SE4) = 140$. While the initial sample

current is $SC' = PE - BSE - SE = 1000 \times (1 - 0.17 - 0.1) = 730$. Thus the sample current drop is $\Delta SC = SC' - SC = 580$. The estimated sample current drop for 5keV beam is about twice larger than 20keV beam which is in agreement with the experimental result.

The second conclusion is that the influence of substrate material was trivial at low beam energy and became more significant as the beam energy increased. This probably comes from what fraction of the PE, i.e. BSE2, can reach the substrate and the BSE3 and SE3 that the BSE2 can generate from the substrate material. From Figure 3.33 it can be seen that at 5kV almost all the PE were scattered back to the vacuum and very few electrons could get to the substrate. Therefore the influence of substrate material on saturation current was negligible at 5kV. While at 20kV more than half of the PE arrived at the substrate and the influence of substrate material can not be put aside any more. Normally tungsten has a higher BSE and SE yields than silicon given the same energy, which means fewer electrons were absorbed and more holes were generated in the tungsten substrate than the silicon substrate. This explains at 20kV the current loss on the tungsten substrate was larger than the silicon substrate. In conclusion, the saturation current is less dependent on substrate materials at low beam energies and the dependence of saturation current on substrate materials increases with beam energy.

In conclusion, the size of critical interaction volume is dependent on beam energy. The relation between the critical interaction volume and the conical top was discussed. The sharpness of the tip was found to vary with beam energy but not substrate material. The relation between electron scattering and time-resolved sample current was discussed.

3.4.2.4 The BSE broadening experiment

3.4.2.4.1 Introduction

In electron microscopy, the broadening effect caused by BSE is a serious problem for SE imaging. As illustrated in Figure 3.3, SEI, which are generated from inelastic scattering of primary electrons penetrating the first 5-10 nm of the sample, are sensitive to conditions in the beam impact region and can provide high-spatial-resolution

information as the incident beam is finely focused. Meanwhile a small fraction of the primary electrons suffer high elastic-scattering angle promptly leave the sample in the immediate vicinity of the beam impact region and they are designated as BSEI. The rest of the primary electrons keep traveling forward into the sample. Some travel a long distance and then head back and escape from the surface. These are designated as BSEII and are the dominant part of the total BSE and are emitted over a much larger area with a diameter similar to the Kanaya-Okayama range of the beam below the surface. As the BSEII pass through the surface of the sample, the secondaries generated along the path within 5-10 nm of the surface, which are defined as SEII, are capable to escape and they are not capable to carry high-spatial-resolution information since they spread over an area of a diameter close to the Kanaya-Okayama range, as illustrated in Figure 3.34. Unfortunately these SEI and SEII have the same energy and angular distribution and cannot be separated on any physical basis. For the beam energy range 10-20 keV which is typically selected for SEM, the SEII emitted over a sufficiently large area ensure that any response to fine-scale details in the immediate vicinity of the beam is overwhelmed by longer-range effect. Thus the broadening effect generated by electron beam of energy range 10-20 keV makes high resolution microscopy difficult. The only way to achieve high resolution images for the energy range 10-20 keV is to reduce the sample to a thin film so that the beam broadening effect from BSEII could be eliminated.

Coming back to our experiment, the object is to find out what particle, SE or BSE, dominates EBID growth. Though it is generally observed that the lateral size of deposited dots is larger than probe size, which most people easily consider as a result from the beam broadening effect caused by BSE, it is still not clear whether it is SEII generated by BSEII or BSEII themselves that dissociate precursor adsorbate on the surface. Inspired by that thin films can help remove beam broadening effect, a thin film material would be adopted to remove BSE (both BSEI and BSEII). Lines were going to be deposited on both a thin film and a bulk material at the same conditions. If SE is the driving force, it will be seen that a thin line grows on the thin film due to SEI from the beam impact area while a thick line grows on the bulk material due to both SEI from the beam impact area

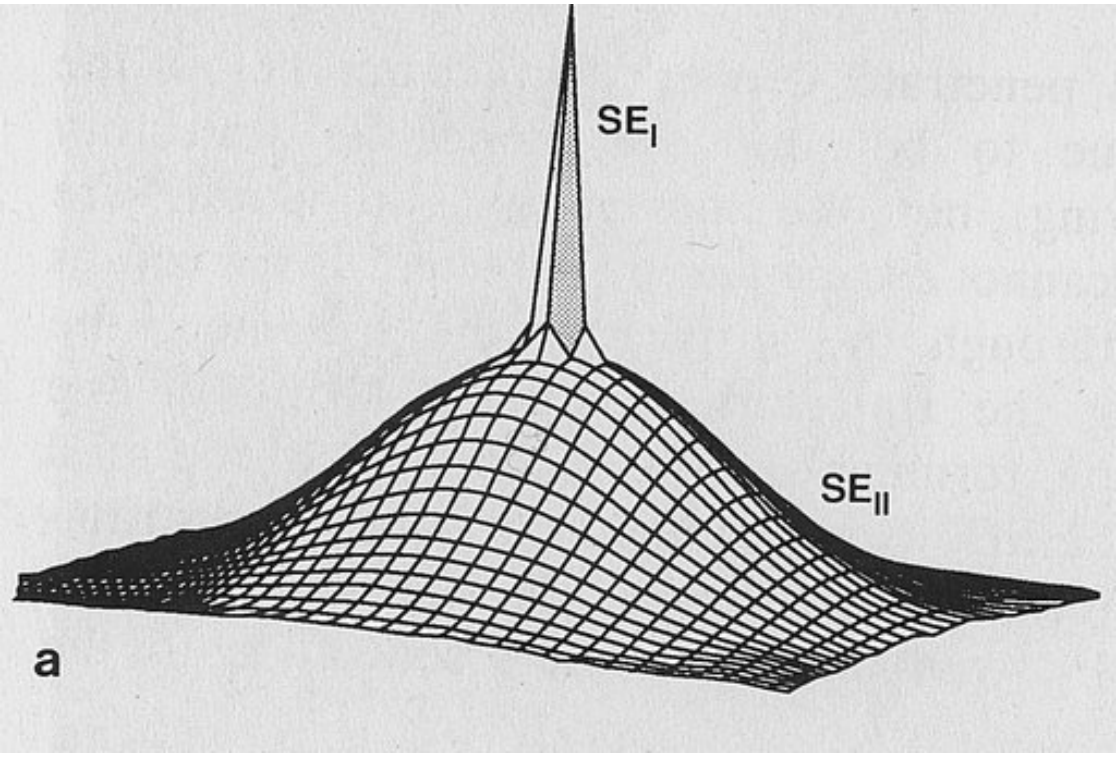

Figure 3.34 Comparison of SEI and SEII Emission

A simulated image of secondary electron emission for a 1-nm, 30-keV probe focused onto a silicon target. The SEI has a FWHM of 2 nm while the SEII component has a FWHM of approximately 10 μm.

and SEII from the vicinity area. If BSE is the driving force, it will be seen that no line is formed on the thin film because all electrons will pass through it and a line is formed on the bulk material.

3.4.2.4.2 Experimental set-up

In order to easily compare the results between a thin material and bulk material, a SPI^{TM} silicon nitride (Si_3N_4) membrane window grid for TEM was used to provide both a Si_3N_4 thin film and Si bulk substrate. The Si substrate is 200 μm thick and in the center has a Si_3N_4 membrane window of 100 nm thick and 0.5 mm wide, as shown in Figure 3.35. The Si_3N_4 film was deposited to the desired thickness, 100 nm in our case, on the Si substrate and then the Si substrate was etched through from the backside to the Si_3N_4 film, thereby producing the membrane window. Lines were going to be deposited across the boundary between the thin film and bulk substrate so that difference between the part on the thin film and that on the bulk substrate would be easily detected.

A STEM sample holder was used to ensure all the transmitted electrons are not reflected back to the membrane and Figure 3.36 illustrates how it works. W lines were deposited across the boundary on both the Si substrate and Si_3N_4 thin film at beam energy of 5, 10, 20 and 30 keV for 3 minutes. The base pressure of the chamber was maintained in the range 4.0×10^{-3}~5.5×10^{-3} Pa during the experiment.

3.4.2.4.3 Results and discussion

SEM micrograph of the lines is illustrated in Figure 3.37(a) and high-magnification micrographs of each line in Figure 3.37(b) through (e). All the micrographs were taken at 5 keV and the dark region is the Si substrate and the bright region is the Si_3N_4 thin film. The proposal that BSE drive EBID can be thrown out immediately since no line would have grown on the thin film if that is true. For the proposal that SE drive EBID, we need to measure the line width to see whether there was any difference.

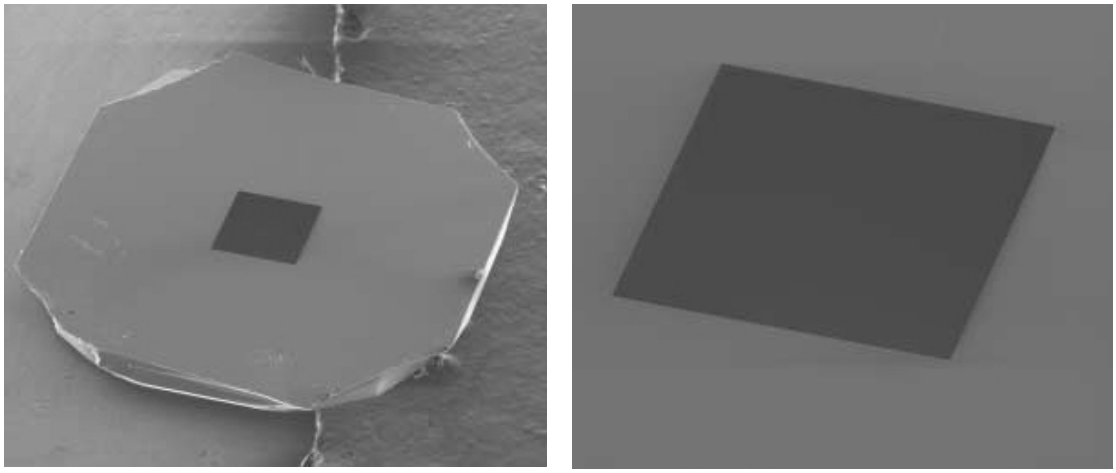

(a) (b)

Figure 3.35 Si_3N_4 Membrane Window Grid

Electron micrographs of the reverse side of a Si_3N_4 membrane window grid showing (a) 3 × 3 mm grid and (b) 0.5 × 0.5 mm membrane window (courtesy to www.2spi.com).

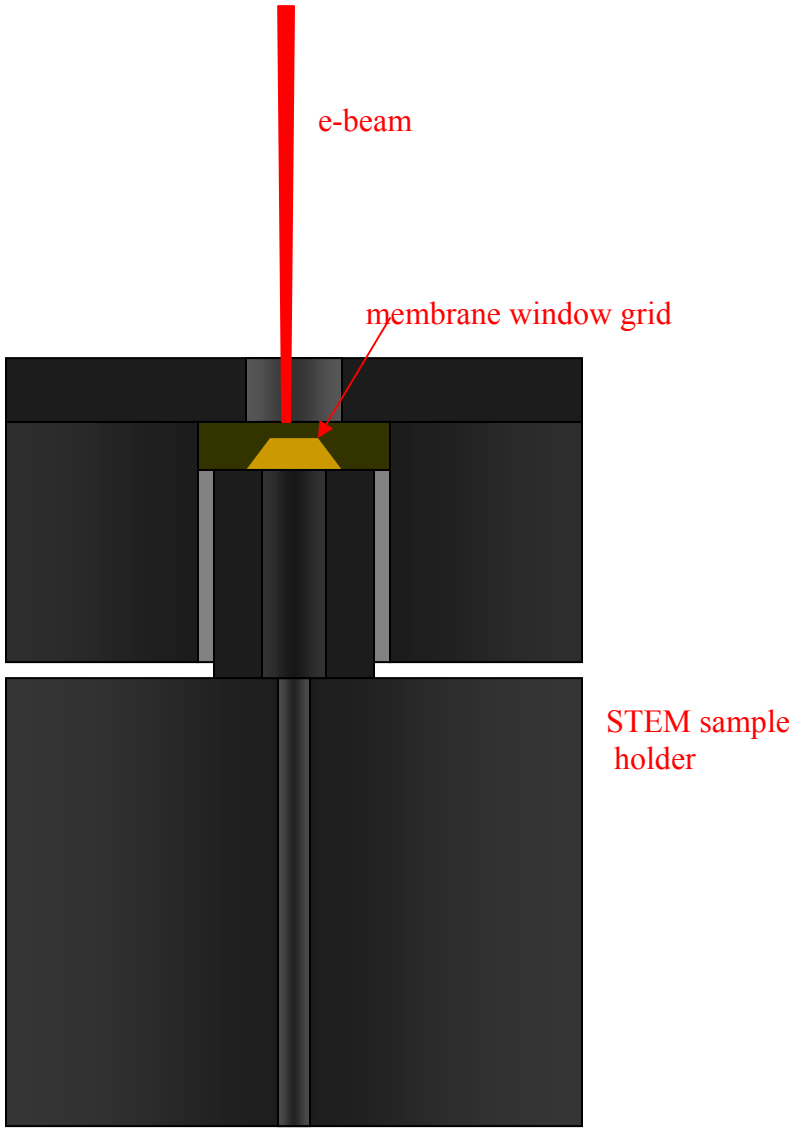

Figure 3.36 Schematic Set-up for BSE Broadening Experiment

A schematic illustration of the set-up of the Si_3N_4 membrane window grid in a STEM sample holder.

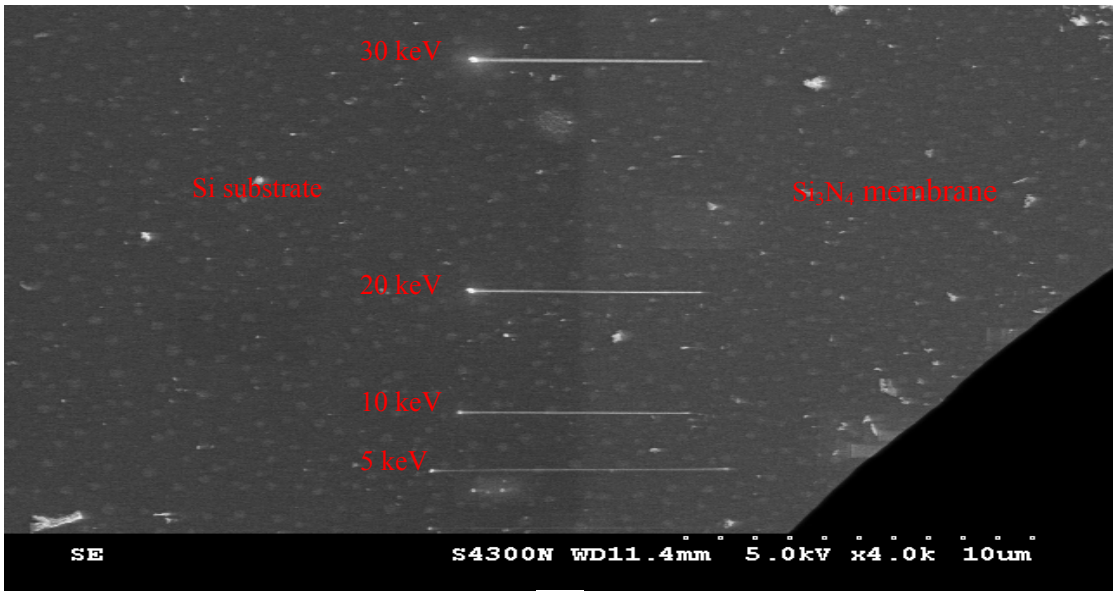

(a)

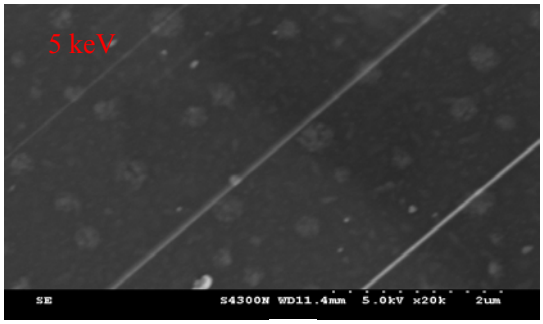

(b)

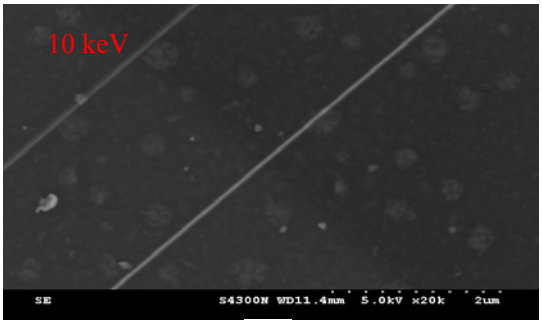

(c)

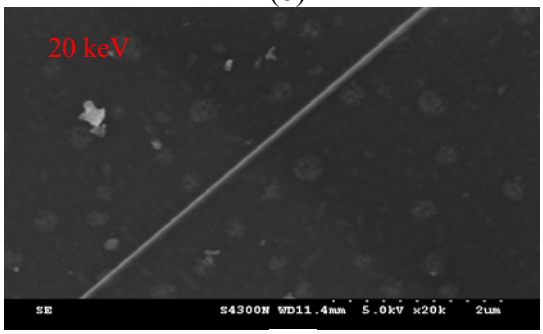

(d)

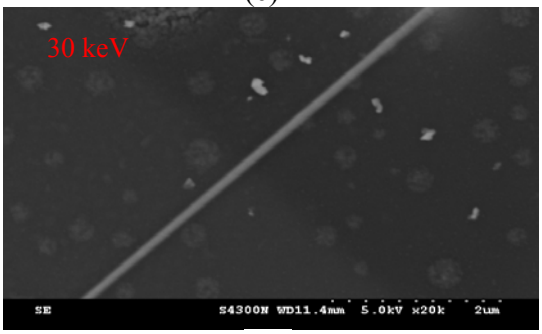

(e)

Figure 3.37 Result of BSE Broadening Experiment

Electron micrographs of (a) all the deposited lines, (b) the line deposited at 5 keV, (c) the line deposited at 10 keV, (d) the line deposited at 20 keV and (e) the line deposited at 30 keV.

SE intensity waveforms are generated for line width measurement by selecting a rectangular box across the line in ImageJ which is developed by National Institutes of Health (NIH). All the intensity waveforms are Gaussian and it is difficult to locate actual edges of the lines. The method employed in this work is called threshold algorithm which is commonly practiced in critical dimension (CD) metrology. In CD metrology accuracy is very important. CD-SEM is one good example of the widely used instruments in modern CD metrology. It measures line widths from image intensity waveforms, which are derived from characteristics of electron-beam-sample interaction. These image intensity waveforms contain characteristic intensity peaks at the lines' edges which seem to make measurement easy. However, there still exists a rather larger uncertainty for the location of the actual line edges due to the width of the intensity peaks. Further, the shape of the intensity peaks depends upon many factors such as energy of incident beam, material and geometry of the lines, surrounding features, charging effect and configuration of the detector. All these factors influence the shape of the intensity peaks, which makes accurate line width measurement extremely difficult. Common edge detection algorithms provided on CD-SEMs include peak-to-peak algorithm, threshold algorithm, maximum slope algorithm and linear regression algorithm, as illustrate Figure 3.38. None of the above algorithms is satisfactory for accurate line width measurement. However, in this study the goal is to measure line width not for accuracy but for comparison. As long as all the measurements are performed according to the same algorithm, they will be good enough for the comparison. Threshold algorithm, which is adopted in this study, will be discussed in detail next.

In this work a 50% threshold algorithm, as shown in Figure 3.39, was selected for edge determination. The practice of line width measurement is demonstrated by ImageJ in the following steps:

Step (1) Select a rectangular box intersecting the line in the image and plot the signal intensity profile and measure the gray value of the peak;

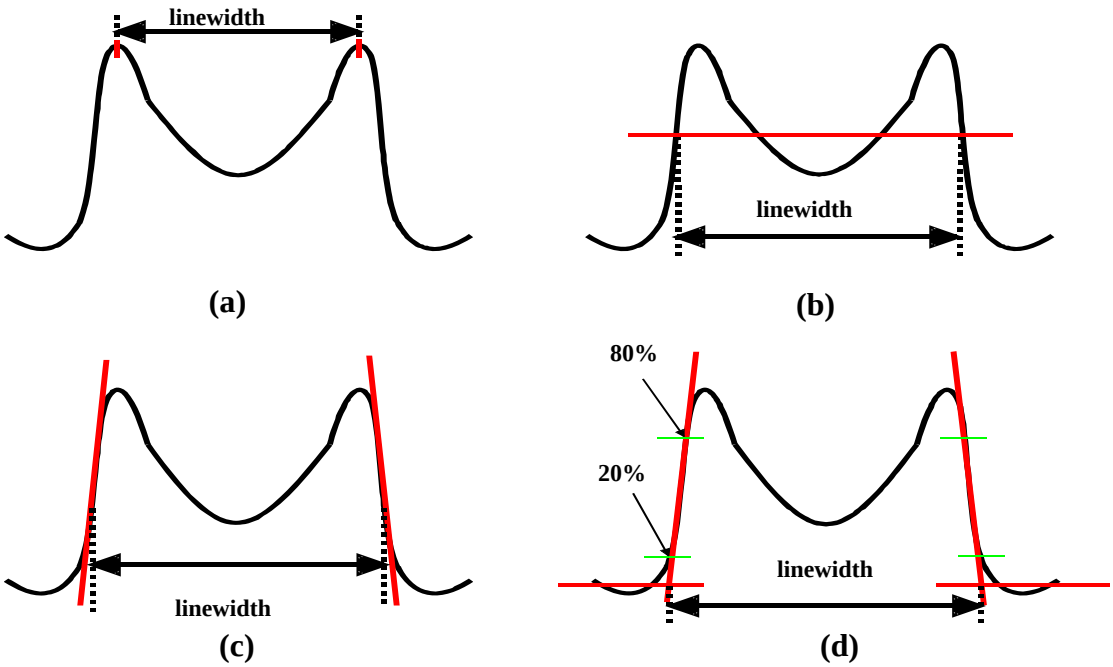

Figure 3.38 Edge Detection Algorithms

A series of schematic diagrams illustrate the common edge detection algorithms employed on CD-SEM which include (a) peak-to-peak algorithm, (b) threshold algorithm, (c) maximum slope algorithm and (d) linear regression algorithm.

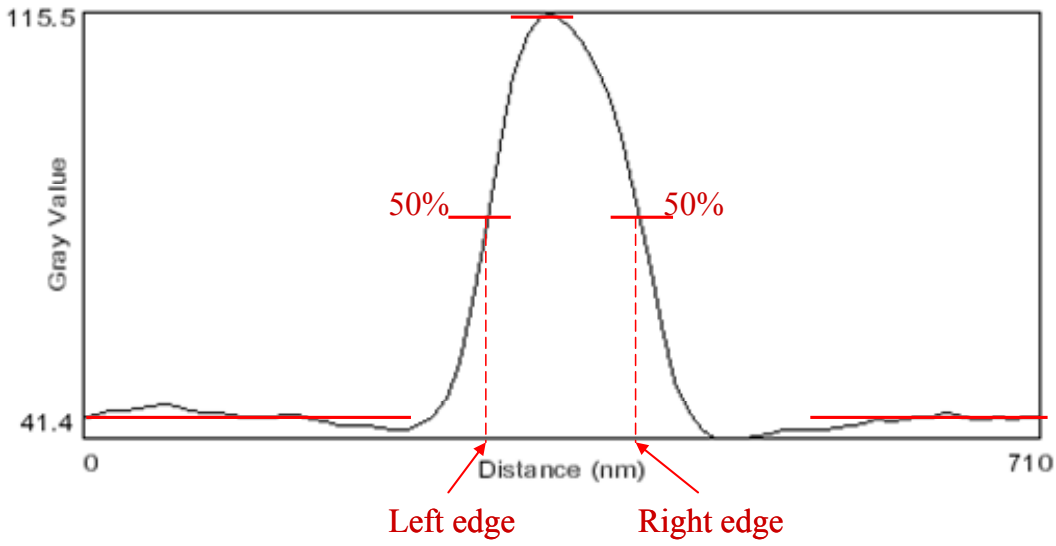

Figure 3.39 50% Threshold Algorithm

An illustration of edge determination based on the 50% threshold algorithm.

Step (2) Move the box into the left vicinity background and measure the mean gray value;

Step (3) calculate the mean gray values of the peak and left vicinity background and obtain the position of the pixel (i.e. the position of the left edge) with the closest gray level to the average level;

Step (4) Repeat Steps (2) and (3) to find the position of the right edge:

Step (5) Measure the distance between the left and right edges, which is the line width.

The line width measurements were carried out on all the lines deposited under 5, 10, 20 and 30 keV. For each line six spots were selected and Spots 1 through 3 were on the Si substrate and Spots 4 through 6 were on the Si_3N_4 thin film. The mean linewidths for Spots 1 through 3 and Spots 4 through 6 were calculated. The data is shown in Table 3.3. Then these mean linewidths were imported into JMP^{TM}, a statistical analysis software developed by SAS Institute Inc. and a Matched Pairs t-Test was conducted for the linewidths on the Si substrate and Si_3N_4 thin film. The result is illustrated in Figure 3.40. In the Paired t-Test plot the mean difference is shown as the horizontal line, with the 95% confidence interval above and below. The horizontal line at zero falls into the confidence region, which suggests that the means are not significantly different at the 0.05 level.

The result seems to tell us that neither BSE nor SE are the dominant particles for EBID reaction since neither of the scenarios we have proposed has been observed. However, once again the electron-solid interaction transition from substrate material to deposited material can help us understand what was happening.

On the Si_3N_4 thin film PE only generated SEI and these SEI dissociated the adsorbate on the surface. The nucleation started and a thin line of W was laid on the beam impact area. Immediately additional electrons started to escape from the sidewall of the

Difference: SiN-Si

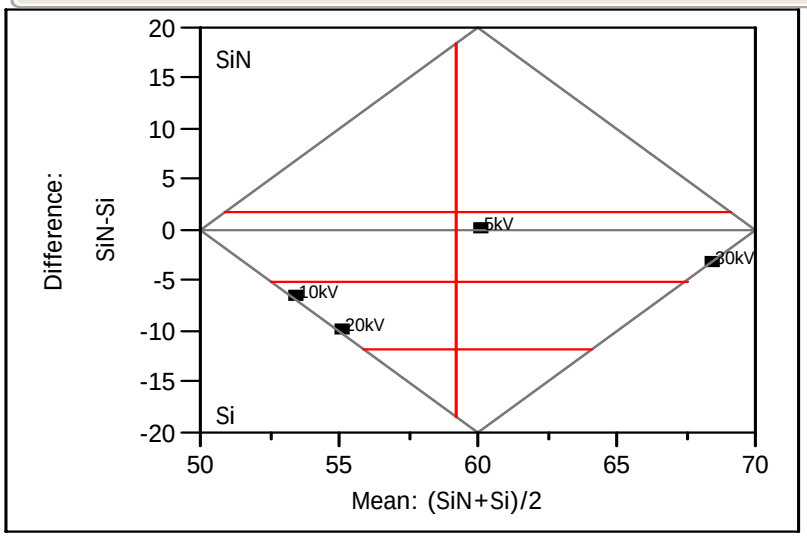

SiN	56.675	t-Ratio	-2.31911
Si	61.675	DF	3
Mean Difference	-5	Prob > |t|	0.1032
Std Error	2.156	Prob > t	0.9484
Upper95%	1.86135	Prob < t	0.0516
Lower95%	-11.861		
N	4		
Correlation	0.86463		

Across Groups

Condition	Count	Mean Difference	Mean Mean
10kV	1	-6.7	53.35
20kV	1	-10	55
30kV	1	-3.3	68.35
5kV	1	0	60

Test Across Groups	F Ratio	Prob>F		
Mean Difference	.	.	Within Pairs	Y Axis
Mean Mean	.	.	Among Pairs	X Axis

Figure 3.40 Matched Pairs Test

A diagram of the Matched Pairs test result based on the mean linewidth on the Si bulk and Si_3N_4 thin film at 5, 10, 20 and 30 keV, which supports the null hypothesis that the two groups are not significantly different.

Table 3.3 Measured Linewidth of Different Spots on Lines Grown across Si Bulk and Si_3N_4 Thin Film at 5, 10, 20 and 30 keV and Their Means.

Condition	Linewidth on Si(nm)		Linewidth on Si_3N_4 (nm)	
5kV	spot 1	60	spot 4	60
	spot 2	60	spot 5	60
	spot 3	60	spot 6	60
	mean	60	mean	60
10kV	spot 1	60	spot 4	50
	spot 2	60	spot 5	50
	spot 3	50	spot 6	50
	mean	56.7	mean	50
20kV	spot 1	70	spot 4	50
	spot 2	60	spot 5	50
	spot 3	50	spot 6	50
	mean	60	mean	50
30kV	spot 1	70	spot 4	70
	spot 2	70	spot 5	70
	spot 3	70	spot 6	60
	mean	70	mean	66.7

thin line since the critical interaction volume was larger than the linewidth, which caused dissociation on the sidewall and the thin line started to get thicker. The electron flux from the sidewall drove the lateral growth of the deposited line until the electron flux on the sidewall was not enough to decompose effectively. Similar points were made by Silvis-Cividjian et al.[58, 104, 153, 154] and Crozier et al.[84] to explain the mechanism of lateral growth. Thus, the measured line width was also the maximum lateral size of the critical interaction volume since the critical interaction volume is designated as the contour of the electrons which can effectively dissociate the precursor molecules, which is schematically illustrated in Figure 3.41. The size of the critical interaction volume is determined by beam energy, beam current and the deposited material. Once the line width reached the size of the critical interaction volume, the lateral growth stopped and only the vertical growth continued.

On the bulk substrate PE induce both SEI and SEII on the surface but the area intensity of SEI is much stronger than SEII, as shown in Figure 3.34, even though usually the number of SEII is about three times of SEI. Thus the beam impact area has deposited material piled up faster than its vicinity area. Then the rest of the scenario is similar to that on the thin film. Electron flux emitted from the sidewall of the deposited material drove the lateral growth and eventually the lateral growth saturated as the lateral size was comparable to the critical interaction volume. Though before the critical interaction volume moved into the deposited material SEII were kept being generated from the vicinity region, the area intensity was low compared with the electron flux emitted from the sidewall. The contribution of SEII to the base growth was negligible. Because the saturation linewidth of the deposited lines is determined by the critical interaction volume and the critical interaction volume is a function of beam energy, beam current and deposited material, the saturation width should be the same for the lines on both the bulk substrate and the thin film. This explains our results quite well. The result at least successful eliminated the possibility that BSE dominate EBID growth because PE did not produce BSE on the thin film and there should be no BSE for nucleation and deposition would never happen if BSE drive the process.

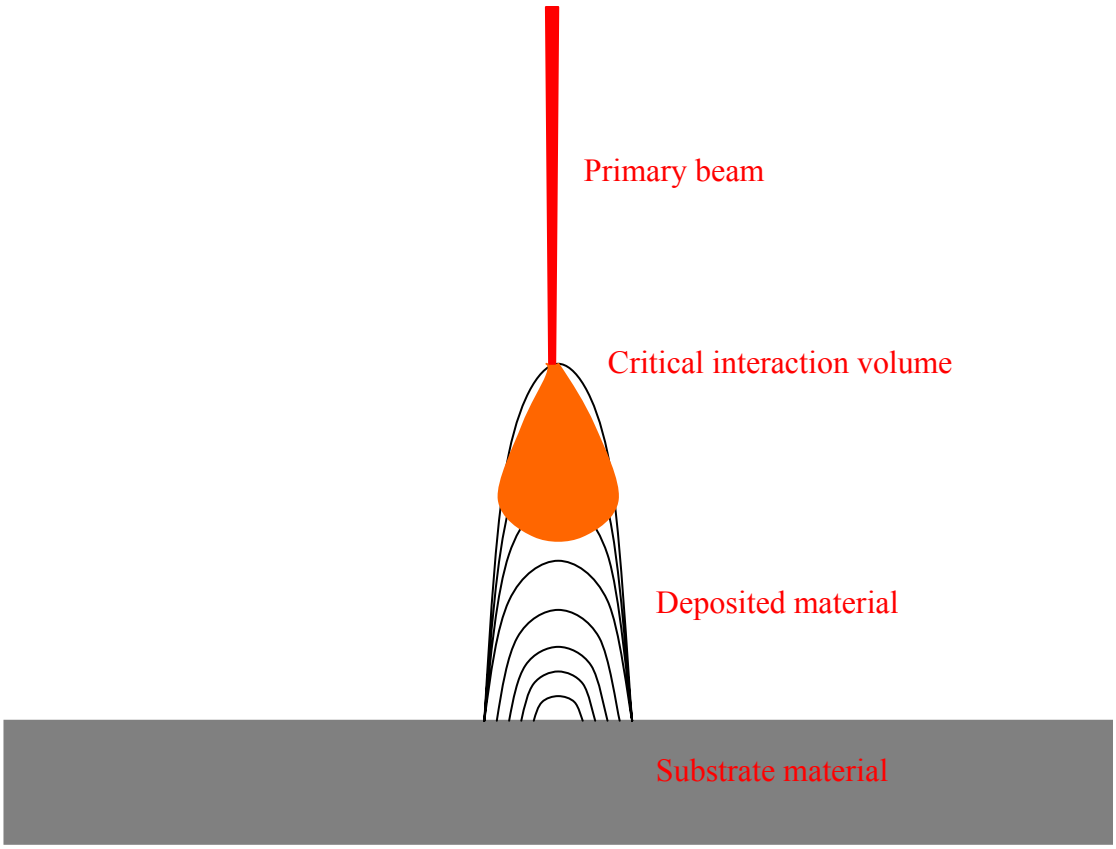

Figure 3.41 Relation between Lateral Size and Critical Interaction Volume

A schematic illustration of relation between the line width and critical interaction volume. The ultimate line width is determined by the size of the critical interaction volume.

In conclusion, the result delivers a mixed message. On one side it indicates that definitely low-energetic SE participate the reaction otherwise no deposition would happen on thin film. This is because on thin film high-energetic BSE are not produced and the only source for nucleation is SE if the deposition happens. The SE from the thin film contribute to the nucleation and after nucleation stage a blend of BSE and SE from the sidewall and top of the deposited material makes the fast growth happen. On the other side though high-energetic BSE do not dominate the reaction, it can not be excluded that BSE do not participate at all. As discussed previously, the particles from the substrate only contribute to the growth for a short time, i.e. mostly at nucleation stage and the beginning of fast growth stage, and these particles are mostly SE no matter whether the substrate is bulk or thin film. Once the critical interaction volume moves into the deposited material, the participating particles, a blend of BSE and SE, are from the deposited material. Thus, using a thin film for deposition is not suitable for investigation of the role of BSE from substrate materials.

3.4.2.5 Further Discussion

Though the designed experiments so far are not able to provide any useful data for the question whether SE or BSE dominate the EBID process, it would be interesting to investigate this problem from the perspective of contributions of SE and BSE to the growth.

Let us start from the case in which PE with energy of 1keV irradiates a silicon substrate surface that is supplied with a constant flow of WF_6 precursor gas. The probability of a deposition event occurring is then determined by the integral of the product of P(E) and σ (E) over the whole electron emission spectrum from 1keV PE. Here P(E) is the probability (or yield) of electrons with kinetic energy E which are emitted from the silicon surface bombarded with PE, through the courtesy of my colleague Yinghong Lin and as illustrated with a red curve in Figure 3.42, and σ (E) is the absolute cross sections for the electron ionization of WF_6 which was measured by a time-

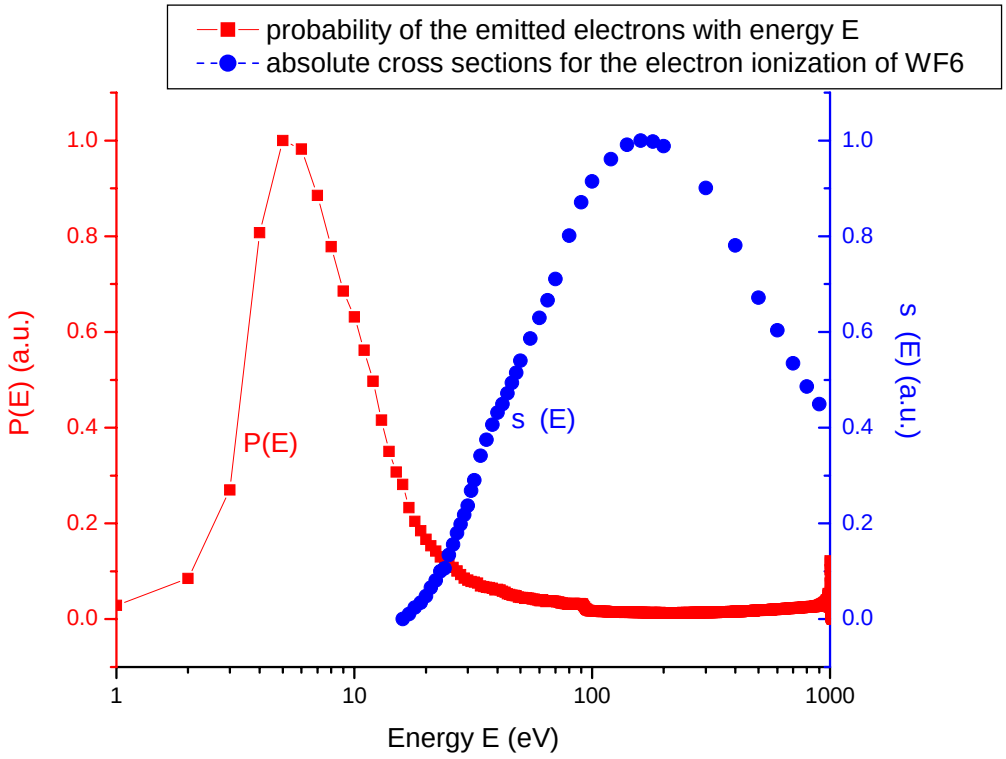

Figure 3.42 Ionization Cross-section and Emission Spectrum

A superimposition of the absolute cross section for the electro ionization of WF_6 (blue curve) over the probability distribution of the emitted electrons with energy E from a silicon surface bombarded with 1keV PE. Both curves are normalized for comparison.

of-flight mass spectrometer (TOF-MS)[122], as illustrated with a blue curve in Figure 3.42. The product of P(E) and σ (E) over the whole electron emission spectrum is illustrated in Figure 3.43. From Figure 3.43 it can been seen that the green area that stands for the SE contribution is much smaller than the blue area that stands for the BSE contribution. This indicates that during deposition the contribution from SE to ionize the precursor molecules is much smaller than that from BSE and BSE seem to dominate the growth for the case in which W deposition is made on the silicon surface under the bombardment of 1keV PE.

If this argument can stand for 1keV, for higher beam energies commonly used in EBID, the BSE contribution to the deposition should be more dominant and SE should be less contributive. This is because for most elements as primary electron energy goes up SE yield starts to increase and reaches its peak at around 10eV and then decays quickly while BSE yield continues increasing. As a consequence, for beam energy ranging from 1 to 30keV the contribution from SE to ionize the molecules is almost negligible compared with BSE.

On the other hand, as beam energy decreases from 1keV the SE yield should increase and BSE yield should decrease. This would lead to an increase in the SE contribution and a decrease in the BSE contribution until at some point the SE contribution outweighs the BSE part and becomes the dominant part.

In summary, for high energy primary electrons in keV range BSE give a much larger contribution to the deposition than SE while for low energy primary electrons around ~100eV range the SE contribution could outweigh the BSE part and becomes dominant in EBID growth.

3.5 Conclusion and future work

In this chapter, the mechanism of EBID process has been investigated from two approaches: surface science and electron-solid interaction. The control of growth rate, vertical growth, lateral growth and tip geometry has been discussed.

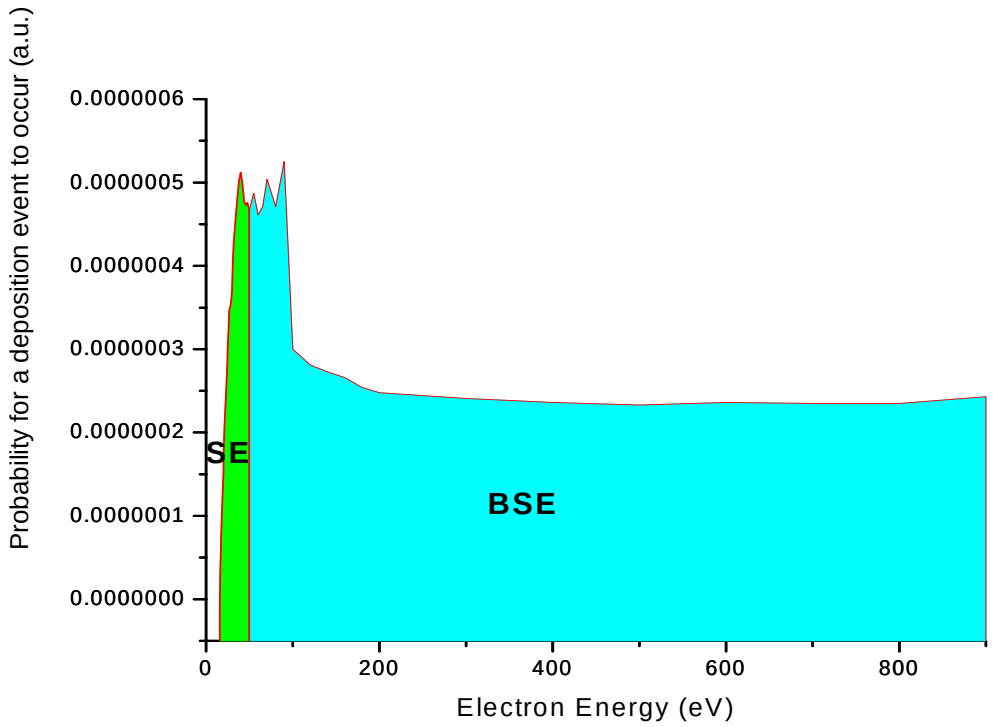

Figure 3.43 Probability Distribution for A Deposition Event

A probability distribution for a deposition event to occur over the emission electron spectrum from a silicon surface bombarded by 1keV PE. The probability is calculated from the product of P(E) and σ (E) in Figure 3.42.

From the perspective of surface science, experiments were performed to study the influence of substrate temperature on EBID process. The observation that the temperature dependence of growth rate follows an Arrehnius relationship provided proof for the statement that EBID reaction involves adsorption-desorption process and is a process on substrate surface instead of gas phase. ESD was found to play an important role in providing energy for adsorbed species to desorb from the surface. Electron scattering within a tip and surface diffusion determine the size and geometry of the tip.

From the perspective of electron-solid interaction, experiments were performed to study the influence of SE and BSE on EBID process. Suppressing SE by giving the substrate positive biases was not successful because of its feasibility. Variations of SE yield by controlling beam energy, substrate material and tilt angle showed no significant correlation with the growth rate of EBID process. Time-resolved sample current measurements suggested EBID growth consists of two phases. The first phase involves both electron-substrate interaction and electron-deposit interaction and the interaction volume transits from the substrate material to the deposited material. The geometry and maximum width of the tip are determined at the end of this phase. The second phase involves only electron-deposit interaction and the interaction volume resides within the conical top of the tip during the second phase. In the second phase the geometry of the conical top and the width of the tip are not changing any more and the only growth is the vertical growth. The contribution of SE to EBID process is still not able to be determined yet based on these experiments. On the other side lines were deposited across a thin film and bulk substrate and they were found to have identical width on both the thin film and the bulk substrate. This experiment was not able to screen BSE during deposition because the second phase of EBID growth took over the first phase very quickly and in second phase the growth had nothing to do with substrate. Thus neither can any conclusion be made for the influence of BSE on EBID growth.

However, the ionization cross section data for WF_6 and the emission energy spectrum from a silicon surface bombarded by a 1keV PE allow us to estimate the contributions of BSE and SE to the deposition. The estimate suggests that for high energy

primary electrons in keV range BSE give a much larger contribution to the deposition than SE while for low energy primary electrons around ~100eV range the SE contribution could outweigh the BSE part and becomes dominant in EBID growth.

Though a lot of work has been done to investigate the deposition from the perspective of electron-solid interaction, the mass transport involved in the process is not clear. The related questions include how the gas flux is distributed in the space after being ejected from the nozzle, what bonding forms between the precursor molecules and the substrate, and what role adsorption-desorption process and surface diffusion play in the mass transport. All these need to be studied to give a better understanding of the deposition.

Chapter 4 Characterization of the deposited materials

4.1 Literature review

As introduced in Chapter 1, EBID can be applied to a broad range of areas, such as mask repair, nanostructure circuit, attachment of carbon nanotube, wiring biomolecules and tip fabrication for AFM. All these applications require deposited materials have some expected properties. For instance, the materials for EUV mask repair need to be of high purity so that EUV light can be absorbed. The materials for nanostructure circuit and wiring biomolecules need to be highly conductive. The materials for attachment of carbon nanotube and tip fabrication for AFM need to have good mechanical properties. Thus it is important to investigate the chemical composition, microstructure, electrical property and mechanical property of deposited materials.

Experiments have been performed to investigate the characterization of the deposited materials and the influence of experimental conditions on the characterization. such as chemical composition[22, 32, 40-43, 47, 50-52, 61, 62, 66, 67, 103, 155-163], microstructure[18, 37, 40, 42, 44-48, 50-52, 60, 68, 123, 131, 156, 160, 164-178], electrical property[15, 16, 23, 26, 28, 37, 39-45, 47, 68, 70, 179-183], density[184-186], mechanical property[187-190] and magnetic property[160, 170].

4.1.1 Chemical composition

Chemical composition has always been the focus of the attentions since it determines many functional aspects of the deposited materials. Auger electron spectroscopy (AES), x-ray microanalysis (XMA) and electron energy loss spectroscopy (EELS) have been employed to perform the study on chemical composition of deposited materials. The general discovery was that the deposited materials contain metal content and ligand from the precursors as well as carbon content from the residue gas in the chamber. It has been widely reported that the metal contents could be increased by increasing beam current[40, 42, 47, 50, 52], decreasing beam energy[40, 51] and

increasing substrate temperature[32, 50, 67]. The ligand clusters remaining in the deposited materials could be reduced exponentially with exposure time[62]. The carbon content could be decreased by increasing beam current[50]. However, opposite observations were made that no significant composition change was found on varying beam current and beam energy[42, 156, 157].

4.1.2 Microstructure

Microstructure of the deposited materials has been attracting a lot of attention because it has a big impact on physical properties of the deposits. The two major investigation tools for this purpose are transmission electron microscope (TEM) and scanning transmission electron microscope (STEM). These TEM and STEM images illustrate that the deposited materials have a structure with nanocrystals dispersed in an amorphous matrix[18, 40, 42, 44-48, 52, 68, 123, 131, 156, 164-172, 178, 191], which indicate a poor conductivity and tensile strength. This structure can be improved by increasing beam current, increasing beam dwell time, increasing beam energy, post-deposition heat treatment and post-deposition electron irradiation. Kretz et al.[46] reported that a high beam current gave a closer packing of crystallites and an increasing beam dwell time led to an increase of the crystallite size. Weber et al.[50, 51] discovered similar results under high beam currents. Xie et al.[171] increased the crystallinity of as-fabricated nanorods by increasing beam energy. Moreover, surprising results came from the experiment in which a continuous polycrystalline wire was transformed from nanocrystals dispersed in amorphous matrix by post-deposition electron irradiation[178] and the experiment in which single crystalline phase was transformed from as-formed nanorods by post-deposition heat treatment[160, 173].

4.1.3 Electrical properties

Resistivity is another hot spot in which people have put lots of efforts because it has a direct impact on the functionality of many nano-devices fabricated by EBID. Resistances of deposited materials were measured by either pre- fabricated micro-

electrodes on a wafer or nano-probe manipulator and the methodologies include two-terminal measurement in which the same pair of terminals sweep the source and collect the signal and high-precision four-terminal measurement in which the outer pair of terminals sweep the source (current) and the inner pair collect the signal (voltage). The common result is that the deposited materials have a resistivity of several orders higher than the bulk materials. The problem was improved by increasing beam current or exposure time[37, 39, 41, 42, 44, 45, 47, 192], plasma cleaning of the chamber and sample[41], increasing substrate temperature[68], decreasing scan speed[68], and post-fabrication annealing[45, 165, 182]. On the other hand, there exist very different results and thus disagreements on aspects such as conducting mechanism and methodology. Koops et al.[47] reported that the resistivity of the deposited materials demonstrated Ohmic characteristic (independent of temperature) due to high metal content while Schossler et al.[45] found Schottky resistivity characteristic (dependent on temperature) in the deposits due to low metal content. Croitoru et al.[181] measured the resistance of a deposited line and found that the result by two-point measurement was about two orders higher than that by four-point measurement, which indicated the contact resistance was dominant. However, Rotkina et al.[182] fabricated Pt/C nanowires by EBID and found the resistance to be the same in both two-point measurement and four-point measurement, which indicates an independence of contact resistance.

4.1.4 Mass density

Few papers have been published on mass density measurement of the deposited materials because the ultra-light weight, in femtogram range, of the nanostructures made direct measurement difficult. The only available way to determine mass of nanostructures is by measuring resonance frequency shift of a micro-cantilever on which new materials were deposited or from which deposited materials were removed. Nishio et al.[184] found out that the mass density of the deposit increases with beam energy and beam current. Utke et al.[186] reported that the ratio of impinging electrons to deposited atoms, beam heating and thermal stability of the precursor molecules determine the density of the deposited materials.

4.1.5 Mechanical properties

In recent two years an interest has risen in mechanical properties of the deposited materials as EBID began to be used for attachment of carbon nanotubes or mask repair. Ding et al.[187] employed an AFM with a nano-indenter mounted to measure the hardness and elastic modulus of a deposited sample and revealed a slight increase of hardness and modulus for increasing beam energy. Li et al.[189] analyzed the stress distribution of nanotube clamps formed by the EBID technique and examined the contributing factors, including nanotube position, stiffness of clamp material, and thickness of the clamping pad between the AFM tip and the nanotube. Okada et al.[188] presented an experiment in which a piezo-driven cantilever was used to deflect a freestanding nano-pillar and the Young's modulus of the nano-pillar was measured from the deflection. Utke et al.[190] demonstrated an in-situ nano-manipulation set-up for tensile strength measurements using a cantilever-based force sensor.

4.1.6 Magnetic properties

Recently some Japanese scientists started to investigate the magnetic properties of the deposited materials because of the potential of applications in ultra-high density magnetic recording and nanometer-sized magnetic devices. Che et al.[170] fabricated FePt nano-rods by flowing Fe and Pt precursors simultaneously followed by post-deposition annealing and off-axis electron holograms indicated that the resulting nano-rods had a strong ferromagnetic characteristic. Takeguchi et al.[160] performed post-deposition heat treatment to crystallize iron nano-rods and electron holograms after magnetization showed that the residual magnetic flux densities of the nano-rods were similar to iron micro-powders.

4.2 Investigation of resistivity

4.2.1 Introduction

As its increasing applications in the field of mask repair and circuit repair, it is urgent to investigate the resistivity of the materials deposited via EBID. In this section, an experimental approach for resistivity measurement will be described and the results will be demonstrated and discussed.

The experimental approach includes preparing a four-point measurement circuit which will be detailed in Section 4.2.2, depositing nanowires on the circuit and measuring I-V curve for the nanowires on a probe station, both of which will be described in Section 4.2.3.

4.2.2 Fabrication of four-point measurement circuits

The fabrication process for four-point measurement circuits adopted in this work is similar to the manufacturing process in semiconductor industry. It follows a series of steps which include spin-coating of resist, pattern transfer through electron beam lithography, resist development, metal deposition by PVD and lift-off and are illustrated in Figure 4.1.

Because electrodes would be made on a silicon substrate and no leakage currents are expected to flow between the electrodes through the silicon substrate, the substrate surface should be covered by a non-conducting layer such as oxide or nitride. In this study a 4-inch Boron-doped Si (100) wafer with an oxide layer grown on the surface was obtained from Silicon Quest International. The resistivity of the n-type silicon wafer is 10~20 Ω·cm and a 500nm oxide layer was thermally grown on the surface because of its great dielectric strength of up to 15×10^{6}V/cm depending on the thickness. The thickness of oxide film was chosen as 500nm so that it would be hard enough to prevent penetration of sharp probes which would be used later in the resistance measurement.

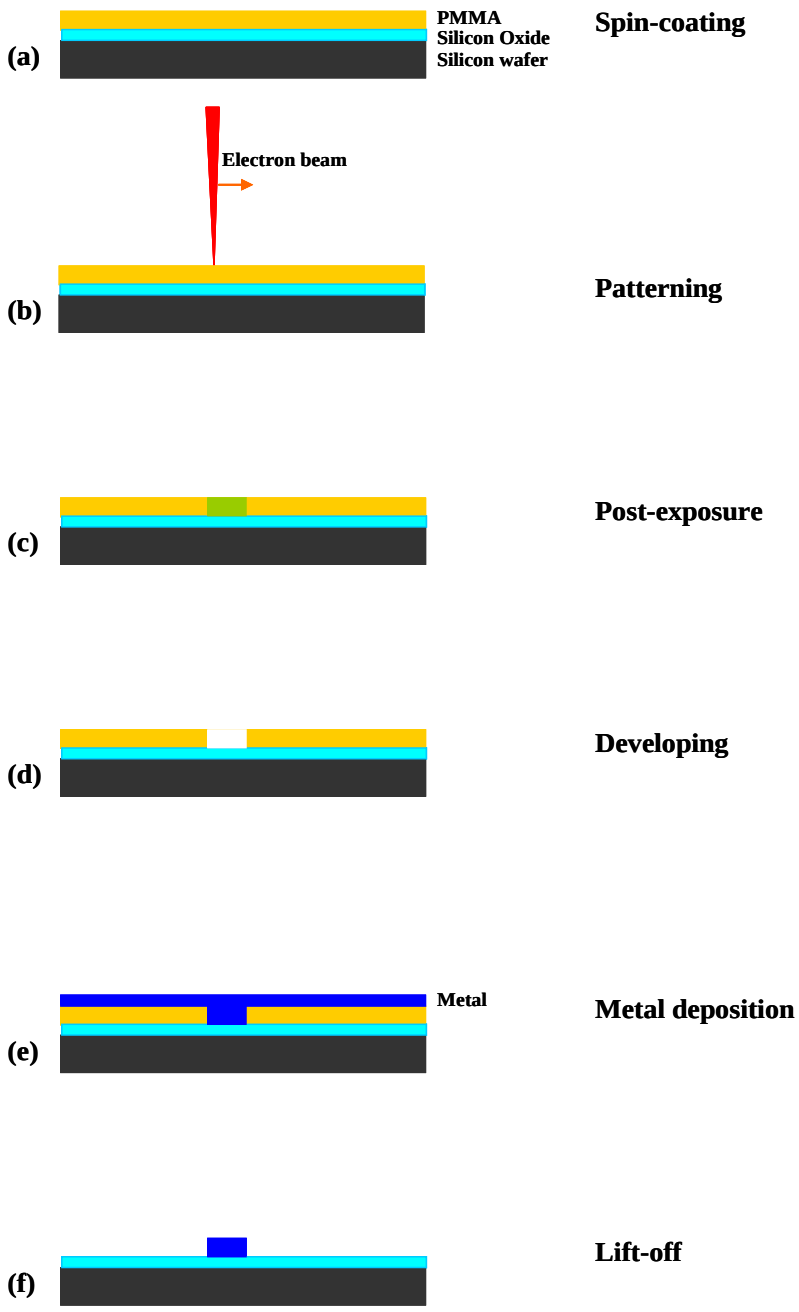

Figure 4.1 Fabrication Process for Four-point Measurement Circuit

A schematic diagram of fabrication process for a four-point circuit. (a) spin-coating PMMA on a silicon wafer covered with an oxide layer; (b) pattern transferring by electron beam lithography; (c) forming pattern area with larger solubility after exposure; (d) developing the patterned resist; (e) depositing metal layer on the wafer and (f) lifting off the resist and leaving the metal pattern on the wafer.

The next step was to spin-coat e-beam resist on the wafer. Based on resist chemistry the common e-beam resists off the shelf can be divided into two categories, positive (removed where exposed) and negative (retained where exposed). In this work, polymethyl methacrylate (PMMA), a positive resist, was selected because metaldeposition would be made afterwards to form electrodes on the exposed area and was purchased from MicroChem Corp. in a high molecular weight form (495K). The e-beam resist was made by mixing 5% PMMA and 95% anisole which is a casting solvent and was poured onto the wafer surface. The wafer was spun on a Brewer Science CEE Model 100 Spin Coater at 1800~1900 rpm for 70 seconds and then baked on a hotplate at 180^{o} C for 70~90 seconds. The resulting resist thickness was measured to be about 120nm by Filmetrics F20-UV Thin Film Analyzer.

Then the wafer was sent for pattern transfer by e-beam lithography which uses a beam of electrons to generate patterns on a surface. The pattern was designed with L-Edit, a CAD program from Tanner Research, Inc. The design contains four 50μm×50μm square pads placed at four corners of a larger square area and one electrode extends from each square pad into the center of the larger square area and forms a tapered terminal of 500nm wide. These terminals are then aligned parallel to each other with a spacing of 1000nm wide. The pattern was later transferred to e-beam lithography system in the standard intermediate format GDSII and converted to the machine-specific format. The e-beam lithography system employed in this study is JEOL JBX 6000FS-E Gaussian vector scan system, as shown in Figure 4.2, with a thermal field emitter running at 25 or 50kV. The system can be operated under two modes: the 4^{th} lens-mode which enables to form an electron beam spot as small as tens of nanometers for efficient submicron writing and the 5^{th} lens-mode which can reduce the beam size down to 5nm and allows nanometer writing. The workpiece stage can hold a wafer of up to 8-inch diameter and its movement is step and repeat. Stage position is controlled in units of 0.62nm by a laser interferometer. In this work the wafer was exposed by an electron beam with energy of 50kV and current of 1nA and with doses of 500μC/cm^2. The pattern was repeated to form a set of 5 by 5 and a number of sets were made on the wafer.

Figure 4.2 Electron Beam Lithography System

A digital photograph of JEOL JBX 6000FS-E Gaussian vector scan e-beam lithography system with a thermal field emitter.

In order to allow metal to form contacts and interconnects on the patterned area, a step called resist development was performed to remove the irradiated resist from the wafer and form open areas in the resist film. The developing solvent contained methyl isobutyl ketone (MIBK) and isopropanol (IPA) and the ratio of MIBK to IPA is 1:3. The wafer was immersed in the solvent for 60 seconds and then taken out to be rinsed in IPA for 40 seconds. After rinsing the wafer was blown dry with nitrogen.

Metal deposition was made in a physical vapor deposition (PVD) system from Cooke Vacuum Products, Inc. The PVD system employs a tungsten boat to resistively heat the target metal to evaporate and then deposit onto the substrate mounted over thetungsten boat. Gold (99.999% pure, Alfa Aesar, Ward Hill, MA, USA) was selected as the target metal here due to its excellent conductivity. Since gold cannot stay on Si surface firmly and would be washed away during the subsequent lift-off step, chromium (99.95% pure, Kurt J. Lesker, Clairton, PA, USA) was chosen as an adhesive between Si substrate and gold film. During deposition a vacuum of ~10^{-4} Pa was created and the tungsten boat was heated above approximately 250ºC. Average thickness and deposition rate were monitored for each film using a water-cooled quartz crystal microbalance (QCM, from Maxtek, Inc.) mounted adjacent to the sample. Nominal metal thickness and deposition rate were 5nm and 0.2 Å/sec, respectively, for chromium. Gold was deposited at 1.0 Å/sec to a nominal thickness of 40 nm.

The last step was metal lift-off which lifts off any metal deposit onto the resist leaving metal only in the open areas of the resist film. The wafer was placed in a container filled with acetone for hours until the unwanted metal film was peeled off. Slight agitation of the container was used to help lift off the metal. When the lift-off was completed the wafer was rinsed in IPA for degreasing and then blown dry with nitrogen.

The four-point measurement circuits which were fabricated through all the steps mentioned above are demonstrated in Figure 4.3.

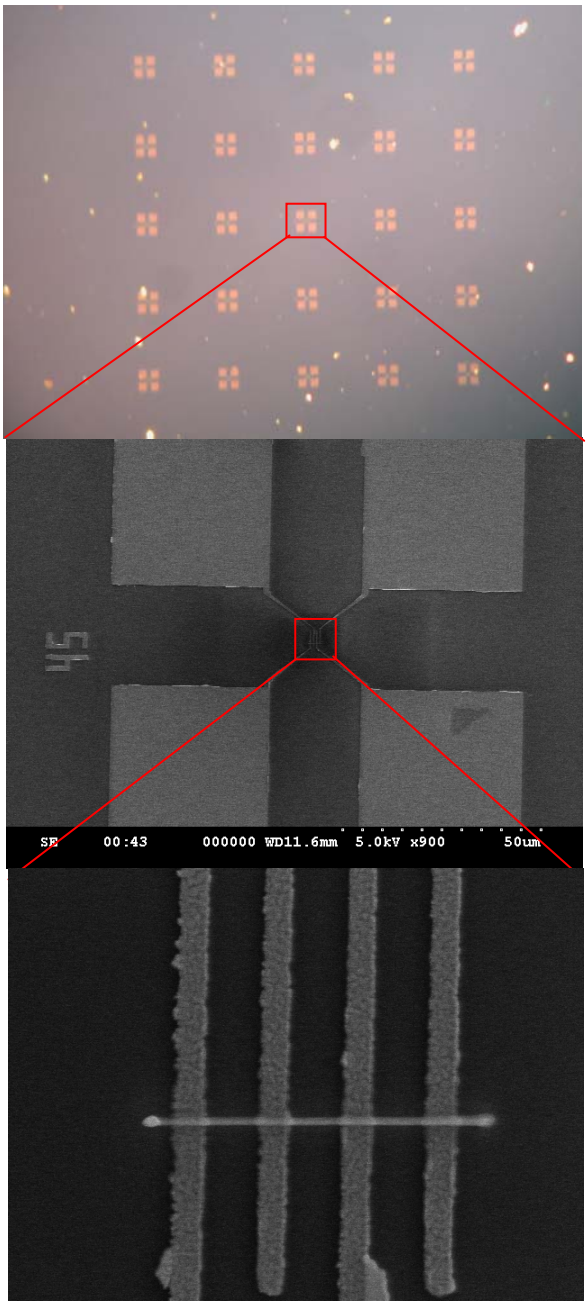

Figure 4.3 Prototype of Four-point Measurement Circuit

Optical and electron micrographs of the four-point measurement circuits fabricated in this study.

4.2.3 Experiment and measurement

The motivation for the experiment which will be described as follows was to examine the feasibility to use the four-point measurement circuits mentioned above to measure resistances of nanowires made by EBID. Also a simple resistivity comparison will be made with respect to beam scan speed.

The experiment was conducted on Hitachi S-4300SE/N VPSEM at 25ºC and the precursor gas was WF_6. The chamber pressure during deposition was kept at 7.5×10^{-3} Pa. The beam energy was set at 5kV and the beam current was measured to be 283pA by a Faraday cup. The beam scan mode was set in line analysis mode so that a tungsten nanowire could be made across the four electrodes of the four-point measurement circuit. The scan speeds provided by the SEM are 16.7ms, 50ms, 11s, 44s, 131s and 262s per line.

However at the last four scan speeds the beam was moving too slow to make a uniform or even continuous nanowire. Therefore only the first two, 16.7 and 50ms/line, were selected for this study. Replica was made for each scan speed and the order for the runs was randomized. Two nanowires were made on the circuits 13 and 23 at scan speed of 50ms/line and two on the circuits 43 and 53 at scan speed of 16.7ms/line. In the following paragraphs, these nanowires will be called Samples 13, 23, 43 and 53, for convenience. All the nanowires were deposited at the magnification of ×20,000 and for 15~20 minutes. Sample 23 is illustrated in Figure 4.4, showing a typical SEM image of the nanowires.

A trick was deployed to make line deposition on the silicon oxide layer possible. Silicon oxide is a well-known insulator and when it exists as a thin film on a conducting substrate, the anomalous secondary electron emission from the oxide layer causes a positive charging-up of the oxide layer. This charging-up leads to a deflection of electron beam and the extend of beam deflection depends on surface potential of charging patterns[193]. In this experiment charging induced electron beam deflection was up to a few microns in less than one minute. In order to mitigate the beam shift problem from

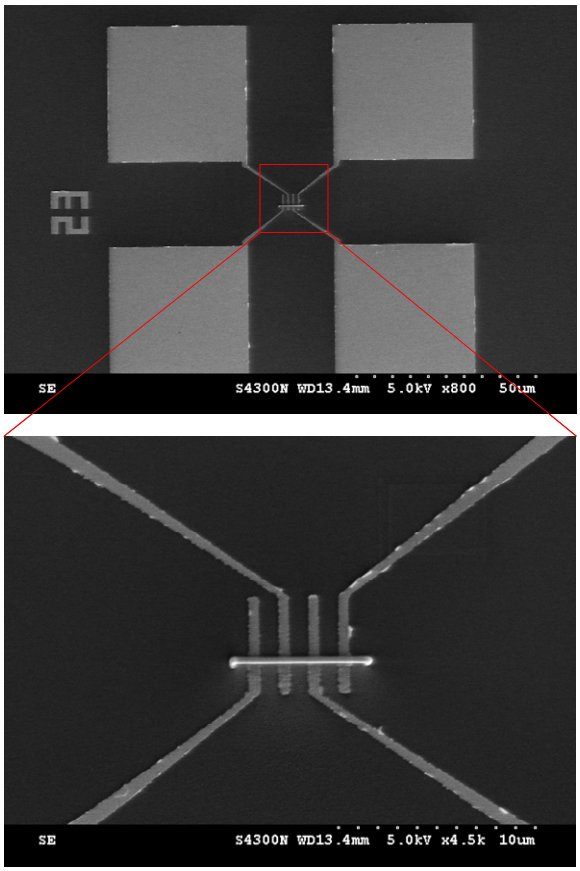

Figure 4.4 Nanowire on Four-point Measurement Circuit

Electron micrographs of nanowire deposited on a four-point measurement circuit.

surface charging, an aluminum foil was used to cover the wafer surface and small openings were cut on the foil to expose the four-point measurement circuits. This effectively limited the field lines to a short range going from the beam spot to the surrounding aluminum foil instead of a long range going from the irradiation spot to the grounded chamber wall. When the incoming electrons travel from the column to the wafer, they do not feel the field until they are very close to the wafer and thus the beam deflection is significantly reduced.

The resistance measurement was carried out on a Signatone CheckMate 210 Probe Station which is loaded with a Motic PSM-1000 ProbeScope and four Signatone S-926 Micropositioners, as shown in Figure 4.5. The CheckMate 210 Probe Station is an ultra-stable 200mm/300mm analytical probe station with coarse and fine wafer stage movement to provide fast wafer movement as well as submicron resolution. The PSM-1000 ProbeScope is equipped with objective lenses with magnification of ×2, ×10 and ×20. The S-926 Micropositioner is designed for small geometry probing down to approximately one micron and is tightly fixed on the probe station by vacuum when in use. The head has a pivot assembly which allows the probe tip holder to be quickly positioned in Z direction before the fine adjustment for final touchdown. At the end of the probe tip holder of each Micropositioner is mounted a Signatone SM-35 tungsten probe tip which has a 500μm-diameter shank and a 0.7μm-diameter tip. The four Micropositioners are electrically connected to a Keithley 2400 Sourcemeter which is controlled by a LabTracer2.0 test integration software. In this study the sourcemeter was set in four-wire sensing mode because this allows four-point measurement and the contact resistances between the probe tips and the sample cancel out. In four-wire sensing mode the current was set as the source in the range 1μA and the programming resolution was 50pA and the voltage was set as the measurement.

In order to measure the resistance, the four probe tips were individually placed on the four conducting pads of the four-point measurement circuit. In four-wire sensing mode the source current was swept in 300 steps from -1μA to 1μA between the two outer electrodes and the voltage feedback was measured between the two inner electrodes.

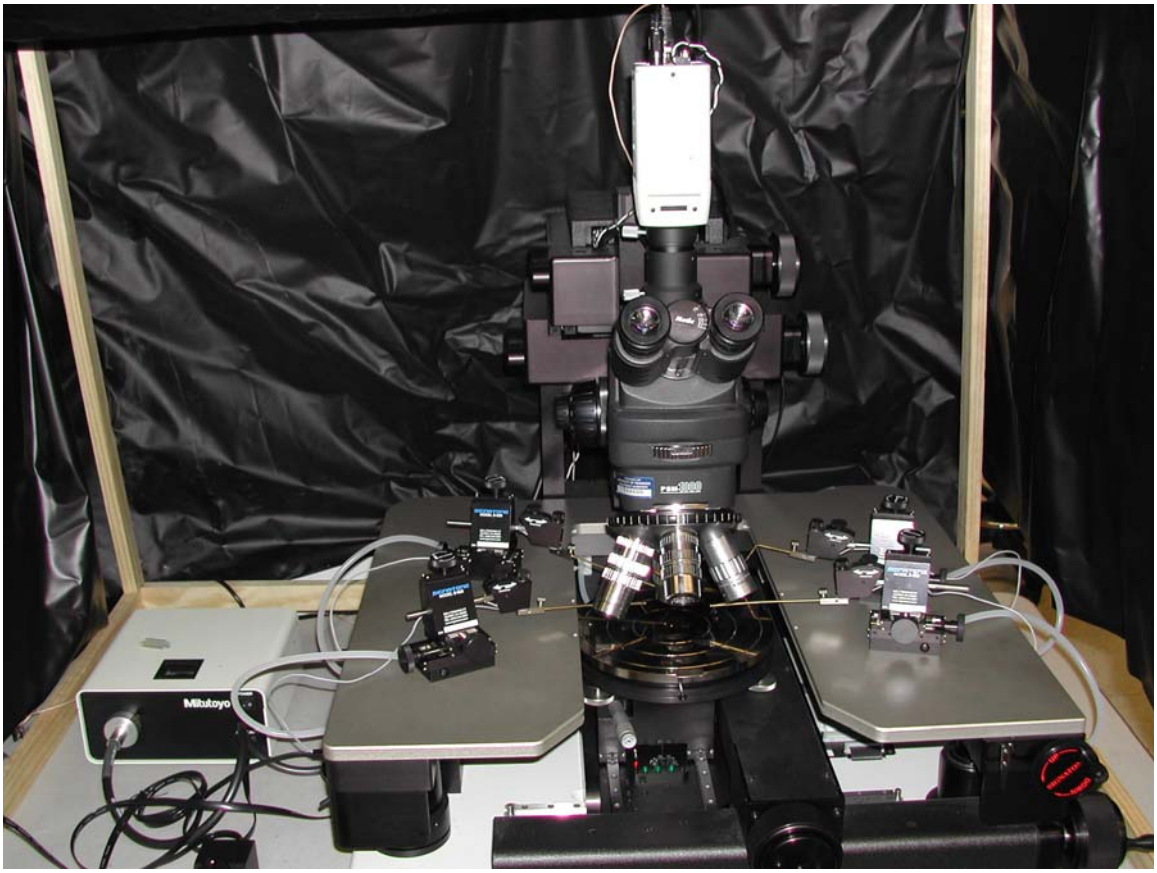

Figure 4.5 Four-point Probe Station

A digital photograph of Signatone CheckMate 210 Probe Station loaded with a Motic PSM-1000 ProbeScope and four Signatone S-926 Micropositioners.

Only Samples 23 and 43 generated data as expected, while Sample 13 failed to generate useful information and Sample 53 was burnt due to overload. The data was recorded and the I-V curves were plotted in Figure 4.6. The data are symmetrically distributed around the origin in a linear fashion. The resistances estimated from the I-V curves are about 1.22 and 5.67MΩ for Samples 23 and 43 respectively.

In order to estimate the resistivity, the dimensions of the nanowires need to be measured. In four-point measurement, the voltages were measured between the two inner electrodes and thus only the length between these two electrodes should be considered. The SEM images indicates the length and the width of both Samples 23 and 43 were 1000nm and 320nm respectively. The 3D and cross-section profiles of both nanowires, as presented in Figure 4.7, were measured on a MFP-3D atomic force microscope (AFM) from Asylum Research. The cross-section profiles indicated that the height of Sample 23 was approximately 350nm and the nominal height of Sample 43 was 450nm. Thus, based on the resistance and dimensions, the resistivity for Samples 23 and 43 were estimated to be 0.136 and 0.815Ω·m.

4.2.4 Discussion

Koops et al.[85] discovered that the deposits with resistance ranging from hundreds ohms to giga ohms by varying beam current and beam voltage, which indicated the deposited materials could behave like a conductor, or semiconductor, or even insulator. This discovery is significant because it gives a possibility in nanofabrication to build all conducting, semiconducting and insulating components by using one precursor and properly controlling system parameters. The estimated resistivities of the nanowires in this study are about 100,000× of magnitude larger than that of bulk tungsten which is 56nΩ·m at 20ºC and the values fall into the range of semiconducting materials which is approximately between 10^{-2} and 10^{9}Ω·m[194]. Similar large resistivity at room temperature was reported elsewhere[37, 45, 192].

The reason why the resistivity was enormously large is not clear. Many other

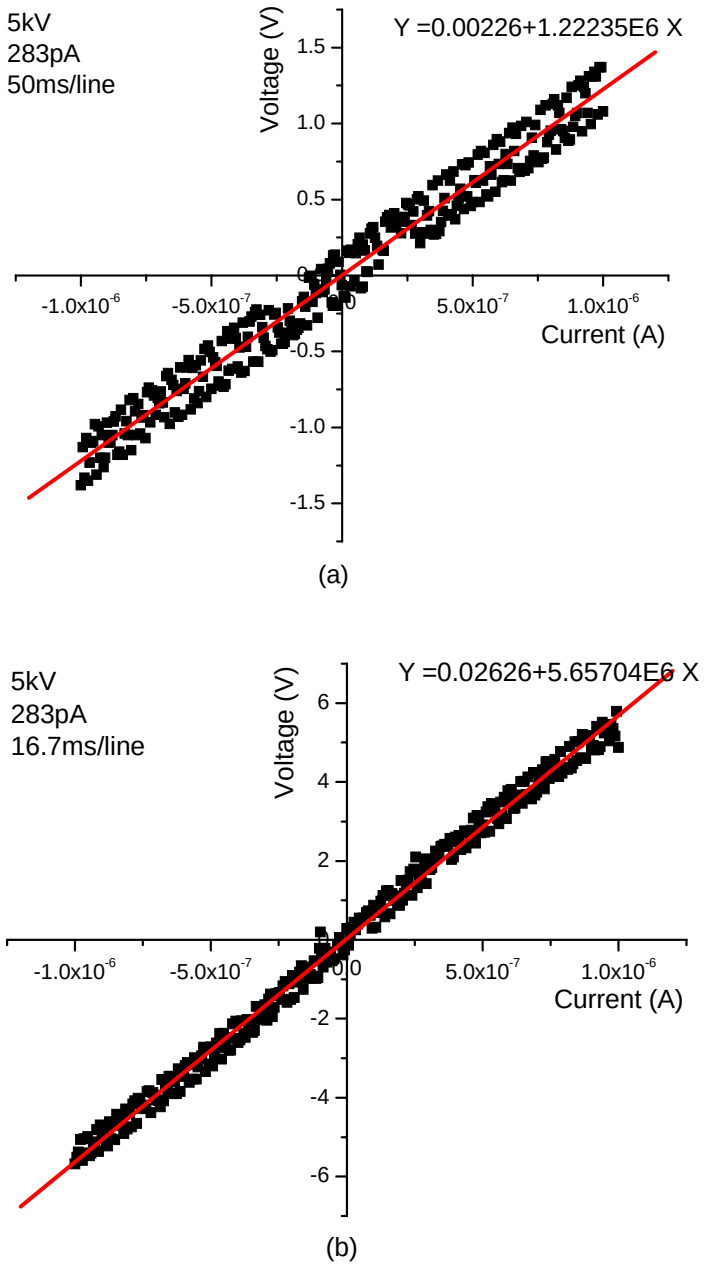

Figure 4.6 I-V Measurements

A series of I-V curves were measured from the four-point measurement circuit pre-fabricated on a silicon wafer with an oxide layer and the sample was a nanowire grown by a 5kv beam with current of 283pA at scan speeds of (a) 50 and (b) 16.7ms/line. The resistances were estimated to be 1.22 and 5.67MΩ for (a) and (b) respectively.

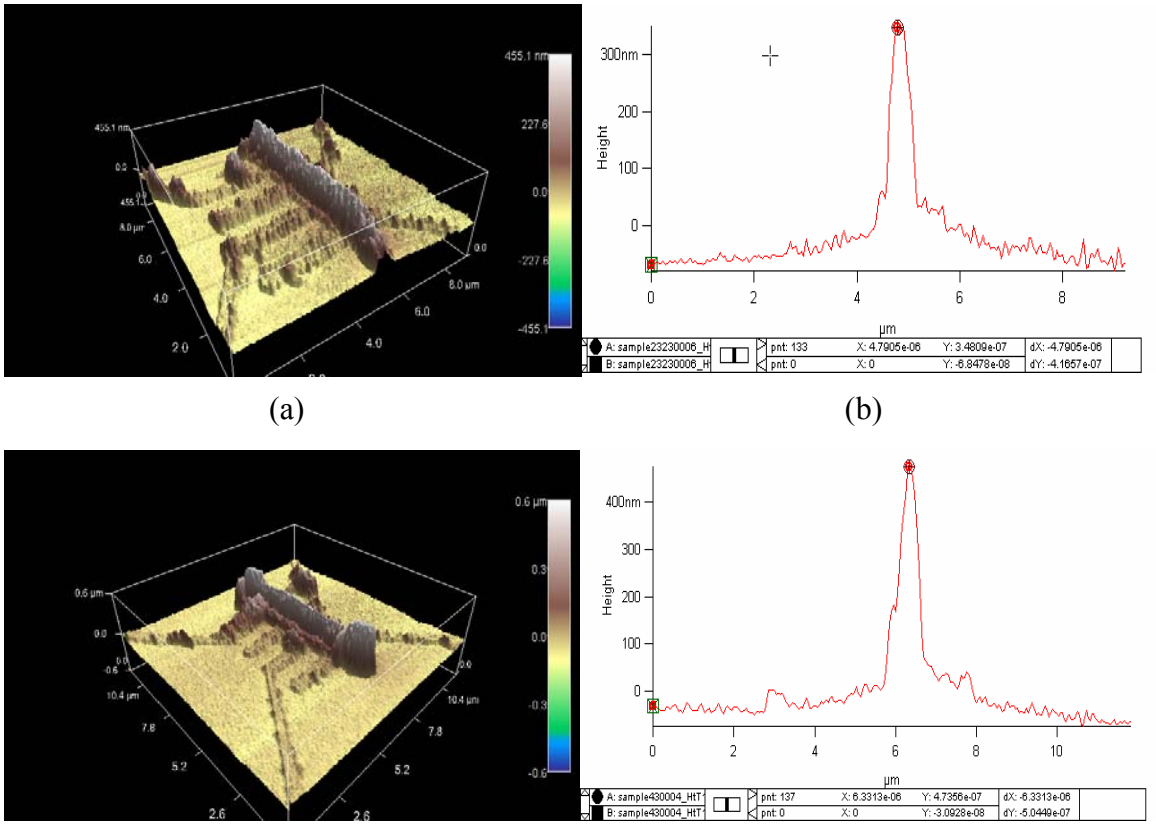

(a) (b)

(c) (d)

Figure 4.7 AFM Measurements

A set of AFM measurements for Samples 23 and 43. (a) 3-D image for Sample 23, (b) cross-section profile for Sample 23, (c) 3-D image for Sample 43 and (b) cross-section profile for Sample 43.

groups reported that this poor conductivity was associated with the microstructure which showed lots of nanocrystals embedded in an amorphous carbon matrix. In that case hopping conduction[67, 195, 196] was proposed to explain that the high resistivity was caused by energy barrier which electrons had to overcome to hop from one site to another. This conduction mechanism was supported by the negative temperature coefficient of the resistivity measured from the deposited materials[67]. However, in those studies the precursors were carbon-based or hydrocarbon-based while in this work the precursor was WF_6 which is carbon-free. Though the possibility that carbon might come from the backflow of pump oil into the vacuum chamber or hydrocarbon contaminants adsorbed on the wafer exists, the amount of carbon in the deposited materials was supposed to be neglected compared with a much higher gas flux of WF_6. A TEM microstructure study of the deposited materials is then necessary to find out the cause of the poor conductivity in this work. If the microstructure shows amorphous carbon matrix containing W nanocrystals, a further investigation is required to find out the source of carbon and how to remove it. If the microstructure shows high-purity W, then our resistance measurement was erroneous and an investigation must be conducted to determine the cause. Thus the microstructure study is highly suggested to the future work.

Another observation found in this work was that the resistivity of the material formed at low scan speed was higher than the material deposited at high scan speed. This is consistent with the results published elsewhere. The explanation is that at low scan speed the electron beam dwelled at each spot longer than at high scan speed. A longer beam dwell time allowed the intermediate products like tungsten subfluorides to go through further decomposition so that less impurity stayed in the deposited.

4.3 Conclusion and future work

A four-point measurement circuit was fabricated to measure the resistance of the deposited materials and was proved a reliable device for resistance measurement. The measured resistivity was in semiconductor range and about 100,000× of magnitude larger than that of bulk tungsten at room temperature. The reason for this is not clear but a TEM

microstructure study of the deposited materials is highly suggested for the future work. A comparison of the resistivities of the deposited materials formed at fast and slow scan speeds showed that a slow scan can improve the conductivity of the deposited materials.

For the future work, TEM study of the deposited materials is necessary to understand the microstructure which determines electrical resistivity of the deposited materials. Further, a temperature-dependent resistivity measurement is helpful to understand the electron transport in the deposited materials. In order to apply EBID to application like nanocircuit fabrication, experiments need to be designed to discover what deposition conditions can improve the resistivity.

References

1. Everhart, T.E., et al. *Proc. 6th Intl. Conf. on X-Ray Optics and Microanalysis*. 1972: Univ. of Tokyo Press.

2. Stewart, R.L., *Insulating films formed under electron and ion bombardment.* Physical review, 1934. **45**: p. 488-490.

3. Watson, J.H.L., *An Effect of Electron Bombardment upon Carbon Black.* Journal of Applied Physics, 1947. **18**(2): p. 153-161.

4. Hillier, J., *On the Investigation of Specimen Contamination in the Electron Microscope.* Journal of Applied Physics, 1948. **19**(3): p. 226-230.

5. Poole, K.M., Proc. Phys. Soc. London B, 1953. **66**: p. 542.

6. Ennos, E., Brit. J. Appl. Phys., 1953. **4**: p. 101.

7. Ennos, E., Brit. J. Appl. Phys., 1954. **5**: p. 27.

8. Scheffels, W., ed. *Proc. Stockholm Conf. Electron Microscopy*. ed. J. Rhodin. 1958, Almquist & Wishell: Stockholm. 77.

9. Martin, J.P., *Doctoral Dissertation*. 1972, Universitat Tubingen: Tubingen.

10. Schief, R., Optik, 1969. **29**: p. 416.

11. Muller, K.H., Optik, 1971. **33**: p. 296.

12. Broers, A.N., et al., *Electron-beam fabrication of 80-angstrom metal structures.* Applied Physics Letters, 1976. **29**: p. 596-598.

13. Moore, G.E. *Progress in Digital Integrated Electronics*. in *IEDM Technical Digest*. 1975. Washington, D. C.

14. Campbell, S.A., *The Science and Engineering of Microelectronic Fabrication*. 2nd Edition ed. 2001: Oxford University Press.

15. Hoyle, P.C., et al., *Electrical-Resistance of Electron-Beam-Induced Deposits from Tungsten Hexacarbonyl.* Applied Physics Letters, 1993. **62**(23): p. 3043-3045.

16. Hoyle, P.C., J.R.A. Cleaver, and H. Ahmed, *Ultralow-Energy Focused Electron-Beam-Induced Deposition.* Applied Physics Letters, 1994. **64**(11): p. 1448-1450.

17. Schiffmann, K.I., *Investigation of fabrication parameters for the electron-beam-induced deposition of contamination tips used in atomic force microscopy.* Nanotechnology, 1993. **4**: p. 163-169.

18. Hoffmann, P., I. Utke, and F. Cicoira, *Limits of 3-D nanostructures fabricated by focused electron beam (FEB) induced deposition.* 10th Int. Symp. "Nanostructures: Physics and Technology", 2002.

19. Kislov, N.A. and I. Khodos, *Direct electron-beam-induced formation of nanometer-scale carbon structures in STEM.* Microscopy Microanalysis Microstructures, 1992. **3**: p. 323-331.

20. Bauerdick, S., et al., *In-situ monitoring of electron beam induced deposition by atomic force microscopy in a scanning electron microscope.* Microelectronic Engineering, 2003. **67-8**: p. 963-969.

21. Miura, N., et al., *Electron-beam-induced deposition of carbonaceous microstructures using scanning electron microscopy.* Applied Surface Science, 1997. **114**: p. 269-273.

22. Matsui, S. and K. Mori, *New Selective Deposition Technology by Electron-Beam Induced Surface-Reaction.* Journal of Vacuum Science & Technology B, 1986. **4**(1): p. 299-304.

23. Kohlmannvonplaten, K.T., et al., *Electron-Beam Induced Tungsten Deposition - Growth-Rate Enhancement and Applications in Microelectronics.* Journal of Vacuum Science & Technology B, 1992. **10**(6): p. 2690-2694.

24. Ichihashi, T. and S. Matsui, *Insitu Observation on Electron-Beam Induced Chemical Vapor-Deposition by Transmission Electron-Microscopy.* Journal of Vacuum Science & Technology B, 1988. **6**(6): p. 1869-1872.

25. Komuro, M. and H. Hiroshima, *Lateral tunnel junction produced by electron-beam-induced deposition.* Journal of Vacuum Science & Technology B, 1997. **15**(6): p. 2809-2815.

26. Ochiai, Y., J. Fujita, and S. Matsui, *Electron-beam-induced deposition of copper compound with low resistivity.* Journal of Vacuum Science & Technology B, 1996. **14**(6): p. 3887-3891.

27. Koops, H.W.P., et al., *High-Resolution Electron-Beam Induced Deposition.* Journal of Vacuum Science & Technology B, 1988. **6**(1): p. 477-481.

28. Hiroshima, H. and M. Komuro, *Fabrication of conductive wires by electron-beam-induced deposition.* Nanotechnology, 1998. **9**(2): p. 108-112.

29. Kim, S.H. and G.A. Somorjai, *Stereospecific Ziegler-Natta model catalysts produced by electron beam-induced deposition of TiCl4: Deposition kinetics, film structure, and surface structure.* Journal of Physical Chemistry B, 2002. **106**(6): p. 1386-1391.

30. Wang, S., et al., *Electron-beam induced initial growth of platinum films using Pt(PF3)(4).* Journal of Vacuum Science & Technology B, 2004. **22**(4): p. 1803-1806.

31. Matsui, S. and K. Mori, *New Selective Deposition Technology by Electron-Beam Induced Surface-Reaction.* Japanese Journal of Applied Physics Part 2-Letters, 1984. **23**(9): p. L706-L708.

32. Takahashi, T., et al., *Mocvd Selective Growth of Gaasc Wire and Dot Structures by Electron-Beam Irradiation.* Journal of Crystal Growth, 1992. **124**(1-4): p. 213-219.

33. Scheuer, V., H.W. Koops, and T. Tschudi, *Electron beam decomposition of carbonyls on silicon.* Microelectronic Engineering, 1986. **5**: p. 423.

34. Brunger, W.H., *X-ray mask repair by electron beam induced metal deposition.* Microelectronic Engineering, 1989. **9**: p. 171.

35. Perentes, A., et al., *Focused electron beam induced deposition of a periodic transparent nano-optic pattern.* Microelectronic Engineering, 2004. **73-74**: p. 412-416.

36. Lee, K.L. and M. Hatzakis, *Direct Electron-Beam Patterning for Nanolithography.* Journal of Vacuum Science & Technology B, 1989. **7**(6): p. 1941-1946.

37. Utke, I., et al., *Focused electron beam induced deposition of gold.* Journal of Vacuum Science & Technology B, 2000. **18**(6): p. 3168-3171.

38. Kohlmannvonplaten, K.T., et al., *Resolution Limits in Electron-Beam-Induced Tungsten Deposition.* Journal of Vacuum Science & Technology B, 1993. **11**(6): p. 2219-2223.

39. Hoyle, P.C., J.R.A. Cleaver, and H. Ahmed, *Electron beam induced deposition from W(CO)(6) at 2 to 20 keV and its applications.* Journal of Vacuum Science & Technology B, 1996. **14**(2): p. 662-673.

40. Koops, H.W.P., A. Kaya, and M. Weber, *Fabrication and characterization of platinum nanocrystalline material grown by electron-beam induced deposition.* Journal of Vacuum Science & Technology B, 1995. **13**(6): p. 2400-2403.

41. Hiroshima, H., et al., *Conditions for fabrication of highly conductive wires by electron-beam-induced deposition.* Japanese Journal of Applied Physics Part 1-Regular Papers Short Notes & Review Papers, 1999. **38**(12B): p. 7135-7139.

42. Lau, Y.M., et al., *Properties and applications of cobalt-based Material produced by electron-beam-induced deposition.* Journal of Vacuum Science & Technology a-Vacuum Surfaces and Films, 2002. **20**(4): p. 1295-1302.

43. Komuro, M., H. Hiroshima, and A. Takechi, *Miniature tunnel junction by electron-beam-induced deposition.* Nanotechnology, 1998. **9**(2): p. 104-107.

44. Bruk, M.A., et al., *Focused electron beam-induced deposition of iron- and carbon-containing nanostructures from triiron dodecacarbonyl vapor.* High Energy Chemistry, 2005. **39**(2): p. 65-68.

45. Schossler, C., et al., *Electrical, and field emission properties of nanocrystalline materials fabricated by electron-beam induced deposition.* Microelectronic Engineering, 1996. **30**(1-4): p. 471-474.

46. Kretz, J., et al., *3-Dimensional Structurization by Additive Lithography, Analysis of Deposits Using Tem and Edx, and Application to Field-Emitter Tips.* Microelectronic Engineering, 1994. **23**(1-4): p. 477-481.

47. Koops, H.W.P., et al., *Characterization and Application of Materials Grown by Electron-Beam-Induced Deposition.* Japanese Journal of Applied Physics Part 1-Regular Papers Short Notes & Review Papers, 1994. **33**(12B): p. 7099-7107.

48. Song, M.H., K. Mitsuishi, and K. Furuya, *Crystallization under 1 MeV electron beam irradiation of nanometer-sized W-dendrites fabricated on alumina*

substrates with electron-beam-induced deposition, in *Pricm 5: The Fifth Pacific Rim International Conference on Advanced Materials and Processing, Pts 1-5*. 2005. p. 4035-4038.

49. Kislov, N.A., *Direct STEM fabrication and characterization of self-supporting carbon structures for nanoelectronics.* Scanning, 1993. **15**: p. 212-218.

50. Weber, M., et al., *New Compound Quantum-Dot Materials Produced by Electron-Beam-Induced Deposition.* Journal of Vacuum Science & Technology B, 1995. **13**(3): p. 1364-1368.

51. Weber, M., et al., *Electron-beam induced deposition for fabrication of vacuum field emitter devices.* Journal of Vacuum Science & Technology B, 1995. **13**(2): p. 461.

52. Utke, I., et al., *Thermal effects during focused electron beam induced deposition of nanocomposite magnetic-cobalt-containing tips.* Microelectronic Engineering, 2004. **73-74**: p. 553-558.

53. Bell, D.A., et al., *Electron-Beam-Induced Deposition of Tungsten.* Journal of Vacuum Science & Technology B, 1994. **12**(5): p. 2976-2979.

54. Lipp, S., et al., *A comparison of focused ion beam and electron beam induced deposition processes.* Microelectronics and Reliability, 1996. **36**(11-12): p. 1779-1782.

55. Gopal, V., et al., *Metal delocalization and surface decoration in direct-write nanolithography by electron beam induced deposition.* Applied Physics Letters, 2004. **85**(1): p. 49-51.

56. Shimojo, M., et al., *Electron induced nanodeposition of tungsten using field emission scanning and transmission electron microscopes.* Journal of Vacuum Science & Technology B, 2004. **22**(2): p. 742-746.

57. Fischer, M., et al., *Direct-write deposition with a focused electron beam.* Microelectronic Engineering, 2006. **83**(4-9): p. 784-787.

58. Silvis-Cividjian, N., et al., *The role of secondary electrons in electron-beam-induced-deposition spatial resolution.* Microelectronic Engineering, 2002. **61-2**: p. 693-699.

59. Tanaka, M., et al., *The size dependence of the nano-dots formed by electron-beam-induced deposition on the partial pressure of the precursor.* Applied Physics a-Materials Science & Processing, 2004. **78**(4): p. 543-546.

60. Matsui, S., T. Ichihashi, and M. Mito, *Electron-Beam Induced Selective Etching and Deposition Technology.* Journal of Vacuum Science & Technology B, 1989. **7**(5): p. 1182-1190.

61. Matsui, S. and K. Mori, *Insitu Observation on Electron-Beam Induced Chemical Vapor-Deposition by Auger-Electron Spectroscopy.* Applied Physics Letters, 1987. **51**(9): p. 646-648.

62. Matsui, S. and M. Mito, *Si Deposition by Electron-Beam Induced Surface-Reaction.* Applied Physics Letters, 1988. **53**(16): p. 1492-1494.

63. Luisier, A., et al., *Comparative study of Cu-precursors for 3D focused electron beam induced deposition.* Journal of the Electrochemical Society, 2004. **151**(9): p. C590-C593.

64. Guise, O., et al., *Electron-beam-induced deposition of carbon films on Si(100) using chemisorbed ethylene as a precursor molecule.* Surface Science, 2004. **571**(1-3): p. 128-138.

65. Rub, M., H.W. Koops, and T. Tschudi, *Electron beam induced deposition in a reducing image projector.* Microelectronic Engineering, 1989. **9**(1-4): p. 251-254.

66. Ishibashi, A., K. Funato, and Y. Mori, *Electron-Beam-Induced Resist and Aluminum Formation.* Journal of Vacuum Science & Technology B, 1991. **9**(1): p. 169-172.

67. Koops, H.W.P., et al., *Conductive dots, wires, and supertips for field electron emitters produced by electron-beam induced deposition on samples having increased temperature.* Journal of Vacuum Science & Technology B, 1996. **14**(6): p. 4105-4109.

68. Utke, T., et al., *Electron beam induced deposition of metallic tips and wires for microelectronics applications.* Microelectronic Engineering, 2000. **53**(1-4): p. 261-264.

69. Liang, T. and A. Stivers, *Damage-free mask repair using electron-beam-induced chemical reactions.* Proceedings of SPIE, 2002. **4688**: p. 375.

70. Gopal, V., et al., *Rapid prototyping of site-specific nanocontacts by electron and ion beam assisted direct-write nanolithography.* Nano Letters, 2004. **4**(11): p. 2059-2063.

71. Koops, H.W.P., et al., *Miniature Low-Voltage Beam Systems Producable by Combined Lithographies.* Nuclear Instruments & Methods in Physics Research Section a-Accelerators Spectrometers Detectors and Associated Equipment, 1995. **363**(1-2): p. 1-9.

72. Koops, H.W.P., et al., *Two-dimensional photonic crystals produced by additive nanolithography with electron beam-induced deposition act as filters in the infrared.* Microelectronic Engineering, 2001. **57-8**: p. 995-1001.

73. Abe, H., et al., *Electric transport and mechanical strength measurements of carbon nanotubes in scanning electron microscope.* Physica E-Low-Dimensional Systems & Nanostructures, 2004. **24**(1-2): p. 42-45.

74. Kim, K.S., et al., *In situ manipulation and characterizations using nanomanipulators inside a field emission-scanning electron microscope.* Review of Scientific Instruments, 2003. **74**(9): p. 4021-4025.

75. Mateiu, R., et al., *An approach to a multi-walled carbon nanotube based mass sensor.* Microelectronic Engineering, 2004. **73-74**: p. 670-674.

76. Kim, P. and C.M. Lieber, *Nanotube Nanotweezers.* Science, 1999. **286**: p. 2148-2150.

77. Fritzsche, W., et al., *Making electrical contact to single molecules.* Nanotechnology, 1998. **9**(3): p. 177-183.

78. Fritzsche, W., et al., *Wiring of metallized microtubules by electron beam-induced structuring.* Nanotechnology, 1999. **10**(3): p. 331-335.

79. Richter, J., et al., *Construction of highly conductive nanowires on a DNA template.* Applied Physics Letters, 2001. **78**(4): p. 536-538.

80. Jumpertz, R., et al., *Magnetically refined tips for Scanning Force Microscopy.* Microelectronic Engineering, 1997. **35**(1-4): p. 325-328.

81. Zenhausern, F., et al., *Enhanced Imaging of Biomolecules with Electron-Beam Deposited Tips for Scanning Force Microscopy.* Journal of Applied Physics, 1993. **73**(11): p. 7232-7237.

82. Hubner, B., et al., *Tips for Scanning Tunneling Microscopy Produced by Electron-Beam-Induced Deposition.* Ultramicroscopy, 1992. **42**: p. 1519-1525.

83. Chen, I.C., et al., *Extremely sharp carbon nanocone probes for atomic force microscopy imaging.* Applied Physics Letters, 2006. **88**(15).

84. Crozier, P.A., et al., *Synthesis of uniform GaN quantum dot arrays via electron nanolithography of D2GaN3.* Applied Physics Letters, 2004. **84**(18): p. 3441-3443.

85. Koops, H.W.P., et al., *Constructive 3-Dimensional Lithography with Electron-Beam-Induced Deposition for Quantum Effect Devices.* Journal of Vacuum Science & Technology B, 1993. **11**(6): p. 2386-2389.

86. Takahashi, T., et al., *Selective Growth of Gaas Wire Structures by Electron-Beam Induced Metalorganic Chemical Vapor-Deposition.* Applied Physics Letters, 1992. **60**(1): p. 68-70.

87. Guise, O., et al., *Patterning of sub-10-nm Ge islands on Si(100) by directed self-assembly.* Applied Physics Letters, 2005. **87**(17).

88. Bauerdick, S., et al., *Addressable field emitter array: A tool for designing field emitters and a multibeam electron source.* Journal of Vacuum Science & Technology B, 2004. **22**(6): p. 3539-3542.

89. Floreani, F., H.W. Koops, and W. Elsasser, *Concept of a miniaturised free-electron laser with field emission source.* Nuclear Instruments & Methods in Physics Research Section a-Accelerators Spectrometers Detectors and Associated Equipment, 2002. **483**(1-2): p. 488-492.

90. Murakami, K., et al., *Fabrication of nano electron source using beam-assisted process.* Japanese Journal of Applied Physics Part 1-Regular Papers Short Notes & Review Papers, 2003. **42**(6B): p. 4037-4040.

91. Ochiai, C., et al., *Fabrication process of field emitter arrays using focused ion and electron beam induced reaction.* Journal of Vacuum Science & Technology B, 2001. **19**(3): p. 933-935.

92. Schoessler, C. and H.W.P. Koops, *Nanostructured integrated electron source.* Journal of Vacuum Science & Technology B, 1998. **16**(2): p. 862-865.

93. Schossler, C., J. Urban, and H.W.P. Koops, *Conductive supertips for scanning probe applications.* Journal of Vacuum Science & Technology B, 1997. **15**(4): p. 1535-1538.

94. Sellmair, J., K. Edinger, and H.W.P. Koops, *Investigation of a microtriode with a planar field emitter-extractor source fabricated by direct-write nanolithography using electron beam induced deposition.* Journal of Vacuum Science & Technology B, 2005. **23**(2): p. 781-785.

95. Takai, M., et al., *Fabrication of field emitter array using focused ion and electron beam induced reaction.* Microelectronic Engineering, 1998. **42**: p. 453-456.

96. Yang, X., et al., *Integrated tungsten nanofiber field emission cathodes selectively grown by nanoscale electron beam-induced deposition.* Applied Physics Letters, 2005. **86**(18).

97. Yavas, O., et al., *Maskless fabrication of field-emitter array by focused ion and electron beam.* Applied Physics Letters, 2000. **76**(22): p. 3319-3321.

98. Yavas, O., et al., *Field emitter array fabricated using focused ion and electron beam induced reaction.* Journal of Vacuum Science & Technology B, 2000. **18**(2): p. 976-979.

99. Ito, Y., A.L. Bleloch, and L.M. Brown, *Nanofabrication of solid- state Fresnel lenses for electron optics.* Nature, 1998. **394**: p. 49 - 52.

100. Mitsuishi, K., et al., *Nano-fabrication using electron-beam-induced deposition combined with low energy ion milling.* Nuclear Instruments & Methods in Physics Research Section B-Beam Interactions with Materials and Atoms, 2006. **242**(1-2): p. 244-246.

101. Miura, N., et al., *Application of carbonaceous material for fabrication of nano-wires with a scanning electron microscopy.* Japanese Journal of Applied Physics Part 2-Letters, 1996. **35**(8B): p. L1089-L1091.

102. van Dorp, W.F., et al., *Approaching the resolution limit of nanometer-scale electron beam-induced deposition.* Nano Letters, 2005. **5**(7): p. 1303-1307.

103. Wang, S., Y.M. Sun, and J.M. White, *Electron induced deposition and in situ etching of CrOxCly films.* Applied Surface Science, 2005. **249**(1-4): p. 110-114.

104. Silvis-Cividjian, N., et al., *Direct fabrication of nanowires in an electron microscope.* Applied Physics Letters, 2003. **82**(20): p. 3514-3516.

105. Hubner, U., et al., *On-line nanolithography using electron beam-induced deposition technique.* Microelectronic Engineering, 2001. **57-8**: p. 953-958.

106. Wooldridge, D.E., *Theory of Secondary Emission.* Physical Review, 1939. **56**(6): p. 562 LP - 578.

107. Wolff, P.A., *Theory of Secondary Electron Cascade in Metals.* Physical Review, 1954. **95**(1): p. 56 LP - 66.

108. Schou, J., *Transport theory for kinetic emission of secondary electrons from solids.* Physical Review B, 1980. **22**(5): p. 2141 LP - 2174.

109. Czyzeweski, Z., et al., Journal of Applied Physics, 1990. **68**: p. 3066.

110. Kanaya, K., S. Ono, and F. Ishigaki, *Secondary electron emission from insulators.* Journal of Applied Physics D, 1978. **11**: p. 2425-2437.

111. Grais, K.I. and A.M. Bastawros, *A study of secondary electron emission in insulators and semiconductors.* Journal of Applied Physics, 1982. **53**(7): p. 5239-5242.

112. Chung, M.S. and T.E. Everhart, *Role of plasmon decay in secondary electron emission in the nearly-free-electron metals. Application to aluminum.* Physical Review B, 1977. **15**(10): p. 4699 LP - 4715.

113. Seiler, H., Z. Angew. Phys., 1967. **22**: p. 249.

114. Seiler, H., *Secondary electron emission in the scanning electron microscope.* Journal of Applied Physics, 1983. **54**: p. R1-R18.

115. Kanter, H., Phys. Rev., 1961. **121**: p. 677.

116. Brunauer, S., P. Emmett, and E. Teller, J. Am. Chem. Soc., 1938. **60**: p. 309.

117. Hudson, J.B., *Surface Science: An Introduction*. 1998, Troy, New York: John Wiley & Sons.

118. Kim, Y.K. and K.K. Irikura. *Proc. 2nd Int. Conf. on Atom. Molec. Data and Their Applications*. in *AIP Conf.* 2000. New York, NY.

119. Kunz, R.R., T.E. Allen, and T.M. Mayer, *Selective Area Deposition of Metals Using Low-Energy Electron-Beams.* Journal of Vacuum Science & Technology B, 1987. **5**(5): p. 1427-1431.

120. Hirose, F. and H. Sakamoto, *Low-temperature Si selective epitaxial growth using electron-beam-induced reaction.* Japanese Journal of Applied Physics Part 1-Regular Papers Short Notes & Review Papers, 1995. **34**(11): p. 5904-5907.

121. Foord, J. and R. Jackman, *CHEMICAL VAPOR-DEPOSITION ON SILICON - INSITU SURFACE STUDIES.* CHEMICAL PHYSICS LETTERS, 1984. **112**(2): p. 190-194.

122. Basner, R., M. Schmidt, and K. Becker, *Measurements of absolute total and partial cross sections for the electron ionization of tungsten hexafluoride (WF6).* International Journal of Mass Spectrometry, 2004. **233**(1-3): p. 25-31.

123. Hoffmann, P., et al., *FOCUSED ELECTRON BEAM INDUCED DEPOSITION OF GOLD AND RHODIUM.* Mat. Res. Soc. Symp. Proc, 2002. **624**: p. 171.

124. Hiroshima, H. and M. Komuro, *High growth rate for slow scanning in electron-beam-induced deposition.* Japanese Journal of Applied Physics Part 1-Regular Papers Short Notes & Review Papers, 1997. **36**(12B): p. 7686-7690.

125. Weber, M., *Scattering of Nonrelativistic Electrons in Tip Structures.* Journal of Physics D-Applied Physics, 1994. **27**(7): p. 1363-1369.

126. Kunz, R.R. and T.M. Mayer, *Electron-Beam Induced Surface Nucleation and Low-Temperature Decomposition of Metal-Carbonyls.* Journal of Vacuum Science & Technology B, 1988. **6**(5): p. 1557-1564.

127. Jackman, R.B. and J.S. Foord, *The Interaction of Wf6 with Si(100) - Thermal and Photon Induced Reactions.* Surface Science, 1988. **201**(1-2): p. 47-58.

128. Jackman, R.B. and J.S. Foord, *Electron-Beam Stimulated Chemical Vapor-Deposition of Patterned Tungsten Films on Si(100).* Applied Physics Letters, 1986. **49**(4): p. 196-198.

129. Chen, W. and J.T. Roberts, *Adsorption and Reaction of Wf6 on W(100).* Surface Science, 1995. **324**(2-3): p. 169-184.

130. Redhead, P.A., *Thermal desorption of gases.* Vacuum, 1962. **12**(4): p. 203-211.

131. Utke, I., et al., *Cross section investigations of compositions and sub-structures of tips obtained by focused electron beam induced deposition.* Advanced Engineering Materials, 2005. **7**(5): p. 323-331.

132. Madey, T.E. and J.T. Yates, *Electron-Stimulated Desorption as a Tool for Studies of Chemisorption - Review.* Journal of Vacuum Science & Technology, 1971. **8**(4): p. 525-&.

133. Rugamas, F., et al., *Angular profiles of molecular beams from effusive tube sources: I. Experiment.* Meas. Sci. Technol., 2000. **11**: p. 1750-1765.

134. Bret, T., et al., *In situ control of the focused-electron-beam-induced deposition process.* Applied Physics Letters, 2003. **83**(19): p. 4005-4007.

135. Bret, T., et al., *Periodic structure formation by focused electron-beam-induced deposition.* Journal of Vacuum Science & Technology B, 2004. **22**(5): p. 2504-2510.

136. Bret, T., et al., *Electron range effects in focused electron beam induced deposition of 3D nanostructures.* Microelectronic Engineering, 2006. **83**(4-9): p. 1482-1486.

137. Goldstein, J.I., et al., *Scanning Electron Microscopy and X-ray Microanalysis*. 1981, New York: Plenum Press. pg. 61.

138. Joy, D.C., *Monte Carlo Modelling for Electron Microscopy and Microanalysis*. 1995, New York: Oxford University Press.

139. Reimer, L. and D. Stelter, *FORTRAN 77 Monte-Carlo Program for Minicomputers Using Mott Cross-Sections.* Scanning, 1986. **8**: p. 265-277.

140. Myklebust, R., D.E. Newbury, and H. Yakowitz. NBS Special Publication 460, ed. D.E. Newbury. 1976, Washington, DC: National Bureau of Standards. 105.

141. Salvat, F., J.M. Fern′ andez-Varea, and J. Sempau. P*ENELOPE - A Code System forMonte Carlo Simulation of Electron and Photon Transport.* in O*ECD Nuclear Energy Agency: Issy-les-Moulineaux.* 2003.

142. S*mallWorld, LLC: h*http://www.small-world.net/efs.htm. 2005.

143. Hovington, P., D. Drouin, and R. Gauvin, Scanning, 1997. 1**9(**1): p. 20.

144. Gauvin, R., et al., Microsc. Microanal., 2003. 9**(Suppl. 2).**

145. Ritchie, N.W.M., A *new Monte Carlo application for complex sample geometries.* Surface and Interface Analysis, 2005. 3**7:** p. 1006-1011.

146. Jablonski, A., F. Salvat, and C.J. Powell, N*IST Electron Elastic-Scattering Cross-Section Database ?Version 3.1. 2*003, National Institute of Standards and Technology: Gaithersburg, MD,.

147. Joy, D.C. and S. Luo, Scanning, 1989. 11**:** p. 176.

148. Casnati, E., A. Tartari, and C. Baraldi, J. Phys. B: At. Mol. Opt. Phys., 1982. 15**:** p. 155.

149. Heinrich, K.F.J. in Pr*oceedings of the 11th International Congress of X-ray Optics and Microanalysis,.* 1986. London: University of Western Ontario.

150. El*ectron Solid Interaction Database* *http://pciserver.bio.utk.edu/metrology/htm/download.shtml.*

151. Lin, Y. and D.C. Joy, A *Review of SE Yield Data of Elements.* 2005.

152. Napchan, E., Ex*perimental Electron Scattering Data, http://www.mc-set.com/bse/.*

153. Silvis-Cividjian, N., C.W. Hagen, and P. Kruit, Sp*atial resolution limits in electron-beam-induced deposition.* Journal of Applied Physics, 2005. 98**(8**).

154. Silvis-Cividjian, N., El*ectron Beam Induced Nanometer Scale Deposition.* 2002, Delft University Press.

155. Matsui, S., et al., El*ectron-Beam Induced Selective Etching and Deposition Technology. S*uperlattices and Microstructures, 1990. 7(**4**): p. 295-301.

156. Cicoira, F., et al., El*ectron beam induced deposition of rhodium from the precursor RhCl(PF3)(2) (2): morphology, structure and chemical composition. J*ournal of Crystal Growth, 2004. 26**5(3**-4): p. 619-626.

157. Cicoira, F., et al., Au*ger electron spectroscopy analysis of high metal content micro-structures grown by electron beam induced deposition. A*pplied Surface Science, 2005. 24**2(1**-2): p. 107-113.

158. Shimojo, M., et al., Se*lective growth and characterization of nanostructures with transmission electron microscopes. A*pplied Surface Science, 2005. 24**1(1**-2): p. 56-60.

159. Utke, I.T., M., et al., Cr*oss section investigationsFabrication of compositionsalpha-iron and sub-structures of tips obtainediron carbide nanostructures by focused electron -beam induced chemical vapor deposition and postdeposition heat treatment. A*dvanced Engineering MaterialsJapanese Journal of Applied Physics Part 1-Regular Papers Brief Communications & Review Papers, 2005. 74**4(5**7B): p. 323-3315631-5634.

160. Takeguchi, M., M. Shimojo, and K. Furuya, Fa*brication of magnetic nanostructures using electron beam induced chemical vapour deposition. N*anotechnology, 2005. 16**(8**): p. 1321-1325.

161. Ketharanathan, S., et al., El*ectron beam induced deposition of pure, nanoscale Ge. J*ournal of Vacuum Science & Technology B, 2006. 24**(2**): p. 678-681.

162. Folch, A., et al., Hi*gh-vacuum versus "environmental" electron beam deposition. J*ournal of Vacuum Science & Technology B, 1996. 14**(4**): p. 2609-2614.

163. Folch, A., et al., El*ectron-Beam Deposition of Gold Nanostructures in a Reactive Environment. A*pplied Physics Letters, 1995. 66**(1**6): p. 2080-2082.

164. Utke, I., et al., Fo*cused-electron-beam-induced deposition of freestanding three-dimensional nanostructures of pure coalesced copper crystals. A*pplied Physics Letters, 2002. 81**(1**7): p. 3245-3247.

165. Kislov, N.A., et al., El*ectron-beam-induced fabrication of metal-containing nanostructures. S*canning, 1996. 18**(2**): p. 114-118.

166. Takeguchi, M., et al., Na*nostructures fabricated by electron beam induced chemical vapor deposition. S*uperlattices and Microstructures, 2004. 36**(1**-3): p. 255-264.

167. Han, M., et al., Na*nostructure characterization of tungsten-containing nanorods deposited by electron-beam-induced chemical vapour decomposition. P*hilosophical Magazine, 2004. 84**(1**2): p. 1281-1289.

168. Kislov, N.A., et al., Di*rect fabrication of metal-containing self-supporting nanostructures by local electron-beam-induced CVD. S*canning, 1994. 16**:** p. IV38-IV39.

169. Shimojo, M., et al., El*ectron beam-induced nano-deposition using a transmission electron microscope,* in Cr*oss-Disciplinary Applied Research in Materials Science and Technology.* 2005. p. 129-132.

170. Che, R.C., et al., Fa*brication and electron holography characterization of FePt alloy nanorods. A*pplied Physics Letters, 2005. 87**(2**2).

171. Xie, G.Q., et al., Ef*fect of accelerating voltage on crystallization of self-standing W-nanodendrites fabricated on SiO2 substrate with electron-beam-induced deposition. P*hysica E-Low-Dimensional Systems & Nanostructures, 2005. 29**(3-**4): p. 564-569.

172. Xie, G.Q., et al., Ch*aracterization of nanometer-sized Pt-dendrite structures fabricated on insulator Al2O3 substrate by electron-beam-induced deposition.* Journal of Materials Science, 2006. 41**(9)**: p. 2567-2571.

173. Takeguchi, M., M. Shimojo, and K. Furuya, Fa*brication of alpha-iron and iron carbide nanostructures by electron-beam induced chemical vapor deposition and postdeposition heat treatment.* Japanese Journal of Applied Physics Part 1-Regular Papers Brief Communications & Review Papers, 2005. 44**(7**B): p. 5631-5634.

174. Molhave, K., et al., So*lid gold nanostructures fabricated by electron beam deposition.* Nano Letters, 2003. 3(**1**1): p. 1499-1503.

175. Xie, G.Q., et al., Fa*brication of ordered array of tungsten nanoparticles on anodic porous alumina by electron-beam-induced selective deposition.* Journal of Vacuum Science & Technology B, 2004. 22**(6**): p. 2589-2593.

176. Tanaka, M., et al., Mo*rphology of iron silicide nanorods formed by electron-beam-induced deposition using ultrahigh-vacuum transmission electron microscope.* Japanese Journal of Applied Physics Part 1-Regular Papers Brief Communications & Review Papers, 2005. 44**(7**B): p. 5635-5638.

177. Shimojo, M., et al., Na*nodot and nanorod formation in electron-beam-induced deposition using iron carbonyl.* Japanese Journal of Applied Physics Part 1-Regular Papers Brief Communications & Review Papers, 2005. 44**(7**B): p. 5651-5653.

178. Frabboni, S., et al., Fa*brication by electron beam induced deposition and transmission electron microscopic characterization of sub-10-nm freestanding Pt nanowires.* Applied Physics Letters, 2006. 88**(2**1).

179. Lin, J.F., L. Rotkina, and J.P. Bird. Tr*ansport in Pt Nanowires Fabricated by Focused-Ion-Beam Induced Deposition and Electron-Beam Induced Deposition.* in Pr*oc. 2nd Quantum Transport Nano-Hana International Workshop.* 2004.

180. Brintlinger, T., et al., El*ectrodes for carbon nanotube devices by focused electron beam induced deposition of gold. J*ournal of Vacuum Science & Technology B, 2005. 23**(6**): p. 3174-3177.

181. Croitoru, M.D., et al., Vi*sualization and in situ contacting of carbon nanotubes in a scanning electron microscope. J*ournal of Vacuum Science & Technology B, 2005. 23**(6**): p. 2789-2792.

182. Rotkina, L., et al., Lo*garithmic behavior of the conductivity of electron-beam deposited granular Pt/C nanowires. P*hysical Review B, 2005. 72**(2**3).

183. Igaki, J.Y., et al., Co*mparison of FIB-CVD and EB-CVD growth characteristics. M*icroelectronic Engineering, 2006. 83**(4**-9): p. 1225-1228.

184. Nishio, M., et al., De*nsity of electron-beam-induced amorphous carbon deposits. J*ournal of Vacuum Science & Technology B, 2005. 23**(5**): p. 1975-1979.

185. Ketharanathan, S., R. Sharma, and J. Drucker, Na*noscale electron stimulated chemical vapor deposition of Au in an environmental transmission electron microscope. J*ournal of Vacuum Science & Technology B, 2005. 23**(6**): p. 2403-2408.

186. Utke, I., et al., De*nsity determination of focused-electron-beam-induced deposits with simple cantilever-based method. A*pplied Physics Letters, 2006. 88**(3**): p. 031906.

187. Ding, W., et al., Me*chanics of hydrogenated amorphous carbon deposits from electron-beam-induced deposition of a paraffin precursor. J*ournal of Applied Physics, 2005. 98**(1**).

188. Okada, S., et al., Gr*owth manner and mechanical characteristics of amorphous carbon nanopillars grown by electron-beam-induced chemical vapor deposition.* Japanese Journal of Applied Physics Part 1-Regular Papers Brief Communications & Review Papers, 2005. 44**(7**B): p. 5646-5650.

189. Li, C.Y., R.S. Ruoff, and T.W. Chou, Mo*deling of carbon nanotube clamping in tensile tests. C*omposites Science and Technology, 2005. 65**(1**5-16): p. 2407-2415.

190. Utke, I., et al., Te*nsile strengths of metal-containing joints fabricated by focused electron beam induced deposition. A*dvanced Engineering Materials, 2006. 8(**3**): p. 155-157.

191. Xie, G.Q., et al., Co*mpound nanostructures formed by metal nanoparticles dispersed on nanodendrites grown on insulator substrates. A*pplied Physics Letters, 2006. 88**(2**6).

192. Komuro, M. and H. Hiroshima, Fa*brication and properties of dot array using electron-beam-induced deposition. M*icroelectronic Engineering, 1997. 35**(1**-4): p. 273-276.

193. Hwu, J.-J., El*ectron Beam Induced Conductivity Effect of Polymer Resists and Charging Induced Electron Beam Deflection Simulation in Electron Beam Lithography.* 2000, University of Tennessee: Knoxville. p. 171.

194. Kasap, S.O., Pr*inciples of Electronic Materials and Devices.* 2nd ed. 2001, New York: McGraw-Hill. 768.

195. Abeles, B., App*lied Solid State Science,* ed. R. Wolfe. Vol. 6. 1976, New York: Academic Press.

196. Abeles, B., et al., St*ructural and electrical properties of granular metal films. A*dvances in Physics, 1975. 24**(3**): p. p407.

Appendix A

Geometry Code for SIMION Simulation

```
pa_define(131,101,101,planar,non_mirror)   ;define potential array (PA) for the
                                           ;SEM chamber

locate(65,50,50)                           ;locate geometry origin in center of PA
  { e(1)                                   ;use electrode of 1 volt
    { rotate_fill()                        ;rotate fill the chamber wall
      { within{centered_box(0,0,120,90)}
       notin{centered_box(0,0,110,80)}
      }
     rotate_fill()                         ;rotate fill the objective lens
      { within{polyline(55,30 25,5 25,-5 55,-30)}
      }
    }
   e(2)                                    ;use electrode of 2 volt
    { rotate_fill()                        ;rotate fill the sample stage
      { within{polyline(10,5 8,5 8,2 5,2 5,15 -30,15 -30,-15 5,-15 5,-2 8,-2 8,-5 10,-5)}
      }
    }
   e(3)                                    ;use electrode of 3 volt
    { locate(30,40)                        ;locate and fill the Faraday cage
      { locate(,,,,,60)
        { locate(,,,,90)
          { fill
            { within{cylinder(0,0,0,3,3,30)}
            }
          }
        }
      }
    }
   e(4)                                    ;use electrode of 4 volt
    { locate(37,-45)                       ;locate and fill the gas injection needle
      { locate(,,,,,-60)
        { locate(,,,,90)
          { fill
            { within{cylinder(0,0,0,0.1,0.1,50)}
            }
          }
        }
      }
    }
  }
```

Appendix B

Java Code for TruncatedConicalShape

```
package gov.nist.microanalysis.NISTMonte;

import gov.nist.microanalysis.EPQLibrary.*;
import gov.nist.microanalysis.Utility.*;
import junit.framework.*;

/**
 * <p>Title: NISTMonte.TruncatedConicalShape</p>
 *
 * <p>Description: A MonteCarloSS.Shape representing a truncated conical shape which
  can be used to define cones, cylinders and frustums by changing the radii of the both
  ends.
 * It is based on the CylindricalShape class writen by Dr. Nicholas Ritchie</p>
 *
 *
 * <p>Copyright: Pursuant to title 17 Section 105 of the United States Code this software
  is not subject to copyright protection
 * and is in the public domain</p>
 *
 * <p>Company: University of Tennessee</p>
 *
 * @author Wei Li
 * @version 1.0
 */

public class TruncatedConicalShape
  implements MonteCarloSS.Shape, ITransform, Cloneable {
  private double[] mEnd0; // The position of the center of the bottom
  private double[] mEnd1; // The position of the center of the top
  private double[] mDelta; // The length and direction of the axis
  private double mRadius0; // The radius of the bottom
  private double mRadius1; // The radius of the top
  private double mRadius0p2; // The sqr of mRadius0
  private double mRadius1p2; // The sqr of mRadius1
  transient double mLen2; // Cache the length squared...

  static public final String NOT_NEAR = "Not near";
  static public final String END_CAP_1 = "End cap 1";
  static public final String END_CAP_0 = "End cap 0";
  static public final String SIDEWALL = "Sidewall";

  /**
   * MCSS_TruncatedConicalShape - Create a truncated conical shape from the end
    points specified with the specified radii.
   *
```

```
   * @param end0 double[]
   * @param end1 double[]
   * @param radius0 double
   * @param radius1 double
   */
  public TruncatedConicalShape(double[] end0, double[] end1, double radius0, double
radius1) {
    mEnd0 = (double[])end0.clone();
    mEnd1 = (double[])end1.clone();
    mDelta = new double[] {end1[0] - end0[0], end1[1] - end0[1], end1[2] - end0[2]};
    mRadius0p2 = Math2.sqr(radius0);
    mRadius1p2 = Math2.sqr(radius1);
    if(mRadius0p2 < 1.0e-30 || mRadius1p2 < 1.0e-30)
      throw new IllegalArgumentException("The radius is unrealistically small.");
    mLen2 = Math2.sqr(mDelta[0]) + Math2.sqr(mDelta[1]) + Math2.sqr(mDelta[2]);
    if(mLen2 < 1.0e-30)
      throw new IllegalArgumentException("The length is unrealistically small.");
  }

  // See Object JavaDoc
  public Object clone(Object obj){
    TruncatedConicalShape cs=(TruncatedConicalShape)obj;
    Return new TruncatedConicalShape
    (cs.getEnd0(),cs.getEnd1(),cs.getRadius0(),cs.getRadius1());
  }

  /**
   * closestPointOnAxis - Returns the parameterized coordinate of the closest point on
    the cone axis to the specified point.
   *
   * @param p double[]
   * @return double
   */
  final private double closestPointOnAxis(double[] p) {
    return (mDelta[0] * (p[0] - mEnd0[0]) + mDelta[1] * (p[1] - mEnd0[1]) + mDelta[2]
    * (p[2] - mEnd0[2])) / mLen2;
  }

  /**
   * distanceSqr - Distance (squared) from the parameterized point on the cone axis to the
    specified point.
   *
   * @param p double[] - The off axis point
   * @param u double - The parameterized point
   * @return double
```

```
 */
final private double distanceSqr(double[] p, double u) {
  return Math2.sqr(p[0] - (mEnd0[0] + u * mDelta[0])) + Math2.sqr(p[1] - (mEnd0[1] +
  u * mDelta[1])) +Math2.sqr(p[2] - (mEnd0[2] + u * mDelta[2]));
}

/**
 * resultingRadius2 - The resulting radius from the point at u to the cone axis.
 *
 * @param parm0 double[]
 * @param parm1 double[]
 * @param u double
 * @return double
 */
final private double resultingRadius2(double[] parm0, double[] parm1, double u) {
  double[] p = new double[] {parm0[0] + u * (parm1[0] - parm0[0]), parm0[1] + u *
  (parm1[1] - parm0[1]), parm0[2] + u * (parm1[2] - parm0[2])};
  return distanceSqr(p, closestPointOnAxis(p));
}

/**
 * surfaceRad - the resulting radius of a circle formed by intersection of the truncated
  conical surface and a plane which is perpendicular to the cone axis and contains the
  point p
 *
 * @param p double[]
 */
final private double surfaceRad(double[] p) {
   return Math.sqrt(mRadius0p2)-closestPointOnAxis(p)*(Math.sqrt(mRadius0p2)-
  Math.sqrt(mRadius1p2));
}

// see MonteCarloSS.Shape JavaDoc
public boolean contains(double[] pos) {
  // project pos onto the line defined by end0 and end1.
  double u = closestPointOnAxis(pos);
  // Is this point between end0 and end1 and is the distance between pos and the axis
     less than the surfaceRad(pos)?
  return(u >= 0) && (u <= 1.0) && (Math.sqrt(distanceSqr(pos, u)) <=
  surfaceRad(pos));
}

/**
 * getRadius0 - Get the radius of the bottom
 *
```

```
 * @return double[]
 */
public double getRadius0() {
  return mRadius0;
}

/**
 * getRadius1 - Get the radius of the top
 *
 * @return double[]
 */
public double getRadius1() {
  return mRadius1;
}

/**
 * getEnd0 - Get the center position of the bottom.
 *
 * @return double[]
 */
public double[] getEnd0() {
  return mEnd0;
}

/**
 * getEnd1 - Get the center position of the top.
 *
 * @return double[]
 */
public double[] getEnd1() {
  return new double[] {mEnd0[0] + mDelta[0], mEnd0[1] + mDelta[1], mEnd0[2] +
  mDelta[2]};
}

/**
 * isNearWall - Evaluate whether the specified point (specified throught parm0, parm1
  and u) is near the specified wall.  The
 * point is located a fraction u along the distance from parm0 to parm1.
 *
 * @param parm0 double[]
 * @param parm1 double[]
 * @param u double
 * @param wall String
 * @return boolean
 */
```

```
public boolean isNearWall(double[] parm0, double[] parm1, double u, String wall) {
  assert(wall != NOT_NEAR);
  double eps = 1.0e-4;
  double[] p = new double[] {parm0[0] + u * (parm1[0] - parm0[0]), parm0[1] + u *
  (parm1[1] - parm0[1]), parm0[2] + u * (parm1[2] - parm0[2])};
  double t = closestPointOnAxis(p);
  if(wall == END_CAP_0) {
    return(Math.abs(t) < eps);
  } else if(wall == END_CAP_1) {
    return(Math.abs(t - 1.0) < eps);
  } else if(wall == SIDEWALL) {
    return(t > -eps) && (t < 1.0 + eps) && (Math.abs(Math.sqrt(distanceSqr(p, t)) -
    surfaceRad(p)) < eps);
  }
  return false;
}

/**
 * nearWall - Tests which wall the specified point u is near.
 *
 * @param parm0 double[]
 * @param parm1 double[]
 * @param u double
 * @return boolean
 */
public String nearWall(double[] parm0, double[] parm1, double u) {
  double eps = 1.0e-4;
  double[] p = new double[] {parm0[0] + u * (parm1[0] - parm0[0]), parm0[1] + u *
  (parm1[1] - parm0[1]), parm0[2] + u * (parm1[2] - parm0[2])};
  double t = closestPointOnAxis(p);
  // near end caps
  String best = NOT_NEAR;
  double err = Double.MAX_VALUE;
  if(Math.abs(t) < eps) {
    best = END_CAP_0;
    err = Math.abs(t);
  }
  if(Math.abs(t - 1.0) < Math.min(err, eps)) {
    err = Math.abs(t - 1.0);
    best = END_CAP_1;
  }
  double tesp = Math.min(err, eps);
  if((t >= -tesp) && (t <= 1.0 + tesp) && (Math.abs(Math.sqrt(distanceSqr(p, t)) -
  surfaceRad(p)) < tesp ))
    best = SIDEWALL;
```

```
  return best;
}

/** getFirstIntersection - Consider a ray starting at pos0 towards pos1. If the ray does
     not intersect
 * this shape return Double.MAX_VALUE. If the ray does intersect the Shape, return
  the u such that
 * p(u)=pos0+u*(pos1-pos0) is the point at which the intersection occurs. If u is greater
  or equal
 * to 0 but less than or equal to 1, the intersection occurs on the interval [pos0,pos1].
 * This indicates that a full step from pos0 to pos1 will not remain entirely inside Shape.
 * Strategy: If one pos is at the exterior side of cap0 and the other at the interior side
  and the intersection
 * pos is within the cap0, then the path intersects with the cap0. The intersection with
  the cap1 follows a
 * similar way. For the rest conditions we will check if the intersection at the sidewall
  happens.
 * Solve a quadratic equation to find the intersection position. The left side of the
  equation is a function
 * of the intersection position to calculate the closest distance between the intersection
  position and the
 * object axis and the right side of the equation is a function of the intersection position
  to calculate the
 * radius of the circle formed by the object boundary and the plane which is
  perpendicular to the axis and
 * also contains the intersection position. If there are solutions, it means the path
  intersects with the sidewall.
 * But we need to ensure the intersection happens between pos0 and pos1 and the the
  intersection pos is between
 * cap0 and cap1.
 */
public double getFirstIntersection(double[] parm0, double[] parm1) {
    double u = Double.MAX_VALUE;
   double u0 = closestPointOnAxis(parm0);
   double u1 = closestPointOnAxis(parm1);
   //when intersection happens on cap0
   if (((u0<=0.0)&&((u1>=0.0)&&(u1<=1.0))&& (resultingRadius2(parm0, parm1,
  u1/(u1-u0)) <= mRadius0p2))||((u1<=0.0)&&((u0>=0.0)&&(u0<=1.0))&&
  (resultingRadius2(parm0, parm1, u0/(u0-u1)) <= mRadius0p2))) {
        assert (isNearWall(parm0, parm1, u1/(u1-u0), END_CAP_0));
        if ((u0<=0.0)&&((u1>=0.0)&&(u1<=1.0))){
            u=u1/(u1-u0);
        }
        if ((u1<=0.0)&&((u0>=0.0)&&(u0<=1.0))){
            u=u0/(u0-u1);
```

```
        }
    }
    //when intersection happens on cap1
    else if (((u0>=1.0)&&((u1>=0.0)&&(u1<=1.0))&& (resultingRadius2(parm0, parm1,
(u1-1.0)/(u1-u0)) <= mRadius1p2))||((u1>=1.0)&&((u0>=0.0)&&(u0<=1.0))&&
(resultingRadius2(parm0, parm1, (u0-1.0)/(u0-u1)) <= mRadius1p2))) {
        assert (isNearWall(parm0, parm1, (u1-1.0)/(u1-u0), END_CAP_1));
        if ((u0>=1.0)&&((u1>=0.0)&&(u1<=1.0))){
                u=(u1-1.0)/(u1-u0);
        }
        if ((u1>=1.0)&&((u0>=0.0)&&(u0<=1.0))){
                u=(u0-1.0)/(u0-u1);
        }
    }
    else {
        double e0 = parm1[0] - parm0[0], e1 = parm1[1] - parm0[1], e2 = parm1[2] -
        parm0[2];
        double f0 = parm0[0] - mEnd0[0], f1 = parm0[1] - mEnd0[1], f2 = parm0[2] -
        mEnd0[2];
       // Solve[a t^2 + b t + (c - mLen2*surfaceRad(t))=0]
       double a = (Math2.sqr(mDelta[1] * e0 - mDelta[0] * e1) + Math2.sqr(mDelta[2] *
        e0 - mDelta[0] * e2) + Math2.sqr(mDelta[2] * e1 - mDelta[1] * e2))-
        Math2.sqr(mDelta[0]*e0+mDelta[1]*e1+mDelta[2]*e2)*Math2.sqr(Math.sqrt(m
        Radius0p2)-Math.sqrt(mRadius1p2))/mLen2;
        double b = 2.0 * (Math2.sqr(mDelta[0]) * (e1 * f1 + e2 * f2) +
        Math2.sqr(mDelta[1]) * (e2 * f2 + e0 * f0) + Math2.sqr(mDelta[2]) * (e0 * f0 +
        e1 * f1) - (mDelta[0] * mDelta[1] * (f1 * e0 + f0 * e1) + mDelta[1] * mDelta[2] *
        (f2 * e1 + f1 * e2) + mDelta[2] * mDelta[0] * (f0 * e2 + f2 * e0))) -
        2.0*(mDelta[0]*e0+mDelta[1]*e1+mDelta[2]*e2)*(mDelta[0]*f0+mDelta[1]*f1
        +mDelta[2]*f2)*Math2.sqr(Math.sqrt(mRadius0p2)-
        Math.sqrt(mRadius1p2))/mLen2+2.0*Math.sqrt(mRadius0p2)*(Math.sqrt(mRadi
        us0p2)-Math.sqrt(mRadius1p2))*(mDelta[0]*e0+mDelta[1]*e1+mDelta[2]*e2);
       double c = (Math2.sqr(mDelta[0]) * (Math2.sqr(f1) + Math2.sqr(f2)) +
        Math2.sqr(mDelta[1])* (Math2.sqr(f0) + Math2.sqr(f2)) + Math2.sqr(mDelta[2])
        * (Math2.sqr(f0) + Math2.sqr(f1)) -2.0 * (mDelta[0] * mDelta[1] * f1 * f0 +
        mDelta[0] * mDelta[2] * f0 * f2 + mDelta[1] * mDelta[2] * f2 * f1)) -
        Math2.sqr(mDelta[0]*f0+mDelta[1]*f1+mDelta[2]*f2)*Math2.sqr(Math.sqrt(mR
        adius0p2)-Math.sqrt(mRadius1p2))/mLen2 +2.0*Math.sqrt(mRadius0p2)
        *(Math.sqrt(mRadius0p2)-Math.sqrt(mRadius1p2))
        *(mDelta[0]*f0+mDelta[1]*f1+mDelta[2]*f2)-mRadius0p2*mLen2;
       double rad = b * b - 4.0 * a * c;
       if(rad >= 0) {//intersection requires at least one solution for the equation
         rad = Math.sqrt(rad);
         double tm = (-b - rad) / (2.0 * a);
         double tp = (-b + rad) / (2.0 * a);
```

```
        if(tm < 0.0)
          tm = Double.MAX_VALUE;
        if(tp < 0.0)
          tp = Double.MAX_VALUE;
        double t = Math.min(tm, tp);
        if(t <= 1.0) {//the intersection should happen between pos0 and pos1
          // project this coordinate onto the cone axis
          double cp = u0 + t * (u1 - u0);
          if((cp >= 0.0) && (cp <= 1.0)){//the intersection should happen between cap0
         and cap1
                assert ((t > 1.0) || isNearWall(parm0, parm1, t, SIDEWALL));
                if (Math.sqrt(distanceSqr(parm0, u0)) <= surfaceRad(parm0))
                        u=t;
                else
                        u=1-t;
          }
        }
      } // else never intersects
    }
    return u;
}


// See ITransform for JavaDoc
public void rotate(double[] pivot, double phi, double theta, double psi) {
  mEnd0 = Transform3D.rotate(mEnd0, pivot, phi, theta, psi);
  mDelta = Transform3D.rotate(mDelta, phi, theta, psi);
}

// See ITransform for JavaDoc
public void translate(double[] distance) {
  mEnd0[0] += distance[0];
  mEnd0[1] += distance[1];
  mEnd0[2] += distance[2];
}

// see Object JavaDoc
public String toString(){
  String res="TruncatedCone ([";res+=Double.toString (getEnd0()[0])+","
  +Double.toString(getEnd0()[1]) +","+Double.toString(getEnd0()[2])+"], [";
  res+=Double.toString(getEnd1()[0])+","+Double.toString(getEnd1()[1])+","+Double.
  toString(getEnd1()[2])+"],"; res+=Double.toString(getRadius0())+",";
  res+=Double.toString(getRadius1())+")";
  return res;
}
```

```
  static public class TruncatedConicalShapeTest extends TestCase {
    public TruncatedConicalShapeTest(){
      super("doTest");
    }
    public void doTest(){
      for(int j = 0; j < 100; ++j) {
        double[] e0 = {Math.random(), Math.random(), Math.random()};
        double[] e1 = {Math.random(), Math.random(), Math.random()};
        TruncatedConicalShape c0 = new TruncatedConicalShape(e0, e1, Math.random(),
        Math.random());
        for(int i = 0; i < 100; ++i) {
          double[] parm0 = {2.0 * Math.random(), 2.0 * Math.random(), 2.0 *
          Math.random()};
          double[] parm1 = {2.0 * Math.random(), 2.0 * Math.random(), 2.0 *
          Math.random()};
          double u = c0.getFirstIntersection(parm0, parm1);
          if(u != Double.MAX_VALUE) {
            String wall = c0.nearWall(parm0, parm1, u);
            assertTrue(wall != TruncatedConicalShape.NOT_NEAR);
          } else {
            assertTrue(c0.contains(parm0)==c0.contains(parm1));
          }
        }
      }
    }
  }
}
```

Appendix C

Jython Example Script for EBID

```
# A simple script for a nanofiber on a substrate
import gov.nist.microanalysis.EPQLibrary as epq
import gov.nist.microanalysis.NISTMonte as nm
import java.io as io
import javax.imageio as imgio
# create an instance of the model
print "Start..."
monte=nm.MonteCarloSS()
monte.setBeamEnergy(epq.ToSI.keV(20.0))
monte.setElectronGun(nm.MonteCarloSS.GaussianBeam(monte,10.0e-9))
# create the material, shape and region
mat1=epq.MaterialFactory.createPureElement(epq.Element.Si)
mat2=epq.Material()
mat2.defineByMoleFraction([epq.Element.W,epq.Element.C],[1.0,1.0])
mat2.setDensity(epq.ToSI.gPerCC(15.8))
mat2.setName("WC")
print "Radius = "+r.toString()
# Create the substrate
subs = nm.MultiPlaneShape.createSubstrate([0.0, 0.0, -1.0],[0.0, 0.0, 0.0])
subReg = monte.addSubRegion(monte.getChamber(), mat2, subs)
# create a fiber with hemispherical top
cylinder = nm.CylindricalShape([0.0,0.0,0.0],[0.0,0.0,1.0e-6],80.0e-9)
cone=nm.TruncatedConicalShape([0.0,0.0,-80.0e-9],[0.0,0.0,0.0],20.0e-9,80.0e-9)
sphere=nm.Sphere([0.0,0.0,-80.0e-9],20.0e-9)
tip=nm.SumShape(cone,sphere)
fiber= nm.SumShape(cone,cylinder)
monte.addSubRegion(monte.getChamber(), mat2, tip)
monte.addSubRegion(monte.getChamber(), mat2, cylinder)
monte.addSubRegion(monte.getChamber(), mat2, sphere)
#backscattered stat
back=nm.BackscatterStats(monte)
monte.addActionListener(back)
# add event listeners
xrel=nm.XRayEventListener(monte)
monte.addActionListener(xrel)
przs=nm.PhiRhoStats.watchDefaultTransitions(xrel,-1.0e-6,4.0e-6)
# add a trajectory image
img=nm.TrajectoryImage(2048,2048,0.5e-6)
monte.addActionListener(img)
# add generation images
imgs=nm.EmissionImage.watchDefaultTransitions(xrel,256,5.0e-6)
# run the simulation
monte.runMutipleTrajectories(1000)
# determine where to save the results
dest="c:\\temp\\fiber2\\"
```

```
io.File(dest).mkdirs()
#output the backscatter stats
back.dump(io.FileOutputStream(dest+"backscatter.prn"))
# output the phi-rho-z stats
nm.PhiRhoStats.dumpToFiles(przs,dest)
# output the trajectory image
img.dumpToFile(dest)
# output the transition image
nm.EmissionImage.dumpToFiles(imgs,dest)
print "Done!"
```

Vita

Wei Li was born on March 29, 1977 in Changsha, China. After finishing high school, he entered Xi'an Jiao Tong University, Xi'an, China, for his undergraduate study in 1995. Wei graduated summa cum laude with a BS in Materials Science and Engineering in 1999. Then he worked as a patent consultant at the Legal Department in Hon Hai Precision Industry Co., Ltd. for three years. Wei enrolled into University of Tennessee, Knoxville in 2002 in pursuit of a Ph.D in Materials Science.